Characterization of Tensile Damage for a Short Birch Fiber-reinforced Polyethylene Composite with Acoustic Emission

Alencar Bravo*[1], Lotfi Toubal[2], Demagna Koffi[3], Fouad Erchiqui[4]

[1,2,3]Laboratory of Mechanics and Eco-Materials, University of Quebec at Trois-Rivières,
3351, boul. des Forges, C.P. 500, Trois-Rivières (Québec), Canada

[4]Laboratory of Biomaterials, University of Quebec at Abitibi-Témiscamingue,
445, boul. de l'Université, Rouyn-Noranda (Quebec), Canada

[1]alencar.soares.bravo@uqtr.ca; [2]lotfi.toubal@uqtr.ca; [3]koffi@uqtr.ca; [4]fouad.erchiqui@uqat.ca

Abstract

A biocomposite was prepared using paper industry wood fibers (birch) mixed with a thermoplastic matrix of linear low-density polyethylene (LLDPE) at various fiber weights. Monotonic and load-unload tensile tests were performed at room temperature. The acoustic emission (AE) technique was used to characterize microstructural damage events leading to overall failure of the biocomposite. The behavior evolution (stress/strain) of the biocomposite appears to be correlated with the evolution of the AE cumulative energy, exhibiting four phases. The failure mechanisms in the short fiber-reinforced thermoplastic composites were identified using a neural network based on a Kohonen non-supervised self-organizing map (KSOM). Three parameters of the AE burst signals (amplitude, count and duration) were found to be very useful in classifying damage modes. As a result, a new damage mode definition is proposed based on a neural network with three parameters. The participation of each mode in the final failure was evaluated. The results indicated that fiber content plays a primary role in biocomposite failure. This finding has been further supported by scanning electron microscopy (SEM) micrographs of the fractured face.

Keywords

Acoustic Emission; Birch; Biocomposite; Damage Mechanics; Neural Network; Polyethylene

Introduction

The term, biocomposite, is employed when natural fibers are used as an environmentally friendly alternative to replace composites with traditional fibers. Biocomposites were developed in response to the recent increased need for more ecologically friendly and low-cost materials. Some advantages of natural fibers include their singular properties of low density, high specific strength, enhanced energy recovery, CO_2 neutral after burning, easy processing, bio-degradability and low cost. However, their applications are primarily limited to decorative or non-loading bearing uses. This research aims to expand our understanding of the degradation of these materials and to enhance knowledge of its uses, such as in mechanical gears. Therefore, quantitative analyses and methodologies to assess the behavior of these materials, their properties and their failure modes are extremely important.

In this work, a biocomposite material is developed using paper industry wood fibers (birch) mixed with a thermoplastic matrix of linear low-density polyethylene (LLDPE). Compared to other semi-crystalline polymers, LLDPE has the highest ductility at room temperature. Birch is a common hardwood tree that grows in cool areas with abundant precipitation, such as the province of Quebec, which contains approximately 50% of the growing stock volume of yellow birch in North America. The combination of the two materials results in a biocomposite that is easy to fabricate and consequently should be very affordable.

However, it is surprising how few studies have investigated the damage of LLDPE reinforced with birch fiber. Gu and Raj studied the properties of this type of thermoplastic matrix but used an aspen fiber and they have not studied the damage. Some studies have been conducted to obtain an enhanced interface between two naturally incompatible constituents: hydrophilic fibers and a hydrophobic matrix. Recently, Lafia-Araga tested red balau fibers using various thermal treatments at the fiber level. These researchers observed an increase in matrix/fiber adhesion, which improved the mechanical properties. The use of a coupling agent can also enhance the mechanical properties by improving the matrix/fiber interface. Nevertheless, there is still a lack of comprehensive studies on the failure processes of a thermoplastic matrix of LLDPE reinforced with short fibers (birch).

TABLE 1 LITERATURE REVIEW ON DAMAGE MODES OF COMPOSITES WITH RESPECT TO THE AMPLITUDE RANGE.

Author	Matrix	Fiber	Matrix micro-cracking	Matrix/matrix friction	Debonding	Matrix/fiber friction	Fiber breakage
El Mahi et al.	Epoxy	Flax	42-60 dB	-	60-70 dB	-	70-100 dB
Kotsikos et al.	Polyester	Glass	40-55 dB	-	55-70 dB	-	80-100 dB
Czigány	Poly-propylene	Basalt	21-30 dB	35-45 dB	45-60 dB	-	60-100 dB
Elouaer et al.	Poly-propylene	White hemp and chènevotte	40-60 dB	-	60-65 dB	65-85 dB	85-95 dB
Laksimi et al.	Poly-propylene	Glass	33-45 dB	45-58 dB	58-67 dB	67-85 dB	85-100 dB
Meraghni and Mullin	Epoxy	Glass	35-48 dB	48-60 dB	60-65 dB	65-82 dB	82-100 dB

To achieve this aim, monotonic and load-unload tensile tests were conducted to measure the mechanical properties and failure mechanism evolution caused by irreversible changes in the material due to the application of stress. Acoustic emission (AE) testing was carried out to assess damage mechanisms and their evolution in tensile-test specimens.

Mehan is first researcher to correlate failure mechanism with an acoustic signature (AS). Conventional mechanism analysis is performed by investigating histograms of cumulative hits versus amplitude. The results of amplitude discrimination in composites are available in the literature and are reviewed in Table 1.

In our case, it is important to note that some factors can alter the amplitude of a microstructural event: 1) LLDPE dampers the amplitude at very short distances and 2) fibers obtained from plants have cellular structures that are assembled through a hierarchical process in nature and therefore are not homogeneous. The consequence of these two factors is that damage classifications based on burst amplitude can be inaccurate.

One option is to use artificial neural networks to correct dubious microstructural event classifications using other burst shape information. For this purpose, the Kohonen non-supervised self-organizing map (KSOM) is used; which has a learning style that allows relationships in the input data to be maintained in the output. The working principle of an artificial neural network is based on soft-competitive learning in which adjacent neurons are weighted by a neighborhood function. Although analysis by neural networks may be useful, the results must be corroborated by external knowledge.

This paper is organized as follows. First, the material proprieties and damage level progression are analyzed using mechanical parameters such as stiffness reduction. Second, the damage is evaluated in terms of the AE energy released during various phases using the material condition and changes in shape of the stress/strain curve. Third, the degradation is analyzed in detail using a developed two-step methodology for damage mode characterization in biocomposites with neural networks. Fourth, the results of the mechanical measurements of damage and the AE are combined to verify their correlation. Finally, our conclusions are validated by fractured face scanning electron microscope (SEM) micrographs.

Materials and Experimental Testing

Materials

For this experiment, an LLDPE thermoplastic matrix (Novacor® HI-0753-H) donated by NOVA Chemicals was used with industrial short fibers (thermomechanical pulping, 35 mesh size) of yellow birch (Betula alleghaniensis). The fibers were produced by the Lignocellulosic Materials Research Centre, Trois-Rivieres (Canada) and were dried at 60°C in an air-circulated oven for 24 hours before use.

All of the specimens were prepared using a two-roll mill (Thermon C.W. Brabender, Model T-303) with a 0.6 gear ratio. Grains of LLDPE were melted on rollers at 170°C, and fiber was subsequently added according to the desired weight ratio (0, 10, 20 and 30 wt%).

Dog-bone specimens in accordance with the norm ISO 527-2 were obtained through molding processes. This norm suggests a specimen shape with a length greater than 150 mm and a width of 4 mm. The mold was maintained at a temperature of 205°C by means of a Dake press for 20 minutes under a pressure of 20 MPa.

Experimental Testing

At room temperature, monotonic and load-unload tensile tests were performed following the standards of ISO 527-4. The tests were carried out using an electromechanical testing machine, Instron model LM-U150, equipped with a 150-kN load cell (Fig. 1). During tensile testing, a 25mm extensometer was connected to the data acquisition system and fixed on the gauge length section of the specimen to record the strain evolution.

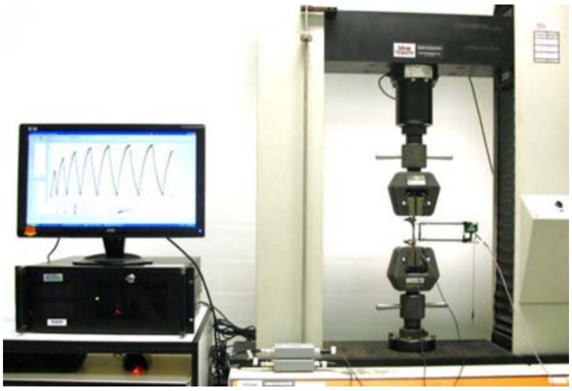

FIG. 1 TENSILE MACHINE TESTING, WITH ACOUSTIC EMISSION EQUIPMENT ON THE LEFT

AE measurements were conducted using devices provided by Physical Acoustics Corporation (PAC), equipped with two PCI cards. Two sensors (type Micro-80 PAC, wideband 100-1000 kHz) were mounted to the surface of the test specimen at a spacing of 70 mm. An acoustic threshold level set at 35 dB was used to filter background noise. A silicone adhesive gel was employed as a coupling agent between the sensors and the specimen. Before each test, the quality of the coupling was verified using a Nielsen-Hsu pencil lead break.

The quality of the measured AE data depends mainly on the choice of the waveform system timing parameters, namely, peak definition time (PDT), hit definition time (HDT) and hit lockout time (HLT). The values of the timing parameters employed are: PDT= 40 μs, HDT = 80 μs and HLT = 200 μs.

Mechanical Behavior Results

Material Properties

Fig. 2a shows the stress-strain curves recorded during monotonic tensile testing while Fig. 2b shows results for the 20 wt% sample, with the monotonic and load-unload tests superposed. The static strength properties are given in Table 2.

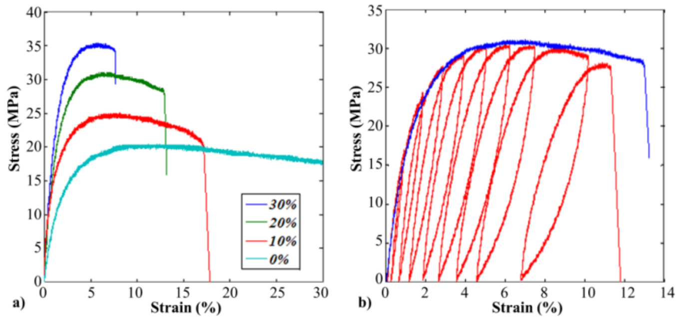

FIG. 2(a) RESULTS FROM THE TENSILE TESTS OF SPECIMENS WITH DIFFERENT FIBER WEIGHTS; (b) RESULTS FOR 20 WT% WITH THE MONOTONIC AND LOAD-UNLOAD TESTS SUPERPOSED.

The manufacturing protocol used in this work demonstrates a good reproducibility of measurements with a low standard deviation. An increase in the fiber proportion reduces the ductility of the material while increasing the Young's modulus and the ultimate strength (cf. Table 2). Compared to a pure matrix, the Young's modulus increases to 98%, 144% and 178% for biocomposites of 10 wt%, 20 wt% and 30 wt% fiber, respectively. In the same order, the ultimate strength increases to 51%, 88% and 94%.

TABLE 2 TENSILE TEST DATA: AVERAGE ULTIMATE STRENGTH AND YOUNG'S MODULUS.

Fiber (wt%)	**Young's modulus**		**Ultimate strength**		**Strain failure**	
	E (GPa)	STD DEV	σ (MPa)	STD DEV	ε (%)	STD DEV
0%	0.91	0.07	16.97	2.56	-	-
10%	1.81	0.11	25.62	1.44	15.46	3.60
20%	2.22	0.18	31.87	1.12	11.39	1.77
30%	2.53	0.27	33.04	1.85	7.17	2.08

These results indicate that 30 wt% approaches the optimum fiber content ratio in these biocomposites, as the maximum load improves by only 6% compared to the result for 20 wt%. This is very low compared to the improvement gained by using 20 wt% versus 10 wt% (37%). Overall, the results are interesting considering that no treatment or coupling agent was used to improve the cohesion of the fiber-matrix interface.

Property Degradation and Failure

As no standard test method exists for load/unload tests, a sufficient number of cycles was chosen to cover the different phases that describe the behavior of the biocomposite. At room temperature, load-unload longitudinal tensile tests were performed as follows: the specimen is loaded until it reaches a certain strain, then the loading is removed. Afterwards, the material is subjected to a higher strain level.

Fig. 3a displays the evolution of residual strain for different fiber weights. The axis of abscissa refers to the maximum strain obtained in each cycle before the unloading phase begins. For all samples, the occurrence of residual strain is measured at 2% of the maximum strain.

In the initial linear elastic range, the biocomposite behaves as a homogeneous material, with the fibers and matrix experiencing the same strain. Above the elastic limit, due to the difference in their Young's moduli, shear force accumulates in the matrix/fiber interface. At this point, the stress and strain in the two components are partially decoupled due to the matrix viscoelasticity. Consequently, the matrix will be compressed and the fiber will be under tensile stress after the unloading phase.

The shear stress in the components will increase, ultimately resulting in the detachment of the fibers from the matrix. If this detachment occurs, damage is induced in the matrix, the yield limit increases and more residual strain is observed. In the case of the 10 wt% specimen, above 10% strain, we can assume that the shear limit of the interface is reached, subsequently causing fiber pullout. Due to the occasioned subsequent fiber detachment, the semi-crystalline LLDPE can reach a higher residual strain. This phenomenon is noted above 4.2% of residual strain with a continuous rate of increase of the residual strain.

The change in the elastic modulus is commonly used to document irreversible changes in the properties of materials due to the application of cyclic stresses or strains. The cumulative damage, D (mechanical damage index), is defined as:

$$D = 1 - E_i/E_o{}^{\circ} \quad (1)$$

where E_i is Young's modulus after the ith cycle and E_0 is the initial modulus.

Fig. 3b presents the evolution of damage accumulation for all specimens. The damage accumulation variable exhibited a logarithmic shape until the final failure occurred. The rapid increase in variable D in the first cycles is most likely related to the viscoelastic behavior, which temporally affects the value of Young's modulus. In this graph, the ability to bear internal damage before failure can be evaluated for each specimen. As the biocomposite fiber content decreases, more internal damage can be borne before final failure. Conversely, higher fiber content induces a more sudden brittle rupture. For 30 wt%, final breakage occurred at 65% of internal damage; for 20wt% and 10 wt%, the final breakage occurred at 69% and 73%, respectively.

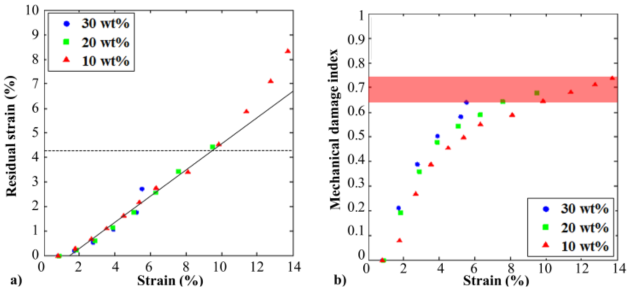

FIG. 3 (a) RESIDUAL STRAIN VERSUS STRAIN AND (b) MECHANICAL DAMAGE INDEX VERSUS STRAIN FOR 10 WT%, 20 WT% AND 30 WT% FIBER SPECIMENS.

Acoustic Emission Results

Degradation in Tensile Tests

AE tests were performed to examine the microstructural failure events contributing to the behavior of the biocomposite. The damage can be observed through the AE energy parameter. Fig. 4 shows the combination of a stress curve and the AE cumulative energy versus strain for a pure matrix and a 10 wt% fiber specimen.

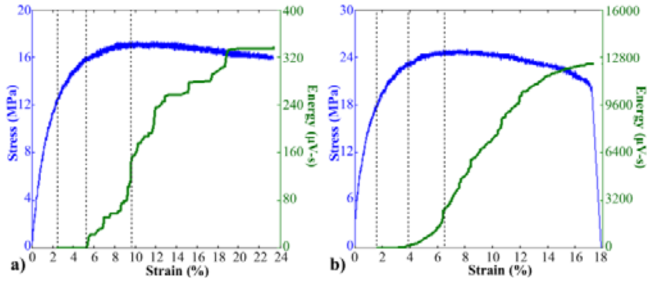

FIG. 4 TENSILE CURVES WITH CUMULATIVE AE ENERGY: (a) 0 WT% AND (b) 10 WT% FIBER.

Four phases are shown in Fig. 4. First, no acoustic activity was recorded in the first linear elastic phase (characterized by an elastic modulus E0). Second, the slope of the stress curve decreased, reflecting the beginning of viscoelastic behavior. We also denote the onset of the first AE energy measurement, with the accumulation of AE energy remaining low and constant. Third, the evolution of the AE energy curve suddenly became exponential. At this point, the stress curve is non-linear, reflecting the onset of plasticity (inelasticity). An assumption can be made that a new mechanism of damage has occurred at this point. Fourth, after the maximum load, the curve evolution of the energy changed and exhibited an almost linear form until the final breakage. Thus, the AE can be correlated to the stress/strain curve shape. These four phases could be distinguished in every specimen.

It is noted that the pure matrix has some particularities, making its phase identification more difficult. For this specimen in particular, only damage events due to matrix microcracking and matrix/matrix friction can be observed (as will be discussed later). The AE waves of these events are characterized by a lower energy. This phenomenon, together with the fact that the test was stopped before final failure (the specimen had a very high elongation, exceeding the limits of the tensile testing machine), resulted in a very low level of energy. The energy recorded at the end of the test for the pure matrix was 335 μV-s, making this curve very sensitive to variation. The total cumulative energy for the 10wt% specimen was 11500 μV-s.

Degradation in Load-unload Tests

Fig. 5 documents the evolution of cumulative energy as a function of time (for the pure matrix and the 10 wt% fiber specimen). As mentioned in the preceding section, the same phases can be observed. The acoustic activity begins with a linear elastic phase, with the detection of the first burst near 12 MPa for the pure matrix and 18 MPa for the 10 wt% specimen. A significant energy value only appears when the load increases to 15 MPa for the pure matrix and to 23 MPa for the 10 wt% specimen. Afterwards, an exponential evolution takes place up to the maximum stress. The energy curve evolution subsequently becomes linear until failure. The loads corresponding to a phase boundary were the same as in the monotonic test. The advantage of this test is its ability to assess damage evolution through mechanical indicators.

The accumulated acoustical energy curve exhibits the same four phases for each specimen. The total energy produced in the pure matrix specimen is again very low (240 µV-s) when compared to the 10 wt% specimen (39654 µV-s). The fibers are responsible for some damage modes, producing considerably more energy. In the case of the biocomposite (Fig. 5b), more energy is recorded in each cycle compared to the pure matrix (Fig. 5a).

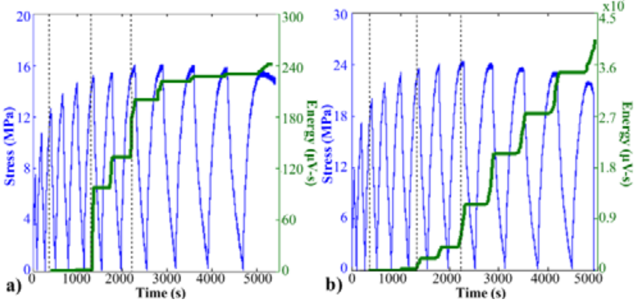

FIG. 5 ACCUMULATED AE ENERGY AND STRESS VERSUS TIME FOR LOAD-UNLOAD TESTS: (a) 0 WT% AND (b) 10 WT% FIBER..

The Kaiser and Felicity Effects

The Kaiser effect occurs in load-unload tests, when applied stress levels that were previously exerted on a material do not produce AE activity. If the Kaiser effect is present, the material is in a relatively good condition and no substantial damage was inflicted. The Felicity effect is a term used when the Kaiser effect is not observed. This effect can be described as the onset of AE events occurring before the previous maximum stress is reached.

The Felicity effect is a much less desirable damage situation because it results in a faster degradation of the material proprieties. According to Pollock, insignificant flaws tend to exhibit the Kaiser effect, while structurally significant flaws tend to exhibit the Felicity effect. Fig. 6 shows the Felicity diagram for the pure matrix and for the 10 wt% specimen.

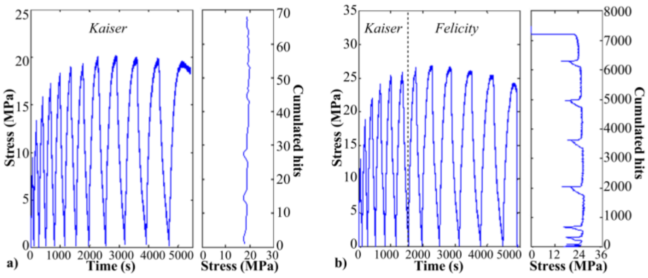

FIG. 6 STRESS VERSUS TIME AND FELICITY EFFECT DIAGRAM FOR (a) 0 WT% AND (b) 10 WT% FIBER.

The pure matrix and biocomposite behave differently regarding their Felicity effect level. While the pure LLDPE presents no Felicity effect during the test, the biocomposite has a substantial Felicity effect with a low fiber content and an increase in the total produced energy with each cycle. In the case of a 10 wt% fiber specimen, the Felicity effect begins after the sixth cycle. This point corresponds to where the third material phase begins in Fig. 5b, with an exponential increase in the energy value. Alternatively, in this phase, significant flaws are inflicted to the material, and it starts losing its mechanical stability. Therefore, in real-life biocomposite applications for a mechanically required piece, replacement must be considered at this stage. As it can be observed by comparing Fig. 4, 5 and 6, the Kaiser effect is beneficial for the pure matrix: the phase transitions not only have the same load but also the same energy level. For example, the final phase began as the total accumulated energy reached 120 µV-s in both the monotonic and the load-unload test. Conversely, the biocomposite final phase was reached at 2834 µV-s in the monotonic test and at 4152 µV-s in the load-unload test, corresponding to a difference of 46.5%.

Consequently, real-time material surveillance using the energy parameter is not recommended for certain cases, such as gear systems. In such cases, for an optimal product life cyclic design, other information might be useful, such as the load level of the material phase transition or a well-known composite AS.

Acoustic Signatures of Damage Mechanisms

Several modes of micro failure mechanisms are found in composites. For mode identification, the amplitude distribution of AE events is commonly used to describe the failure modes. The distribution of the AE amplitude takes the form of groups, which may overlap, reflecting the failure mechanisms.

To best study failure mechanisms in biocomposites, this section is divided into two parts. First, only the failure mechanisms in the pure matrix are studied. Second, the damage modes related to the presence of fibers are discussed for the biocomposites.

Pure Matrix (0 wt% fiber): Pre-analysis of the Damage Mode Classification

Fig. 7a documents the amplitude distributions of the AE events for pure polyethylene. As previously discussed, relatively few bursts were recorded. In this context, two higher peaks are visible in the amplitude histogram at 48 dB and 40 dB, suggesting the presence of two groups of damage. This corresponds to the initiation and propagation of microcracks and matrix/matrix friction, respectively. A local valley near 45 dB indicates a borderline value.

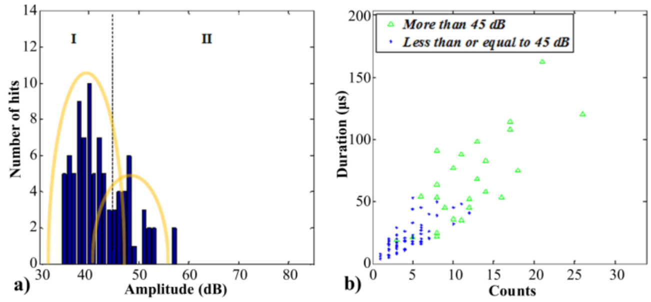

FIG. 7(a) CLASSICAL HISTOGRAM OF AMPLITUDES FOR PURE LLDPE: TWO OVERLAPPING GROUPS REPRESENTING DAMAGE MODES; (b) COUNTS VERSUS DURATION DISCRIMINATED BY AMPLITUDE.

Fig. 7b represents the shape (counts versus duration) of each burst with regard to the limit value of 45 dB. Blue spots represent bursts for which the amplitudes are between 35 dB and 45 dB, and green triangles represent amplitudes between 46 dB and 55 dB. We can attribute matrix microcracks to the blue spots, whereas the green spots have a shorter duration and a lower number of counts and can be attributed to matrix/matrix friction.

Using this classification, some bursts with approximately 5 counts at a duration of 20 µs are classified as matrix/matrix friction. However, we assume that this is a burst with matrix microcracking characteristics, so the classification may be inappropriate.

We can use amplitude discrimination with the tensile stress/strain curve. Fig. 8 illustrates burst amplitude ranges along with the tensile curve. The AE bursts between 35 dB and 45 dB are marked with an asterisk below the tensile curve. Bursts between 45 dB and 55 dB are shown as a circle above the tensile curve. The first microcrack is observed at a 12-MPa load, but the activity remains low until a load of approximately 16 MPa is reached, where a phase with several microcracking events starts. As we reach the maximum stress, the AE activity reaches its maximum. Subsequently, the AE activity rate for both modes stabilizes. This finding corroborates with the suggestion that new mechanisms start at specific phases.

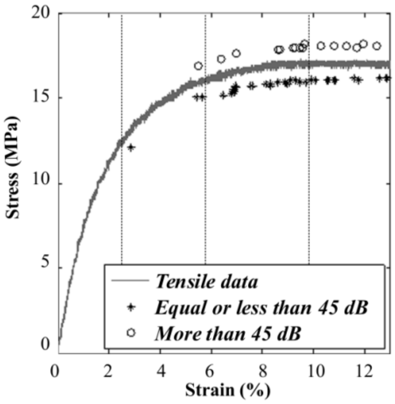

FIG. 8 STRESS/STRAIN CURVE AND AE DAMAGE BURSTS ACCORDING TO AMPLITUDE FOR PURE LLDPE.

Pure Matrix (0 wt% Fiber): KSOM Damage Mode Classification

Based on the key knowledge that a material exhibits phases related to damage mechanisms, in real life applications, it is important to reach a maximum reliability in dealing with damage mode evaluations. As plastic has very high damping characteristics, the amplitude is strongly dependent on the event location with respect to the sensor position. Consequently, it is important to evaluate not only the burst maximum amplitude but also its shape. The number of counts, the duration and the amplitude are important burst shape indicators.

In this section, KSOM is used to increase the discrimination accuracy by using additional burst parameters. KSOM is an unsupervised artificial neural network method that uses the principle of soft-learning. In this method, the neurons adjacent to the winner are weighted through a neighborhood function. All of the data relationships in the input are kept in the output because the algorithm processes information in a manner similar to that of the human brain. In spite of these advantages, results must be corroborated with previous knowledge to ensure that the artificial network is analyzing data properly.

If the results corroborate well with previous knowledge, the result is a topological map referring to the damage modes. The results of the algorithm analyses are documented in the amplitude histogram of Fig. 9a. The graph includes two overlapping groups. These results are in agreement with the study presented in the previous section, confirming the validity of the current results.

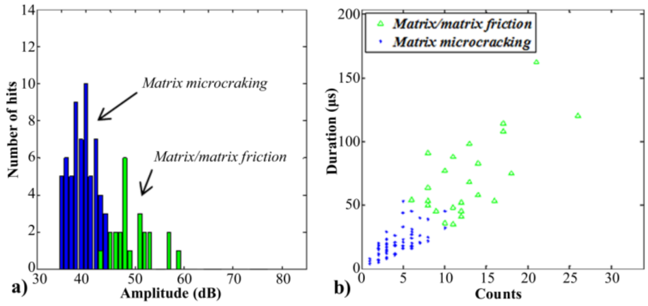

FIG. 9(a) AMPLITUDE HISTOGRAM SUCCESSFULLY DISCRIMINATED BY KSOM FOR PURE LLDPE; (b) COUNTS VERSUS DURATION ACCORDING TO KSOM.

The burst shape information for duration versus counts is documented in Fig. 9b. As expected, the two clusters with overlapping non-linear borders, which are similar to those found in the previous analysis, are good indicators that the discrimination is appropriate. The resulting AS of the matrix microcracking has a characteristic count number of up to 15 and a duration of up to 50 µs while the matrix/matrix friction has a minimum AS of 10 counts and a 25 µs duration.

Biocomposites: Pre-analysis of Damage Mode Classification

In this section, we study the failure mechanisms of the biocomposites. The amplitude distributions for specimens with 10 wt% and 30 wt% birch fiber are displayed in Fig. 10. In the first step, the mode boundaries found for the pure matrix specimens are used in the biocomposite histogram. This implies that mode I and II are already defined, in accordance with the first section (for a pure matrix).

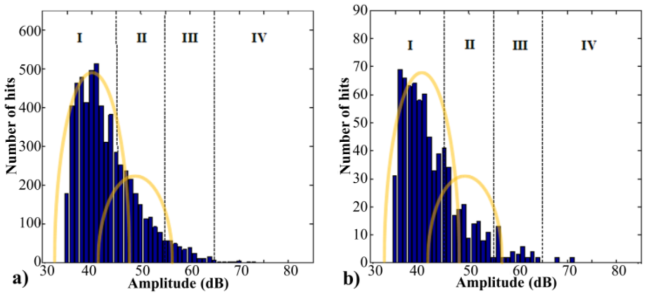

FIG. 10 AMPLITUDE HISTOGRAMS FOR BIOCOMPOSITES: (a) 10 WT% AND (b) 30 WT% FIBER.

The interpretation of the amplitude histograms starts from 55 dB. A discontinuity in shape is observed at 65 dB in both graphs. This suggests the existence of a boundary between the third and fourth modes, with the third group centered at 60 dB. The appearance of a decreasing slope is due to the overlap near 55 dB with mode II and the lack of overlap with mode IV. This last mode would have fewer bursts.

The literature suggests that groups III and IV represent decohesion and matrix/fiber friction, respectively. No bursts were observed from 85 dB to 100 dB, i.e., in the fiber breakage amplitude range; thus, mode V is inexistent due to the short fiber length (mean length: 0.489 mm ± 0.016 mm).

Biocomposites: KSOM Damage Mode Classification

In this section, the KSOM neural network is successfully applied for mode discrimination. The results of amplitude histograms for 10 wt% and 30 wt% are documented in Fig. 11. We denote four overlapping groups with limits close to those previously set in Fig. 10. Thus, the result from KSOM is in good agreement with the other data.

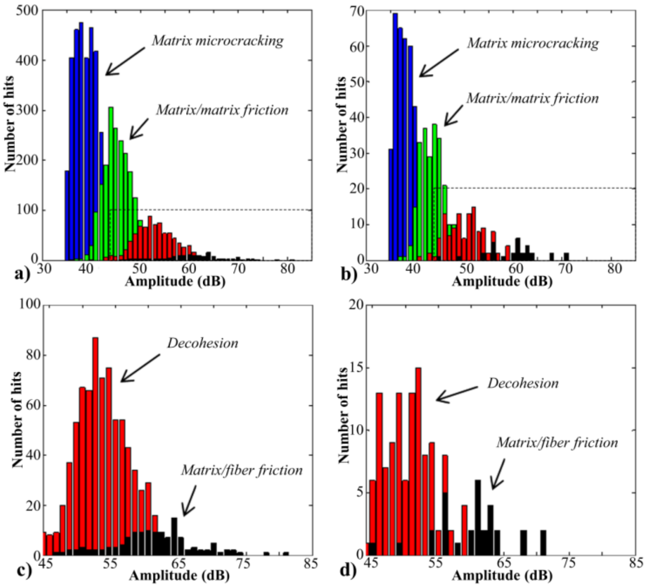

FIG. 11 AMPLITUDE HISTOGRAM SUCCESSFULLY DISCRIMINATED BY KSOM FOR BIOCOMPOSITES: (a) 10 WT% AND (b) 30 WT%. THE RESULTS OF DECOHESION AND MATRIX/FIBER FRICTION ONLY: (c) 10 WT% AND (d) 30 WT%.

For a better visualization, only the decohesion and matrix/fiber friction are documented in Fig. 11c and 11d. The substantial decohesion shown in the histograms reveals a poor matrix/fiber interface. For the 30 wt% specimen, the occurrence of final breakage with low strain contributed to the lower number of bursts recorded. The burst duration versus number of counts is shown in Fig. 12a for the 10 wt% specimen and in Fig. 12b for the 30 wt% specimen.

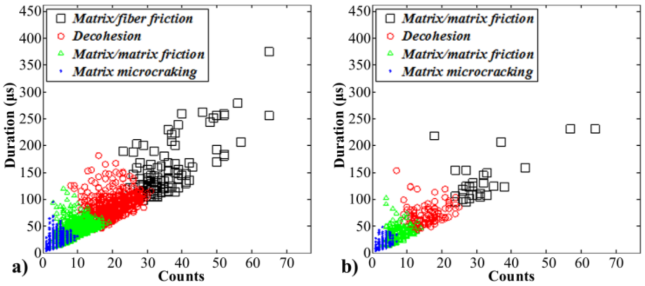

FIG. 12 COUNTS VERSUS DURATION ACCORDING TO THE MODES FOR BIOCOMPOSITES: (a) 10 WT% AND (b) 30 WT% FIBER.

The AS for the damage modes of the biocomposites was successfully discriminated. The multiparameter neural network analysis resulted in four clusters. The borders exhibited some overlapping, but there are still clear domains. As found before, the results were independent of the fiber weight used.

These results are summarized in Table 3. In this table, the AS of each damage mechanism is presented. The amplitude values are comparable to values found in the literature, but they are reinforced by two other parameters: the duration and the number of counts. This additional information allows for a consideration of the fuzziness in the AS that characterizes each damage mechanism. The results of this table can be useful for advanced mode recognition algorithms.

TABLE 3 SUMMARY OF DAMAGE AS.

Damage mode	**Matrix micro-cracking**	**Matrix/ matrix friction**	**Decohesion**	**Matrix/ fiber friction**
Amplitude (dB)	35-45	40-55	45-60	55-85
Duration (µs)	1-80	20-120	50-200	100-600
Counts	1-10	8-20	16-35	30-120

AE Failure Analysis Correlated to Mechanical Behavior

Once the AS is defined, the quantitative mode participation in specimen degradation can be assessed. We use the damage participation ratio (R_{ij}) proposed by Gong et al. which is defined as follows:

$$R_{ij} = \frac{(number\ \ of\ burts)_{ij}}{total\ number\ \ of\ burst} = \frac{m_{ij}}{m_R} \qquad (2)$$

"i" refers to the different modes of damage, "j" to the different load levels, and "m_R" to the total number of bursts at failure. With this definition, it is possible to observe the participation of each damage mechanism as a function of the material residual strain, as shown in Fig. 13.

Fig. 13 is a useful graph because it permits a comparison of the viscoelasticity with measured AE damage. For the 10 wt% specimen, a significant AE damage was observed only at 2.7% of the residual strain, after five cycles, suggesting that the initial increase in variable D (Fig. 3b) may be related to viscoelastic behavior. At this point, the mechanism of matrix/matrix friction contributed 3.19% of the damage. Decohesion and microcracking accounted for similar proportions, 2.41% and 2.40%, respectively. Matrix/fiber friction was the least damaging mode, which accounted for 1.33%, resulting in a total of 9.93% of the measured specimen damage.

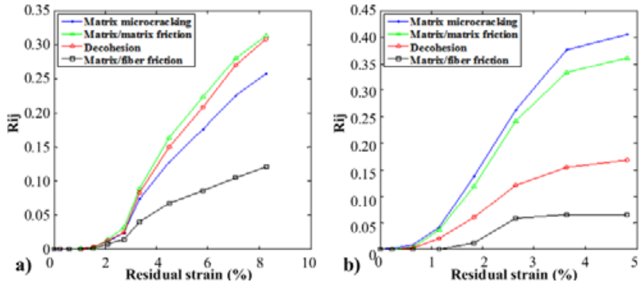

FIG. 13 EVOLUTION OF EACH DAMAGE MECHANISM FOR (a) 10 WT% AND (b) 30 WT% SPECIMENS

It is interesting to correlate the AE analysis with the mechanical behavior. As documented in Fig. 3a, the matrix and fiber of the material uncoupled starting from 4.2% of residual strain. We can see in Fig. 13a that in this cycle of uncoupling a substantial amount of AE activity occurred. At this point, decohesion contributed for 14% of material damage, causing 50% of total damage.

In the final failure, matrix/matrix friction was responsible for 31.42%, decohesion for 30.83%, matrix microcracking for 25.67% and matrix/fiber friction for 12.09%. Interestingly, as the biocomposite approached the final failure, the matrix microcracking accounted for less of the damage; instead, the matrix/matrix friction and decohesion were the dominating mechanisms.

In the case of the 30 wt% specimen, the first considerable damage occurred at 1.2% of the residual strain, after three cycles. At this stage, matrix microcracking accounted for 4.13% of the damage, matrix/matrix friction for 3.56% and decohesion for 2.02%. Matrix/fiber friction had not yet damaged the material, and the total measured damage was 9.71%.

Subsequently, the contribution of each damage mechanism in the final failure was: matrix microcracking, 40.53%; matrix/matrix friction, 36.13%; decohesion, 16.86%; and matrix/fiber friction, 6.48% of the total damage. It is interesting to note the low level of decohesion that occurred, even without a coupling agent. This can be in part attributed to the lower level of stress on the interface matrix/fiber before the final failure occurs.

Scanning Electron Microscopy

To corroborate these results, the fractures were analyzed by SEM. Fig. 14a shows the fractured face of the 10 wt% specimen. A high amount of fiber decohesion led to many voids in the matrix. Furthermore, the high level of friction with the fibers (hard material) led to the surface aspect of a twisted matrix (soft material).

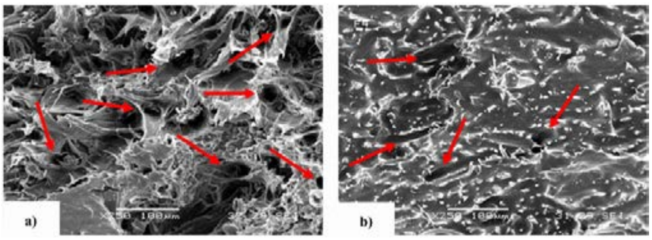

FIG. 14 FRACTURED FACE OF 10 WT% (A) AND 30 WT% (B) SPECIMENS: RED ARROWS INDICATE FIBERS THAT HAVE PULLED OUT.

The fractured face micrograph of the 30 wt% specimen (Fig. 14b) shows fewer fiber voids and a much less damaged matrix surface. As demonstrated by damage mode participation analysis, a lower level of decohesion and, subsequently, less matrix/fiber friction contributed to this surface condition, thus corroborating our results.

Conclusions

In this work, a biocomposite material was developed by mixing paper industry natural fibers (birch) and a thermoplastic matrix (LLDPE) at various fiber weights. Monotonic and load-unload tensile strength tests were conducted to measure the mechanical properties of the materials. An improvement in the elastic modulus and the ultimate strength was obtained for higher fiber weights. The manufacturing protocol used in this work demonstrates excellent measurement reproducibility with a low standard deviation.

AE instrumentation was used to assess the damage in the material along with a mechanical analysis of the stiffness drop. The evolution of the biocomposite behavior in four phases was documented using the AE energy. Exclusive damage modes (i.e., decohesion and matrix/fiber friction) increased the energy measured in the material degradation of the biocomposites. However, a participation analysis is only possible if a clear method of defining the AS is elaborated. For this reason, in the first step only, general conclusions were drawn from the amplitude histogram for the pure matrix. Then, an artificial neural network using the KSOM was utilized, taking into account burst shape information on the counts and duration. The results corroborated the previous analysis, but misclassification was avoided to some extent.

This methodology was extended to biocomposites, which led to an AS classification for advanced algorithms with fuzzy boundaries. The participation of each mode in the final failure was finally evaluated. The results indicate that fiber content plays a primary role in biocomposite failure. This finding was supported by scanning electron microscopy (SEM) micrographs of the fractured face. With these encouraging results, it may be useful to study the degradation until failure of other forms of biocomposites, such as composites with both a matrix and a fiber from ecological sources.

ACKNOWLEDGEMENT

Lignocellulosic Materials Research Centre, Trois-Rivières (Canada).

REFERENCES

Barsoum, Fady F., Suleman, Jamil, Korcak, Andrej, and Hill, Eric.V. K. "Acoustic Emission Monitoring and Fatigue Life Prediction in Axially Loaded Notched Steel Specimens." Journal of acoustic emission 27 (2009): 40-63.

Bera, Moumita, Alagirusamy, R., and Das, Apurba. "A Study on Interfacial Properties of Jute-Pp Composites." Journal of Reinforced Plastics and Composites 29, no. 20 (2010): 3155-61.

Berthelot, Jean-Marie, and Rhazi, J. "Different Types of Amplitude Distributions in Composite Materials." Journal of Reinforced Plastics and Composites 7, no. 4 (1988): 302-20.

Bodig, Jozsef, and Jayne, B. A. "Mechanics of Wood and Wood Composites. Van Nostran-Reinhold Co." Inc., New York (1982).

Bravo, Alencar, Toubal, Lotfi, Koffi, Demagna, Erchiqui, Fouad, and Kokta, Bohuslav V. "Suivi par emission acoustique du Comportement et de l'endommagement d'un composite à matrice thermoplastique renforcée par des fibres de bouleau." RIED 2012 1 (2012): 4.

Czigány, Tibor. "Special Manufacturing and Characteristics of Basalt Fiber Reinforced Hybrid Polypropylene Composites: Mechanical Properties and Acoustic Emission Study." Composites science and technology 66, no. 16 (2006): 3210-20.

El Mahi, Abderrahim, Ben Salem, Imen, Assarar, Mustapha, Berbaoui, Rachid, Poilane, Chritophe, and El Guerjouma, Rachid. "Analyse par émission acoustique de l'endommagement des matériaux éco-composites." Paper presented at the 10ème Congrès Français d'Acoustique, 2010.

Elouaer, Abdelmonem, Aboura, Zoheir, Ayad, Rezak, Sabhi, Hamid, and Benzeggagh, Malk. "Suivi de l'endommagement en fatigue des composites à base de fibres végétales = Monitoring of Fatigue Damage in Composites Based Fiber Plant." Paper presented at the 16èmes Journées Nationales sur les Composites (2009).

G'Sell, Christian. "Plasticité et endommagement des polymères structuraux." L'Actualité chimique, no. 3 (2002): 40-43.

Godin, Nathalie, Huguet, S., Gaertner, R., and Salmon, L. "Clustering of Acoustic Emission Signals Collected During Tensile Tests on Unidirectional Glass/Polyester Composite Using Supervised and Unsupervised Classifiers." NDT & E International 37, no. 4 (2004): 253-64.

Gong, Xiao-Lu, Laksimi, A., and Benzeggagh, M. L. "Nouvelle approche de l’émission acoustique et son application à l’identification des mécanismes d’endommagement dans les matériaux composites." Revue des composites et des Matériaux Composites Avancées 8, no. 1 (1998): 7-23.

Gu, Ruijun, Kokta, Bohuslav V., Michalkova, D., Dimzoski, B., Fortelny, I., Slouf, M., and Krulis, Z. "Characteristics of Wood-Plastic Composites Reinforced with Organo-Nanoclays." Journal of Reinforced Plastics and Composites 29, no. 24 (2010): 3566-86.

ISO 527-2. Determination of Tensile Properties - Part 2: Test Conditions for Moulding and Extrusion Plastics. Geneva: International Organization for Standardization, 1994.

ISO 527-4. Determination of Tensile Properties - Part 4: Test Conditions for Isotropic and Orthotropic Fibre-Reinforced Plastic Composites. Vol. 527, Geneva: International Organization for Standardization, 1997.

Jemielniak, Krzysztof. "Some Aspects of Acoustic Emission Signal Pre-Processing." Journal of Materials Processing Technology 109, no. 3 (2001): 242-47.

Kaiser, Josef. "Erkenntnisse Und Folgerungen Aus Der Messung Von Geräuschen Bei Zugbeanspruchung Von Metallischen Werkstoffen." Arch. Eisenhüttenwes 24, no. 1-2 (1953): 43-45.

Khan, Mubarak A., Masudul Hassan, M., and Drzal, Lawrence T. "Effect of 2-Hydroxyethyl Methacrylate (Hema) on the Mechanical and Thermal Properties of Jute-Polycarbonate Composite." Composites Part A: Applied Science and Manufacturing 36, no. 1 (2005): 71-81.

Kotsikos, George, Evans, J. T., Gibson, A. G., and Hale, J. "Use of Acoustic Emission to Characterize Corrosion Fatigue Damage Accumulation in Glass Fiber Reinforced Polyester Laminates." Polymer composites 20, no. 5 (1999): 689-96.

Lafia-Araga, Ruth A., Hassan, Aziz, Yahya, R., Rahman, Normasmira A., Hornsby, Peter R., and Heidarian, J. "Thermal and Mechanical Properties of Treated and Untreated Red Balau (Shorea Dipterocarpaceae)/Ldpe Composites." Journal of Reinforced Plastics and Composites 31, no. 4 (2012): 215-24.

Laksimi, Adbelouahed, Benmedakhene, S., and Bounouas, L. "Monitoring Acoustic Emission During Tensile Loading of Thermoplastic Composites Materials." Paper presented at the Proceeding of ICCM, 1999.

Lee, Seung G., Choi, Sung-Seen, Park, Won H., and Cho, Donghwan. "Characterization of Surface Modified Flax Fibers and Their Biocomposites with Phb." Paper presented at the Macromolecular Symposia, 2003.

Little, Elbert J. "Checklist of United States Trees (Native and Naturalized)." Agriculture Handbook, UK Department of Agriculture, no. 541 (1979).

Mark, Richard E. "Cell Wall Mechanics of Tracheids." Cell wall mechanics of tracheids. (1967).

Mehan, R. L., and Mullin, J. V. "Analysis of Composite Failure Mechanisms Using Acoustic Emissions." Journal of Composite Materials 5, no. 2 (1971): 266-69.

Meraghni, Fodil, and Benzeggagh, M. L. "Micromechanical Modelling of Matrix Degradation in Randomly Oriented Discontinuous-Fibre Composites." Composites science and technology 55, no. 2 (1995): 171-86.

Miller, Ron K., and McIntire, P. "Nondestructive Testing Handbook. Vol. 5: Acoustic Emission Testing." American Society for Nondestructive Testing, 1987 (1987): 603.

Nourbakhsh, Amir, Ashori, Alireza, and Kouhpayehzadeh, Mojgan. "Giant Milkweed (Calotropis Persica) Fibers—a Potential Reinforcement Agent for Thermoplastics Composites." Journal of Reinforced Plastics and Composites 28, no. 17 (2009): 2143-49.

Nourbakhsh, Amir, Kokta, Bouhuslav V., Ashori, Alireza, and Jahan-Latibari, Ahmad "Effect of a Novel Coupling Agent, Polybutadiene Isocyanate, on Mechanical Properties of Wood-Fiber Polypropylene Composites." Journal of Reinforced Plastics and Composites 27, no. 16-17 (2008): 1679-87.

Physical Acoustics Corporation. PCI-2 Based AE System User's Manual. Princeton, NJ: Physical Acoustics Corporation, 2007.

Pollock, Adrian. "Acoustic Emission-2: Acoustic Emission Amplitudes." Non-destructive testing 6, no. 5 (1973): 264-69.

Raj, R. G., Kokta, Bohuslav V., Maldas, D., and Daneault, C. "Use of Wood Fibers in Thermoplastics. Vii. The Effect of Coupling Agents in Polyethylene–Wood Fiber Composites." Journal of applied polymer science 37, no. 4 (1989): 1089-103.

Santulli, Carlo. "A Biomimetic Approach to the Production of Sustainable Structural Composites Using Plant Fibres." Biologically inspired textiles, Woodhead Publishing (2008).

Toubal, Lotfi, Lorrain, B., Karama, M., and Marlot, D. "Composite Carbone/Époxyde: Suivi Par Émission Acoustique Et Caméra Infrarouge D'un Essai De Fatigue." Contrôles-Essais-Mesures 17 (2006): 26-28.

Vary, Alex. "Acousto-Ultrasonics - Retrospective Exhortation with Bibliography." Materials Evaluation 49, no. 5 (1991).

Two-component Injection Molding of Molded Interconnect Devices

Jyun-yi Chen, Wen-Bin Young*1

Department of Aeronautics and Astronautics, National Cheng Kung University
Tainan, 70101, Taiwan, ROC

*1youngwb@mail.ncku.edu.tw

Abstract

Molded Interconnect Device (MID) can be defined as an injection-molded plastic part combining with electrical and mechanical functions in a single device. This study is to examine the application of micro injection molding technology to the two-component molding process for the MID fabrication. The process involves the first shot of a plastic component with channel patterns on the surface; while the second shot by micro injection molding technology is applied to fill the channel with the plateable plastics. The effects of the micro injection molding process parameters on filled line width of the two-component MID will be investigated. It is concluded that, for a MID component, the molding conditions must be designed carefully to keep the thickness variation below the allowable value. It is also found from the experiments that the thickness interference may be in the range from 92 μm to 196 μm to have adequate molding at the second shot.

Keywords

3D-molded Interconnect Devices; Two-component Injection Molded; Electroless Copper Plating

Introduction

The printed circuit board (PCB) is used to mechanically support and electrically connect the electronic components together to achieve the function of the electronic product. Due to the miniature technology in the electronic application, it has been considered the possibility of constructing the electrical connecting on the plastic housing directly to eliminate the extra space for a PCB. Molded Interconnect Device (MID) can be defined as an injection-molded plastic part combing with electrical and mechanical functions in a single device. The technology originated in 1980s and was employed to many applications in electronic communication, health care, and automotive industries because of its potential to reduce the number of components and compact in size. Feldmann and Gerhard investigated the problems related to soldering on thermoplastic substrate. Feldmann and Krimi presented two placement systems that enabled 3D PCB with surface mounting devices on inclined planes. Islam, et al. demonstrated how the MID technology can be used for industrial products to achieve shorter process chain and reduce the number of components. Macary and Hamilton introduced the MID process using the laser direct structuring and the existing applications.

The process of MID can be roughly divided into the injection molding of the plastic component and fabrication of the metal traces. The metal traces are served as the electrical circuit on the plastic substrate. There are several major methods for fabrication of the circuit traces on the plastic substrate as two-component injection molding, hot stamping, photo lithography, in-mold circuit film, and laser direct structuring (LDS). The LDS process is the most flexible process that is to apply a laser beam to the traces of a plastic molded component containing metallic particles, followed by electroless deposition of metals. Islam, et al. showed that the success of the LDS process is heavily dependent on the choice of material. In two-component injection molding, the plateable and non-plateable plastics are molded together by injection molding. Metallization process is applied on the plateable plastic to form the circuit traces. The photo lithography can construct the circuit traces on the plastic component by film deposition followed by plating, but is mostly used in the flat circuit patterning. The hot stamping and in-mold circuit film apply the circuit traces directly on to the plastic parts.

This study is to examine the application of micro injection molding technology to the two-component molding process for the MID fabrication. The process involves the first shot of a plastic component with channel patterns on the surface. The second shot by micro injection molding technology is applied to fill the channel with the plateable plastics. The process steps are shown in Fig. 1. On the left hand side, the plastic component is molded with the first molding tool and the molding of the traces is shown on the right hand side with the second molding tool. In order to study the moldability of the traces on the plastic component, a simple straight channel is used as the trace pattern in this study. Experiments are designed to mold channels on a plastic substrate with different widths from 200 μm to 1000 μm, and the channel depth is set to 500 μm. The effects of the injection molding process parameters on filled line width of the two-component MID will be investigated.

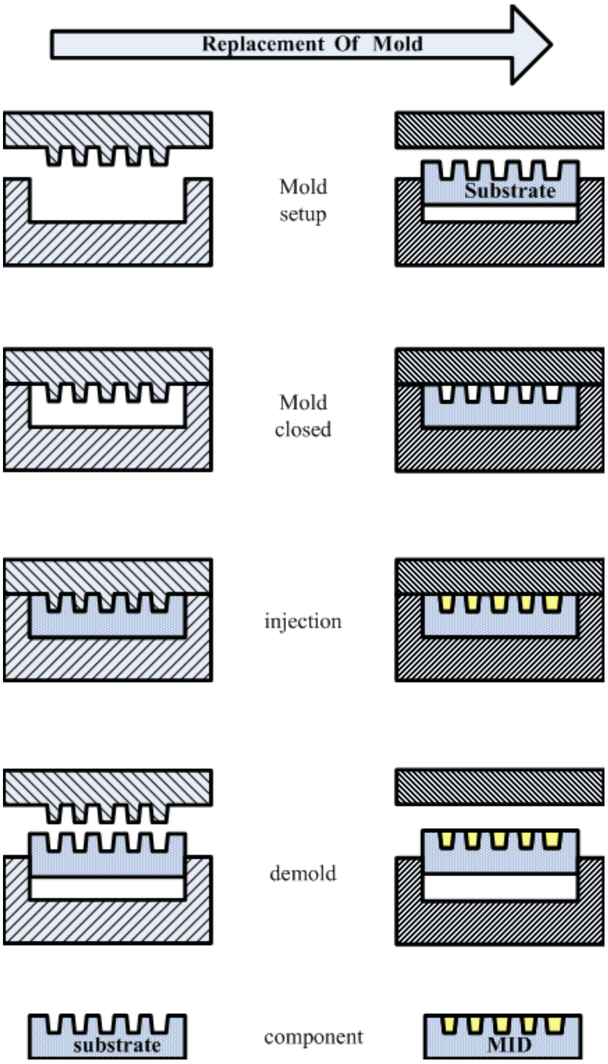

FIG. 1 FABRICATION STEPS OF THE TWO COMPONENT INJECTION MOLDING PROCESS FOR MID

Experimental

The objective of this experimental study is to identify two issues involved in the two-component injection molding. The first is to determine the suitable range for the dimensional interference in the design of the second molding tool. In the two component injection molding, the plastic part will be imbedded into mod during the second shot as shown in Fig. 1. If the plastic part is too thin for the second mold, a flash problem will occur during the injection. On the other hand, if the plastic part is too thick, the mold cannot be closed without crashing the plastics part as shown in Fig. 2. Therefore, a dimensional interference between the second mold and the plastic part must be carefully designed. In this study, it will be attributed as the thickness interference. The second issue is to investigate the filling length in the channel in the second shot. This will be used as a guide for the design of filling gates in molding a circuit trace in the plastic part.

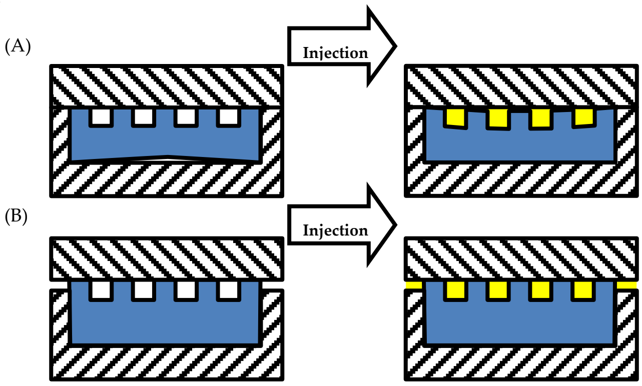

FIG. 2 THE EFFECT OF THE DIMENSION OF THE PLASTIC PART ON THE FILLING OF THE SECOND SHOT. (A) TOO THIN (B) TOO THICK

At the first shot, a two-plate mold is used in this study. The movable mold platen has two rectangular cavities with dimensions in 14x14x3 mm and the fixed mold platen has two rectangular mold inserts with nine channels on the surface as shown in Fig. 3(a). The channels have the dimension of 14 mm in length and 0.5 mm in thickness. Their width ranges from 0.2 to 1 mm by 0.1 mm increment. Another two-plate mold is used for the second shot as shown in Fig. 3(b). The mold has two rectangular cavities with dimensions in 14x14x2.9 mm in the moving side and mold inserts with a flat surface on the fixed side. In the other set of the mold, the cavity height of the first shot mold is changed to 1.5 mm in the subsequent study in order to improve the smoothness of the molded plastic substrate. The cavity height for the second shot mold is changed to 1.374 mm correspondingly.

(A) (B)

FIG. 3 (A) THE INJECTION MOLDING TOOL FOR THE FIRST SHOT (B) THE INJECTION MOLDING TOOL FOR THE SECOND SHOT

Materials used in the molding experiments are polycarbonate PC-110 for the non-plateable plastic and ABS PA-727 for the plateable traces (from Chi Mei Corporation, Taiwan). The base process conditions for the first shot are set as: melting temperature is 320 ℃, mold temperature is 110 ℃, ram speed is 20 mm/s, packing pressure is 80 MPa, packing time is 10 seconds, and cooling time is 10 seconds; while those conditions for the second shot are set as: melting temperature is 230 ℃, mold temperature is 90 ℃, ram speed is 60 mm/s, packing pressure is 80 MPa, packing time is 10 seconds, and cooling time is 10 seconds. The component after second shot can be plated by electroless plating to deposit the copper on the channel surface. A typical component after metallization is shown in Fig. 4.

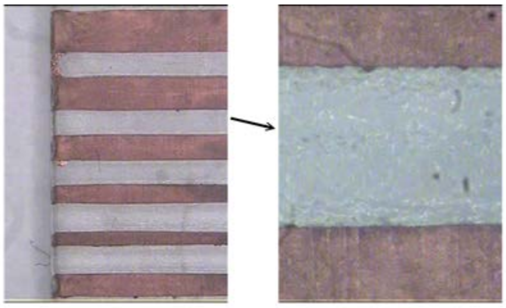

FIG. 4 A TYPICAL COMPONENT AFTER ELECTROLESS PLATING COPPER ON THE CHANNELS

Molding of the Plastic Substrate

As shown in Fig. 2, the interference of the thickness between the plastic substrate and the cavity of the mold in second shot will affect the filling in the channels. In the design of the second shot mold, the cavity height is less than that of the mold in the first shot. If everything is perfect in dimension, 0.1 mm and 0.126 mm thickness interferences are expected for two sets of the molds. However, because of the nature of the plastics, dimension variation is expected in the first shot. Therefore, investigation of the thickness variation of the first molding substrate is performed before start of the second molding.

Due to the molding process, the thickness of the plastic substrate will not be uniform. The thicknesses at nine points (A1 to A9) on the substrate were measured on the molded plastic substrate as shown in Fig. 5. Different packing pressures (from 20 MPa to 160 MPa with 20 MPa in increment) were used for the molding. The resulting thickness on each point is shown in Fig. 6. It is noticed that the thickness at the center of the substrate (A5) is much less than that at the other positions. This is believed to be caused by the knock-out pin at that position. Thickness at the position far from the gate is generally smaller due to the less packing effect. Also, the thickness is not uniform along the direction perpendicular to the channels, which is attributed to the non-uniform channel structures on the substrate.

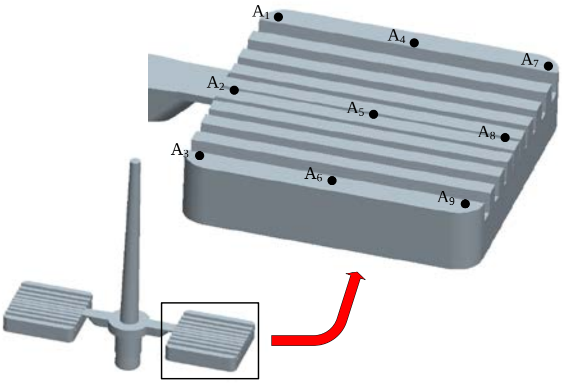

FIG. 5 THE PLASTIC PART OF MID WITH CHANNEL TRACES

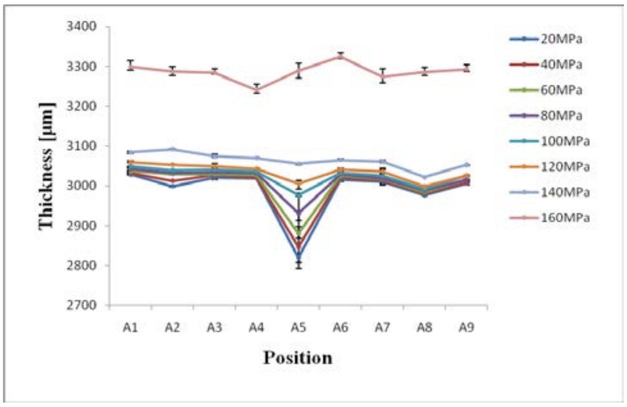

FIG. 6 THICKNESS OF THE SUBSTRATE MOLDED UNDER DIFFERENT PACKING PRESSURES AT DIFFERENT POSITIONS

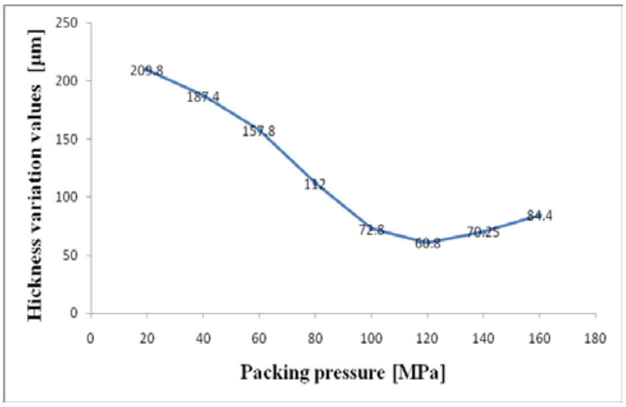

FIG. 7 THICKNESS VARIATION OF THE SUBSTRATE MOLDED UNDER DIFFERENT PACKING PRESSURES FOR A SUBSTRATE OF 3 mm IN THICKNESS

The thickness variation of the substrate is defined as the difference between the maximum and minimum values of thicknesses measured at the nine positions. Figure 7 shows the thickness variation of the substrate molded under different packing pressures. It is noticed that the thickness variation has the lower value as the packing pressure is around 120 MPa. As the plastic substrate is embedded into the mold for a second shot, a flash problem occurs if the thickness variation exceeds about 100 μm. The material of ABS will flow over the channels and cover the substrate as shown in Fig. 8. Therefore, it is necessary to control the thickness variation in the first shot of the plastic substrate in order to eliminate the flash problem.

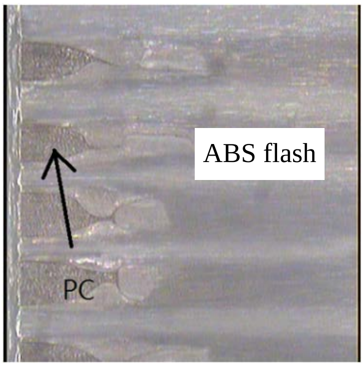

FIG. 8 FLASH OF THE ABS MATERIAL AS THE THICKNESS VARIATION OF THE PC SUBSTRATE IS TOO LARGE

One way to improve the thickness uniformity of the substrate is to reduce the total thickness. Another mold with a smaller cavity height, 1.5 mm, is used for the molding of the substrate. The resulting thickness variation is shown in Fig. 9 under different packing pressures. The thickness variation is quite low as compared to the previous case. It is demonstrated that the thickness of the substrate will affect the uniformity of the molding part. On the other hand, if the thickness of a MID component is selected based on other considerations, the molding conditions must be designed carefully to keep the thickness variation below the allowable value (about 100 ◎ m in this case).

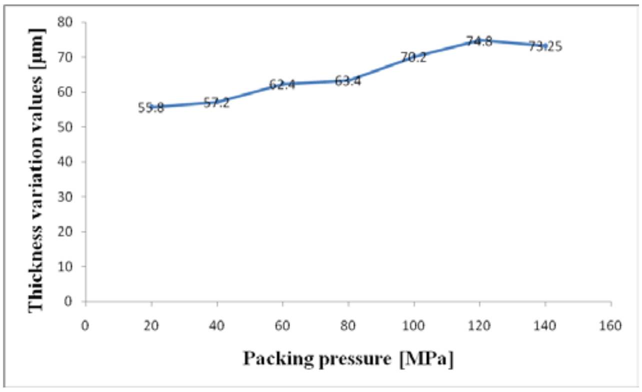

FIG. 9 THICKNESS VARIATION OF THE SUBSTRATE MOLDED UNDER DIFFERENT PACKING PRESSURES BY USING A MOLD WITH CAVITY HEIGHT 1.5 mm

Thickness Interference

The thickness interference is defined as the thickness difference between the substrate and mold cavity as shown in Fig. 10. In the second shot to fill the small channels for circuit traces, the substrate embedded into the mold cavity usually has a thickness larger than the cavity height to ensure a tight contact with the mold surface. As the mold closes and compresses the surface of the substrate, the channel will change in shape due to the deformation of the surface materials. Before the second shot, the dimensions of the channels at the molded plastic substrate are measured first. Table 1 lists the average value of the channel width at the substrate as compared to the original dimension at the mold.

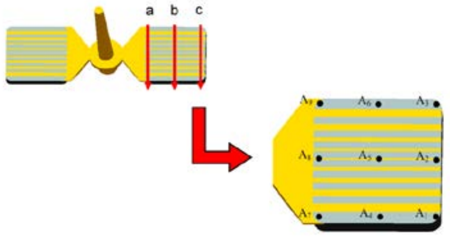

δ: thickness interference; w: channel width

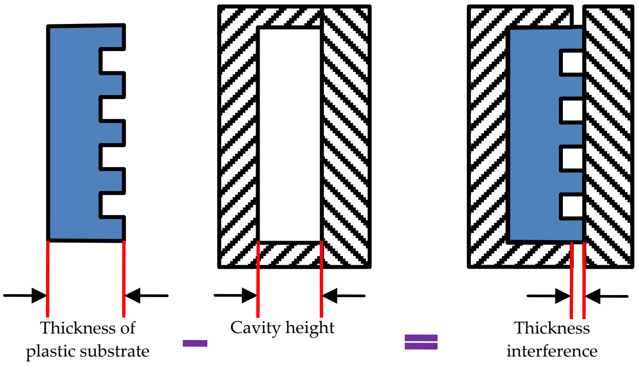

FIG. 10 THICKNESS INTERFERENCE IS DEFINED AS THE DIFFERENT BETWEEN THE SUBSTRATE AND MOLD CAVITY IN THICKNESS

TABLE 1 THE CHANNEL DIMENSION AT THE MOLDED PLASTIC SUBSTRATE USING THE MOLD WITH CAVITY 14 MM LENGTH

Channel width at the mold	Channel width at the plastic substrate
200 μm	182 μm
300 μm	350 μm
400 μm	421 μm
500 μm	523 μm
600 μm	632 μm
700 μm	715 μm
800 μm	822 μm
900 μm	907 μm
1000 μm	1013 μm

As mentioned earlier, the thickness variation must be smaller than 100 μm to eliminate the problem of flash during the filling. Therefore, only the substrates molded at a packing pressure higher than 100 MPa is acceptable for the second shot if the designed thickness is 3 mm. For the mold with a cavity in a thinner thickness, 1.5 mm, the resulted substrates molded under different packing pressures can all be used in the second shot. The typical results of the second shot for the channels are listed in Table 2 for the substrate molded under 80 MPa packing pressure and a designed thickness 1.5 mm. The left column shows the channel width of the plastic substrate and the mold cavity (in parentheses). The channel width on the part surface after the second shot will change due to the deformation of the substrate after mold compression. There are nine positions where the thickness interferences are measured (A1-A9). A large value of thickness interference will cause the substrate to deform significantly and leads to the smaller channel width on the surface. If the interference is too large, the channel may deform a lot and close at the surface. It is concluded from the experiments that the thickness interference may be in the range from 92 μm to 196 μm to have adequate molding at the second shot. If the interference is too small, the same flash problem will also occur. As the interference is too large, the mold compression will destroy the channel entirely.

TABLE 2 THE RESULTING CHANNEL WIDTH AFTER SECOND SHOT AND THE THICKNESS INTERFERENCE

Channel width of the plastic substrate	along a	δ(μm)	along b	δ(μm)	along c	δ(μm)
1013(1000)	1025	164 (A_9)	900	184 (A_6)	850	196 (A_9)
822(800)	845		715		710	
632(600)	655		535		500	
421(400)	480		340		---	
182(200)	275	147 (A_8)	---	210 (A_5)	---	209 (A_2)
350(300)	385		---		---	
523(500)	565		390		375	
715(700)	760		600		610	
907(900)	920	171 (A_7)	760	191 (A_4)	765	204 (A_1)
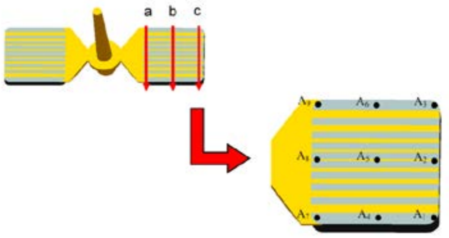						

If the mold with the cavity 1.5 mm in height is considered, the corresponding mold for the second shot has a cavity 1.374 mm in height. The cross sections of the molded channels after second shot are shown in Fig. 11 at the position near the far end from the gate. The figure shows cross sections of channels with the width of 1000, 900, and 500 μm. The thickness inference is also shown under each picture for the channel. Notice that the interference is calculated as the difference between the measured thickness of the substrate and the cavity height of the second shot mod. For the case with a lower value of interference, the cross section of the channel shows a wider open at the surface. This is caused by the original circular fillet at the cross section of the channel in the mold due to the machining process. As the interference is larger, the channel will deform because of the compression on the surface of the substrate as the mold closes. For interference near or above 196 μm, the cross section of the channel deforms more and forms a narrow neck at the middle of the channel. Therefore, an adequate selection of interference is necessary to keep the channel shape for the filling process at the second shot. This selection can be attributed to the control of the part thickness of the first shot and design of cavity thickness for the second-shot mold.

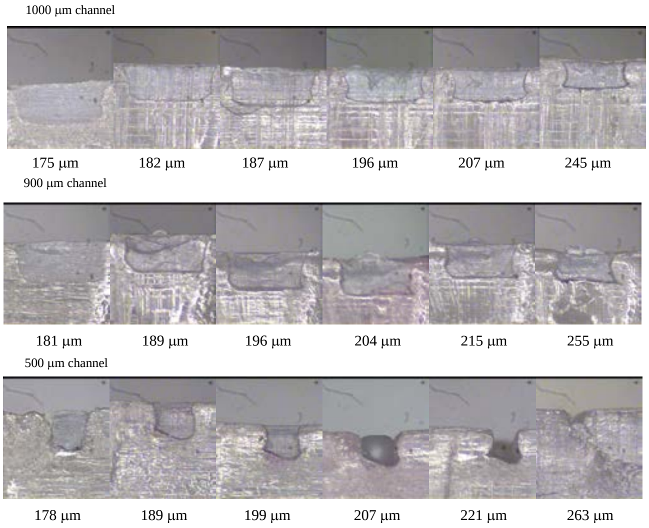

FIG. 11 CROSS SECTION OF THE CHANNELS, 1000, 900, 500 μm IN WIDTH, AND THE THICKNESS INTERFERENCE

Filling Length of the Channels

TABLE 3 THE CHANNEL DIMENSION AT THE MOLDED PLASTIC SUBSTRATE USING THE MOLD WITH CAVITY 90 mm LENGTH

Channel width at the mold	Channel width at the plastic substrate
400μm	338 μm
500μm	448 μm
600μm	539 μm
700μm	644 μm
800μm	735 μm
900μm	875 μm
1000μm	978 μm

In the filling of the channels in the second shot, most of the channels can be filled completely as the mold cavity is only 14 mm in length. In order to study the capability of the filling length in the second shot, a mold with larger length in cavity, 90 mm, is constructed. The mold has channels with width from 400 μm to 1000 μm with 100 μm in increment. The resulting channel width of the molded plastics substrate at the first shot is listed in Table 3.

The filling length on the channels of the plastic substrate at the second shot is shown in Fig. 12 for different mold temperature. It can be seen that the mold temperature must exceed 70 ℃ in order to have a longer filling length. At the second shot, the filling starts as mold closes after the plastic substrate is imbedded into the mold cavity. Therefore, the plastic substrate is actually at the room temperature and cools the filling melt very fast. A higher mold temperature improves the filling of the second shot in the plastic channels. The filling length on the channels of the plastic substrate for different packing pressures shown in Fig. 13 increases with the packing pressure as it increases above 70 MPa. For the channel narrower than 400 μm, the filling length only increases slightly with the packing pressure. In the application for circuit traces, if long trace is necessary, multiple gates are necessary to fill the circuit in the second shot.

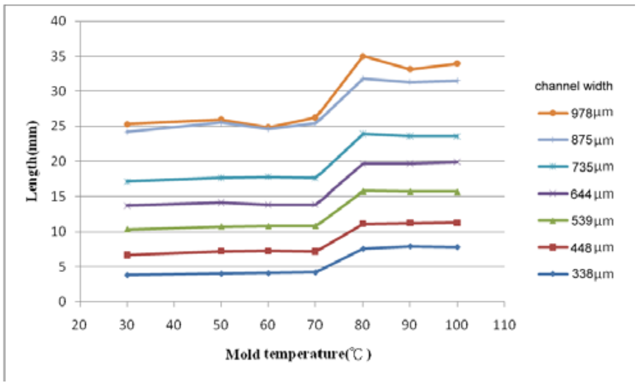

FIG. 12 THE FILLING LENGTH OF CHANNELS ON THE PLASTIC SUBSTRATE FOR DIFFERENT MOLD TEMPERATURES

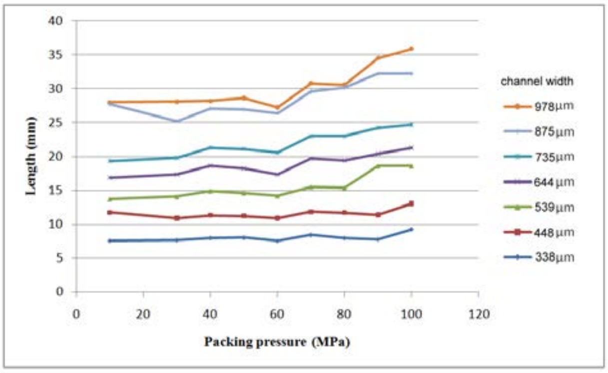

FIG. 13 THE FILLING LENGTH OF CHANNELS ON THE PLASTIC SUBSTRATE FOR DIFFERENT PACKING PRESSURES

Conclusions

Application of micro injection molding technology to the two-component molding process for the MID fabrication has been investigated. The process involves the first shot of a plastic component with channel patterns on the surface. While the second shot by micro injection molding technology is applied to fill the channel with the plateable plastics. Experiments are designed to mold channels on a plastic substrate with different widths from 200 μm to 1000 μm, and the channel depth is set to be 500 μm. The effects of the micro injection molding process parameters on channel filling of the two-component MID will be investigated. It is demonstrated that the thickness of the substrate will affect the uniformity of the molding part. For a MID component, the molding conditions must be designed carefully to keep the thickness variation below the allowable value (about 100 μm in this case). It is also found from the experiments that the thickness interference might be in the range from 92 μm to 196 μm to have an adequate molding at the second shot. If the interference is too small, the same flash problem will occur. As the interference is too large, the mold compression will destroy the channel entirely.

ACKNOWLEDGMENT

The authors would like to thank for the financial support from National Science Council in Republic of China under the contract number of NSC 99-2221-E006-047-MY2. The authors also would like to thank for the collaboration of Far East University, Taiwan for providing the related equipments for the experiments

REFERENCES

Amend, P., Pscherer, C., Rechtenwald, T., Frick, T., Schmidt, M. “A fast and flexible method for manufacturing 3D molded interconnect devices by the use of a rapid prototyping technology.” Physics Procedia 5 (2010): 561-72.

Eberhardt, W., Gerhäußer, T., Giousouf, M., Kück, H., Mohr, R., Warkentin, D. “Innovative concept for the fabrication of micromechanical sensor and actuator devices using selectively metallized polymers.” Sensors and Actuators A: Physical 97-98 (2002): 473-477.

Feldmann, K. and Gerhard, M. “Direct Soldering of Electronic Components on Molded Devices.” CIRP Annals - Manufacturing Technology 44 (1995): 19-22.

Feldmann, K. and Krimi, S. “Alternative Placement Systems for Three-Dimensional Circuit Boards.” CIRP Annals -

Manufacturing Technology 47 (1998): 23-26.

Islam, A., Hansen, H. N., Tang, P. T., Jorgesen, M. B., Orts, S. F. “Two component injection molding for MID fabrication.” Prodeedings of ANTEC 2009 Annual Technical Conference, Chicago, USA. 2009.

Islam, A., Hansen, H. N., Tang, P. T., Sun, J. “Process chains for the manufacturing of molded interconnect devices.” International Advanced Manufacturing Technology 42 (2009): 831-841.

Macary, R. L. and Hamilton, R. “SelectConnect(TM) process for metallizing circuits on molded parts and components.” Metal Finishing 108 (2010): 35-37.

The Effects of Pyrolysis Conditions on the Chemical and Physical Properties of Rice Husk Biochar

Nattaporn Prakongkep*[1], Robert J. Gilkes[2], Wanpen Wiriyakitnateekul[3], Apinya Duangchan[4], Timtong Darunsontaya[5]

[1,2]School of Earth and Environment, University of Western Australia, Crawley, 6009, Australia

[3]Office of Science for Land Development, Land Development Department, Phahon Yothin Road, Chatuchak, Bangkok 10900, Thailand

[4]Department of Chemical Engineering, Faculty of Engineering, Kasetsart University, 50 Phahon Yothin Road, Chatuchak, Bangkok, 10900, Thailand

[5]Department of Soil Science, Faculty of Agriculture, Kasetsart University, 50 Phahon Yothin Road, Chatuchak, Bangkok, 10900, Thailand

*[1]asoil@hotmail.com; [2]bob.gilkes@uwa,.edu.au; [3]wpenldd@gmail.com; [4]fengapd@ku.ac.th; [5]kratig_na@hotmail.com

Abstract

Our research has identified the location and mineralogy of plant nutrients in rice husk biochar prepared by three procedures, involving pyrolysis at a low temperature (<550°C). pH, EC, C, N, ash percentage, chemical composition and mineralogy have been measured. Scanning electron microscopy (SEM) analysis determined the morphology and chemical composition of materials in rice husk biochar.

Rice husk biochar is highly alkaline (8.5-9.7) with a high ash content (36-44%) and high silicon, sodium, potassium, calcium and magnesium contents, it contains archerite (KH_2PO_4), calcite ($CaCO_3$), chlorocalcite ($KCaCl_3$), kalicinite ($KHCO_3$), pyrocoproite ($K_2MgO_7P_2$), struvite ($KMgPO_4.6H_2O$), sylvite (KCl) and vaterite ($CaCO_3$). These minerals are at least moderately soluble in water and are sources of plant nutrients when biochar is applied to soil. Mineral grains (sylvite, carbonates and phosphates) are mainly present between relict vascular bundles and parenchyma cells where dissolved elements in xylem and phloem are precipitated during pyrolysis.

Silica, a major constituent of rice husk biochar, is concentrated in outer epidermis cells including protuberances and hairs (trichomes) and also present in the inner epidermis. Rice husk biochar includes a mixture of amorphous and crystalline forms of silica resembling cristobalite and tridymite. It provides a readily soluble form of both lime and plant nutrient elements so its use on acid, infertile soil should be encouraged.

Keywords

Rice Husk Biochar; Slow Pyrolysis; Low Temperature; Chemical Composition

Introduction

Rice is a primary source of food for many people with annual global paddy rice production being about 580 million tonnes. Rice husk, a by-product of rice processing with approximately 140 million tonnes produced each year, constitutes a significant waste disposal problem (Tarley and Arruda, 2004; Kalderis et al., 2008). Thailand produces around 21-26 million tonnes of rice per year creating about 5.4 million tonnes of rice husks (OAE, 2003). Farmers use rice husk as fuel and for pyrolysis producing bio-oil, gases and biochar. Application of biochar to soil may have diverse agronomic benefits and may also be eligible for carbon credits (Sohi, et al., 2010). Biochar contains plant nutrient elements but the amounts, speciation and availability to plants of these elements is poorly understood, which is the subject of this paper.

The conditions imposed under controlled pyrolysis affect biochar properties. Pyrolysis temperature is the most significant process parameter with the carbon content of biochar created at different temperatures being inversely related to biochar yield (Okimori, et al., 2003). It has been suggested that biochar created at low temperature may be most suitable for controlling the release of plant nutrients from biochar (Day et al., 2005). In the present work, biochar was prepared from rice husks at a low temperature (<550°C) under laboratory conditions and also under conditions employed by farmers.

Pyrolysis was performed at Kasetsart University (fixed bed reactor) and the Land Development Department (cylinder reactor) at 400-550°C which is close to the temperature of the traditional kiln (~350°C). The aim of this work was to characterize rice husk biochar, including morphology, mineralogy and chemical composition to identify if the method of manufacture affects these properties.

Materials and Methods

Manufacture of Rice Husk Biochars

A bulk rice husk sample was obtained from a commercial rice mill that processes jasmine rice. Pyrolysis was carried out using KU (Kasetsart University) and LDD (Land Development Department) equipment and in a traditional farmers kiln under limited oxygen atmosphere as shown in Fig. 1. The KU reactor produced biochar from a load of 700 cm^3 of biomass at 400-550°C, 10-20°C/min heating rate and N_2 was added into the reactor at 200 cm^3/min flow rate with a 1 hr residence time (Fig. 1a). The LDD reactor produced biochar at 400°C with a 300 cm^3/min N_2 flow rate (Fig. 1b) from a load of 5,000 cm^3 biomass. Biochar was produced in a traditional farmer kiln shown in Fig. 1c where organic waste fuel is burnt in an outer metal cylinder to heat the rice husks in the inner cylinder from which air is excluded. The operating temperature is approximately 350°C with a load of 2,500 cm^3 biomass (Figu. 1c).

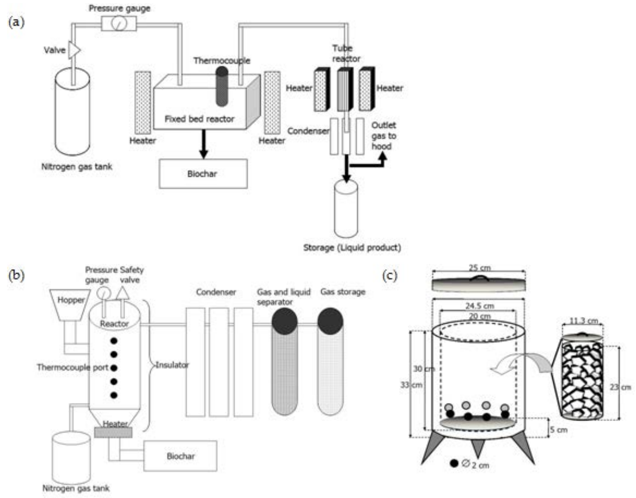

FIG. 1 EQUIPMENT USED TO MANUFACTURE BIOCHAR (a) KASETSART UNIVERSITY EQUIPMENT (KU REACTOR, 370-550°C WITH 200 CM^3 MIN^{-1} N_2 FLOW RATE), (b) LAND DEVELOPMENT DEPARTMENT EQUIPMENT (LDD REACTOR, 400°C WITH 300 CM^3/MIN N_2 FLOW RATE), AND (c) TRADITIONAL KILN (UNCONTROLLED TEMPERATURES ~350°C WITH LIMITED OXYGEN).

X-ray Diffraction Analysis

The mineral composition of ground rice husk biochar was determined by conventional X-ray diffraction (CXRD) analysis using a Philips PW-3020 diffractometer with a graphite diffracted beam monochromator (CuKα, 50 kV, 20 mA) scanning from 4 to 70° 2θ, using a step size of 0.02° 2θ and a scan speed of 0.04° 2θ sec^{-1}.

Thermal Analysis

Thermogravimetric data were obtained with a Perkin Elmer STA 6000 with air flowing at 20 mL/min.. Ground rice husk biochar powder was mixed with aluminium oxide (1:1, v/v) before analysis to avoid artefacts in data due to shrinkage of samples during combustion The temperature was raised from 30°C to 100°C at 10°C/min then kept at 100°C for about 10 mins. Then the temperature was increased from 100°C to 1000°C at a 10°C/min heating rate while DTA and TGA data were recorded.

Chemical Analysis

Rice husk biochars were ground in a pestle and mortar for chemical and thermal analysis. Biochar pH and electrical conductivity (EC) were measured using a 1: 5 solid: MilliQ (MQ) water (by volume) extraction with shaking end-over-end for 12 hr. The total water soluble elements in biochar were determined by extracting the biochar with MQ water (0.3 g biochar per 10 mL MQ water), shaking end-over-end for 12 hr, and the extracted solutions were analysed by ICP-OES. The ash content of biochars was determined by dry combustion in a ventilated muffle furnace at 600°C overnight. Total carbon and nitrogen concentrations were determined using a Vario Macro elemental analyzer. Total element concentrations were determined by digesting biochar ash in 10% HCl, with analysis of the solutions by ICP-OES (Perkin-Elmer).

Microanalysis

For observation of biochar morphology with a scanning electron microscope and element mapping using EDS (energy dispersive spectroscopy), fractured rice husk biochar particles were placed on a double-sided carbon tape, adhered to an aluminium stub and were coated with carbon. The samples were observed with a JEOL 6400 SEM operated at an acceleration voltage of 15 kV. SEM images of biochar enabled recognition of plant organs that have been altered to assemblages of carbon and mineral grains. EDS provided quantitative analyses of micronsize volumes enabling the determination of the chemical composition of mineral grains on the surface and inside voids in biochar.

Results and Discussions

Mineralogical Properties

The mineralogical composition and the solubility in water of the mineral constituents of rice husk biochars are shown in Table 1 and Fig. 2. Amorphous (noncrystalline) silica, a major constituent of these biochars, generates a broad XRD peak centred at 2θ ~ 22.5°, which can be attributed to the presence of disordered cristobalite (Fig. 2) (Liou, 2004) and amorphous carbon also contributes to this broad peak (Radhika and Sugunan, 2006; Chen et al., 2011).

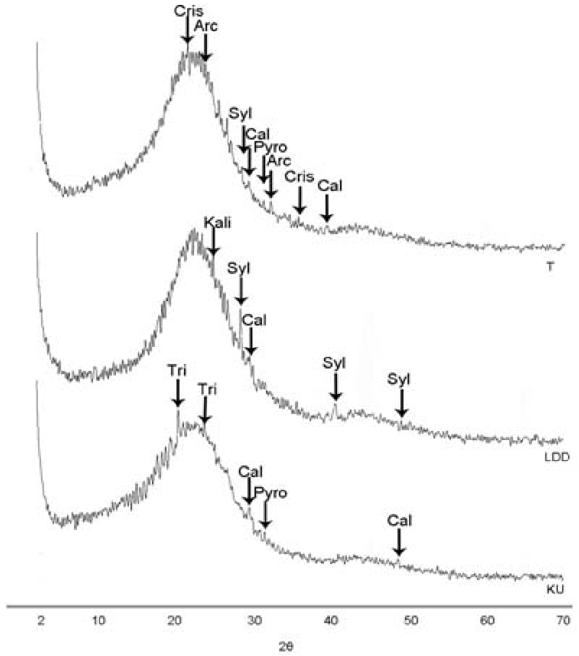

FIG. 2 CONVENTIONAL XRD PATTERNS OF RICE HUSK BIOCHAR (KU=RICE HUSK BIOCHAR FROM KASETSART UNIVERSITY EQUIPMENT, LDD=RICE HUSK BIOCHAR FROM LAND DEVELOPMENT DEPARTMENT EQUIPMENT AND T=TRADITIONAL RICE HUSK BIOCHAR) (ARC=ARCHERITE, CAL=CALCITE, CRI=CRISTOBALITE, KALI = KALICINITE, PYRO=PYROCOPROITE, SYL=SYLVITE, TRI=TRIDYMITE). THE BROAD REFLECTION CENTRED AT ABOUT 22° 2Θ IS DUE TO AMORPHOUS SILICA AND CARBON.

Archerite (KH_2PO_4), calcite ($CaCO_3$), chlorocalcite ($KCaCl_3$), kalicinite ($KHCO_3$), pyrocoproite ($K_2MgO_7P_2$), struvite ($KMgPO_4.6H_2O$), sylvite (KCl) and vaterite ($CaCO_3$) are variously present in rice husk biochar samples. All these minerals are soluble in water to different extents except for cristobalite (SiO_2) and tridymite (SiO_2) (Table 1). It is evident that the solubility in soils of elements in these biochars will depend on the mineral species containing the elements. For example, K in sylvite will readily dissolve when biochar is applied to soil but K in struvite will only be slowly soluble. Calcite ($CaCO_3$), struvite ($KMgPO_4.6H_2O$) and tridymite (SiO_2) are present in all these biochars. Sylvite (KCl), kalicinite ($KHCO_3$) and vaterite ($CaCO_3$) only occur in LDD biochar. This difference may be a consequence of the different equiptment and procedures used to prepare the biochars.

Thermal Stability

TGA and derivative thermogravimetry DTG curves for the biochars shown in Fig. 3 similar show major exotherm and weight loss at 400-550°C due to oxidation of biochar carbon in the flowing air. The DTGA and DTA curves for LDD biochar have a split DTA/DTGA peak (475°C, 513°C) and an additional peak at 513°C. This difference presumably relates a different (lesser) extent of pyrolysis of the LDD sample.

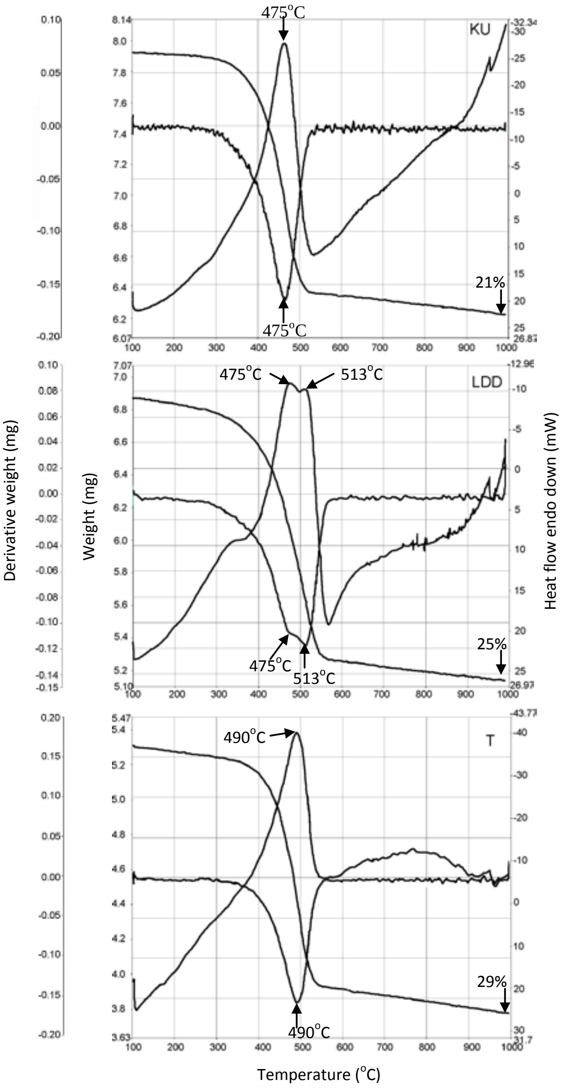

FIG. 3 TGA, DTG AND DTA CURVES FOR RICE HUSK BIOCHAR (KU = RICE HUSK BIOCHAR FROM KASETSART UNIVERSITY EQUIPMENT, LDD = RICE HUSK BIOCHAR FROM LAND DEVELOPMENT DEPARTMENT EQUIPMENT AND T = TRADITIONAL RICE HUSK BIOCHAR). ALUMINIUM OXIDE WAS MIXED WITH BIOCHAR (1:1, V/V). EXOTHERMS AND WEIGHT LOSS ARE DUE TO OXIDATION OF CARBON IN BIOCHAR.

Chemical Properties

Table 2 presents the chemical composition of three rice husk biochars. They have total ash contents ranging between 36-44 wt% and similar carbon contents (46-57%). The higher C content of LDD biochar is consistent with the lower degree of pyrolysis indicated by TGA analysis. EC values for KU and T rice husk biochars are similar but LDD biochar has a much higher value possibly because it contains more of the highly soluble minerals kalicinite, sylvite and vaterite (Table 1).

In addition to, C and N the major constituents of biochars are Si, Ca, Mg, Na, K and P. Other elements are present at minor to trace concentrations. The slightly elevated concentrations of Fe, Cr, Ni and Ti in LDD biochar presumably originated in the iron and steel present in the LDD reactor. The elevated Zn concentration in T biochar may originate in galvanised iron used in this equipment.

The concentration of water soluble elements and the proportion of the total element concentration that is soluble are shown in Tables 3 and 4, respectively. Much K is water soluble because rice husk biochar contains the soluble potassium compounds [archerite (KH_2PO_4), chlorocalcite ($KCaCl_3$), kalicinite ($KHCO_3$), pyrocoproite ($K_2MgO_7P_2$), and sylvite (KCl)]. Potassium in struvite will be only slightly soluble (Table 1). Sulphur is moderately soluble but the forms of S in biochar are not known. Most of the plant nutrient elements in biochar (Ca, Mg, Fe, Mn, Zn, P, S) are quite poorly soluble in water, possibly reflecting the low solubility of minerals at the high pH (8.5-9.7) of the water extract (Table 2).

Anatomical Features and Individual Minerals

Sections of rice husk biochar taken through the entire thickness of the husk provide information on the pseudomorphic preservation of anatomical features for all three methods of biochar manufacture (Fig. 4). Scanning electron microscopy shows that the structure of rice husk biochar faithfully preserves original features of the rice husk. The outer epidermis, layered fibers, vascular bundles, parenchyma cells and inner epidermis and interconnected pores are preserved during the conversion to carbon (Fig. 4). Biochar manufactured by the traditional method (biochar T) has perfectly preserved surface and internal structures (Fig. 4f) whereas rice husk biochar produced on Kasetsart University equipment (KU) has experienced some disruption of the surface and internal structures (Fig. 4b). The porosity provided by the plant cell structure (pore size <10 μm) contributes to the very large specific surface area and high chemical activity of rice husk biochar (Xu et al., 2012). However, much of the surface area is provided by the micropores (< 10 nm pores) in carbon that is not a feature of original husks.

The outer epidermis of rice husk biochars is conspicuously ridged and ridges are punctuated with conical protrusions (Fig. 4). The outer epidermis walls are extremely thick (30-35 μm) (Fig. 4). Hairs are present on the outer epidermis of traditionally prepared rice husk biochar (T) and rice husk biochar manufactured on Land Development Department equipment (LDD) (Fig. 4d, f).

Poorly crystalline silica is a major constituent of rice husk biochar. Much of the silica is present in the outer epidermis cells and concentrated in hair and dome-shaped protrusions (Figs. 5, 6 and 7) and also as dispersed silica inside the husk (Fig. 7). Other minerals (carbonates, phosphates and chlorides) are mainly present between carbonised vascular bundles and parenchyma cells (Figs. 5, 6 and 7). These mineral grains provide x-ray spectra in the SEM that are indicative of individual minerals or mixes of the minerals identified by XRD (Table 1 and Figs. 5, 6 and 7).

TABLE 1 THE COMPOSITION AND SOLUBILITY IN WATER OF MINERAL CONSTITUENTS OCCURRING IN RICE HUSK BIOCHAR. SOLUBILITY VALUES ARE DERIVED FROM THE LITERATURE. THE ABUNDANCE OF THESE MINERALS IN THE THREE BIOCHAR IS INDICATED

Biochars	Formula**	Archerite (KH_2PO_4)	Calcite ($CaCO_3$)	Chlorocalcite ($KCaCl_3$)	Cristobalite (SiO_2)	Kalicinite ($KHCO_3$)	Pyrocoproite ($K_2MgO_7P_2$)	Struvite ($KMgPO_4.6H_2O$)	Sylvite (KCl)	Tridymite (SiO_2)	Vaterite ($CaCO_3$)
	Solubility in water (mg L^{-1})*	Soluble	14	Soluble	Insoluble	224,000	Decomposes	Slightly soluble	238,000	Insoluble	Highly soluble
Rice husk KU		-	x	x	-	-	x	x	-	x	-
Rice husk LDD		x	x	-	-	x	-	x	x	x	xx
Rice husk T		x	x	-	x	-	x	x	-	x	-

KU=biochar from Kasetsart University equipment, LDD = biochar from Land Development Department equipment, T= traditional biochar, - = not detected, x = small, xx = moderate, * Water solubility data from Weast (1983), ** ICDDF (powder data file).

TABLE 2 PROPERTIES AND TOTAL ELEMENTAL COMPOSITION* OF THE RICE HUSK BIOCHARS.

Biochars		Wt loss	Ash	C	N	pH**	EC**	Si	Al	Ca	Mg	Na	K	P	S	Fe	Mn	As	Ba
		(-----------%-------------)					(µs cm^{-1})	(--mg kg^{-1}--)											
Rice husk	KU	62	38	47	0.59	8.5	620	166338	793	2245	900	29628	7999	1033	442	416	249	3	15
Rice husk	LDD	64	36	51	0.91	9.7	3180	149499	500	7804	1840	19086	12519	2162	864	1270	207	nd	63
Rice husk	T	56	44	46	0.63	9.7	833	193748	212	1340	1683	12353	8502	2983	89	220	454	3	23
Biochars								Co	Cr	Cu	Gd	Ge	Ni	Pb	Rb	Sr	Ti	Zn	Zr
								(--mg kg^{-1}---)											
Rice husk	KU							3	9	10	2	5	8	1	18	9	41	31	2
Rice husk	LDD							3	130	24	1	3	19	11	21	18	114	84	7
Rice husk	T							5	4	20	1	6	9	11	78	4	18	309	1

* = digest of biochar ash samples in 10% HCl, measured by ICP-OES and converted to biochar basis, ** = 1:5 H_2O extract on biochar, Wt loss = weight loss on ignition in air at 600°C, nd = not detectable, KU = biochar from Kasetsart University equipment, LDD = biochar from Land Development Department equipment, T = traditional biochar.

TABLE 3 CONCENTRATIONS OF WATER SOLUBLE ELEMENTS* IN RICE HUSK BIOCHAR.

Raw Materials		Al	Na	K	Ca	Mg	P	S	Fe	Mn	Cu	Zn
		(---mg kg^{-1}--)										
Rice husk	KU	0.3	32	1641	59	44	243	73	0.5	9	0.03	0.02
Rice husk	LDD	0.8	710	9903	548	225	129	1118	0.2	0.3	nd	nd
Rice husk	T	0.1	nd	2141	28	341	978	19	0.2	17	nd	0.3

* Biochar samples were extracted by MQ water for 12 hr and analysed by ICP-OES, nd = not detectable, KU = biochar from Kasetsart University equipment, LDD = biochar from Land Development Department equipment, T = traditional biochar.

TABLE 4 THE PROPORTION OF THE TOTAL ELEMENT CONCENTRATION IN RICE HUSK BIOCHAR THAT IS WATER SOLUBLE*.

Raw Materials		Al	Na	K	Ca	Mg	P	S	Fe	Mn	Cu	Zn
Rice husk	KU	0.00	0.00	0.21	0.03	0.05	0.24	0.17	0.00	0.04	0.00	0.00
Rice husk	LDD	0.00	0.04	0.79	0.07	0.12	0.06	>1.00	0.00	0.00	0.00	0.00
Rice husk	T	0.00	0.00	0.25	0.02	0.20	0.33	0.21	0.00	0.04	0.00	0.00

* Biochar samples were extracted by MQ water for 12 hr and analysed by ICP-OES, KU = biochar from Kasetsart University equipment, LDD = biochar from Land Development Department equipment, T = traditional biochar.

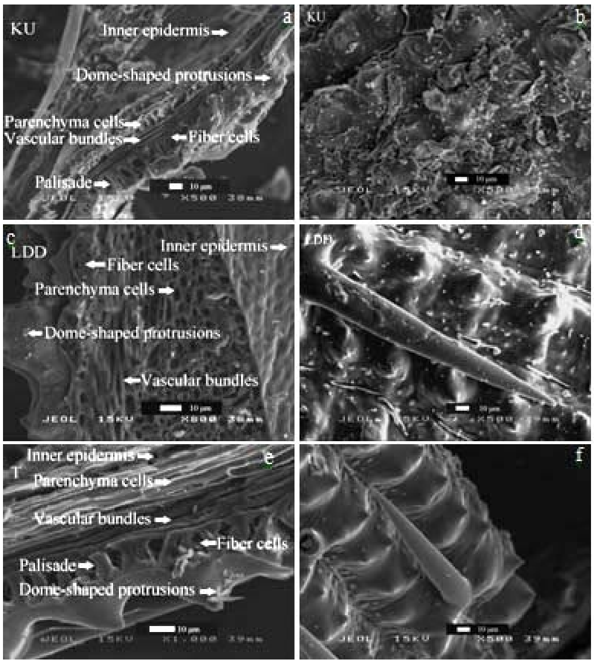

FIG. 4 SCANNING ELECTRON MICROGRAPHS OF (a) RICE HUSK BIOCHAR (b) OUTER EPIDERMIS FROM KASETSART UNIVERSITY EQUIPMENT (KU), (c) RICE HUSK BIOCHAR (d) OUTER EPIDERMIS FROM LAND DEVELOPMENT DEPARTMENT EQUIPMENT (LDD) AND (e) RICE HUSK BIOCHAR (f) OUTER EPIDERMIS FROM THE TRADITIONAL KILN (T). THE WELL PRESERVED RELICT CARBONISED PLANT ORGANS ARE INDICATED.

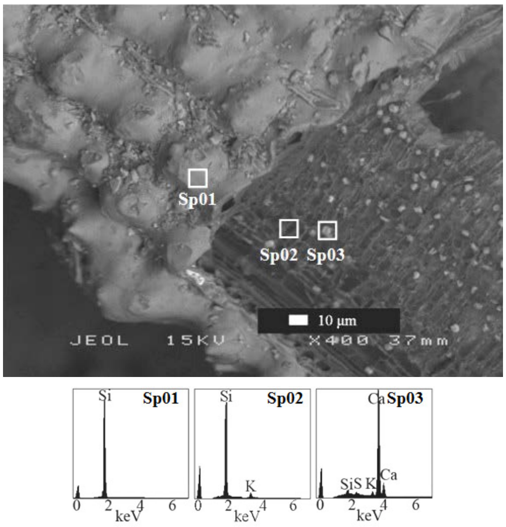

Atomic percent				
Sp	Si	S	K	Ca
Sp01	100	-	-	-
Sp02	93	1	6	-
Sp03	3	2	3	92

FIG. 5 BACKSCATTERED ELECTRON MICROGRAPH, X-RAY SPECTRA AND ANALYSES OF INORGANIC PARTICLES EXPRESSED AS ATOMIC PERCENT FOR RICE HUSK BIOCHAR FROM KASETSART UNIVERSITY EQUIPMENT (KU) (Sp01 = AMORPHOUS SILICA, Sp02 = MOSTLY AMORPHOUS SILICA AND $KHCO_3$ AND Sp03 = MOSTLY $CaCO_3$, LITTLE $KHCO_3$, $CaSO_4$ AND SiO_2)

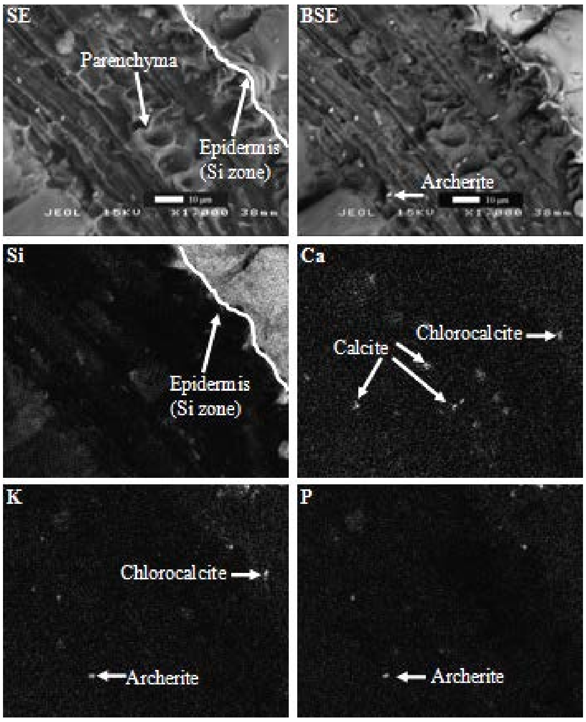

FIG. 6 SECONDARY AND BACKSCATTERED ELECTRON SCANNING MICROGRAPHS AND ELEMENT MAPS FOR RICE HUSK BIOCHAR FROM LAND DEVELOPMENT DEPARTMENT EQUIPMENT (LDD) SHOWING A LAYER OF SILICA AND GRAINS OF CALCITE, ARCHERITE AND CHLOROCALCITE IN THIS SAMPLE.

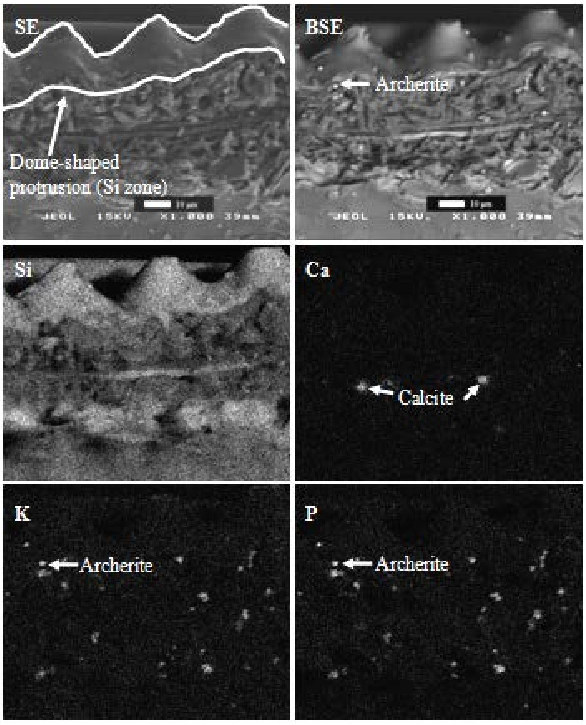

FIG. 7 SCONDARY AND BACKSCATTERED SCANNING ELECTRON MICROGRAPHS AND ELEMENT MAPS FOR TRADITIONAL RICE HUSK BIOCHAR (T) CONTAINING CALCITE AND ARCHERITE.

Conclusions

A aim of this work was to develop an understanding of the speciation of plant nutrient elements in biochar created from rice husks. The bioavailability of elements depends on speciation (mineralogy). Rice husk biochar is rich in total ash ranging between 36-44 wt% and has a high pH (8.5-9.7) due to the presence of alkaline minerals. A broad XRD peak from 15^o to 35^o 2θ indicates that rice husk biochar samples contains much amorphous silica (Kamath and Proctor, 1998; Tarley et al., 2004) although amorphous carbon also scatters x-rays in this 2θ range. There is no difference in XRD patterns between rice husk biochars produced by the three processes. All rice husk biochar contains the minerals archerite (KH_2PO_4), calcite ($CaCO_3$), chlorocalcite ($KCaCl_3$), kalicinite ($KHCO_3$), pyrocoproite ($K_2MgO_7P_2$), struvite ($KMgPO_4.6H_2O$), sylvite (KCl) and vaterite ($CaCO_3$) all of which contain essential plant nutrients.

Biochar formed from rice husks may sequester carbon in soils while releasing plant nutrients to soil solution as ions diffuse into and out of this highly porous material. The rate at which this process occurs will depend on a numbers of factors including the pore structure of both biochar and soil, the solubility of minerals in biochar and chemical properties including pH of soil and soil solution. This work has clearly demonstrated the value of rice husk biochar as a multinutrient fertilizer.

ACKNOWLEDGMENT

This work was supported by a Crawford Fund grant to Wanpen Wiriyakitnateekul. Our sincere thanks go also to the Centre of Microanalysis and Microscopy the University of Western Australia for SEM analyses. We are grateful for the assistance to Mr. Michael Smirk and Miss Kimberly Duffecy, School of Earth and Environment, the University of Western Australia, with ICP-OES analysis. Many thanks to Winat Sudsukh, Sirapassorn Kiatpuengpon, Nilwan Praikhachorndech and Saowaluk Suraroachanakul who are research students at Kasetsart University for the preparation of biochar samples.

REFERENCES

Chen, Y., Zhu, Y., Wang, Z., Li, Y., Wang, L., Ding, L., Gao, X., Ma, Y., and Guo, Y. Application studies of activated carbon derived from rice husks produced by chemical-thermal process-a review. Advances in Colloid and Interface Science 163 (2011): 39-52.

Day, D., Evans, R.J., Lee, J.W., and Reicosky, D. Economical CO_2, SO_x, and NO_x capture from fossil-fuel utilization with combined renewable hydrogen production and large-scale carbon sequestration. Energy 30 (2005): 2558-2579.

Kalderis, D., Bethanis, S., Paraskeva, P., and Diamadopoulos, E. 'Production of activated carbon from bagasse and rice husks by a single-stage chemical activation method at low retention times'. Bioresource Technology 99 (2008): 6809-6816.

Kamath, S.R., and Proctor, A. Silica gel from rice hull ash: Preparation and characterisation. Cereal Chem. 75 (1998): 484-487.

Liou, T.H. Preparation and characterization of nano-structured silica from rice husk. Materials Science and Engineering A364 (2004): 313-323.

OAE. Agricultural statistics of Thailand 2003. Center for Agricultural Information, Office of Agricultural Economics, Ministry of Agriculture and Co-operatives, Thailand, 2003.

Okimori, Y., Ogawa, M., and Takahashi, F. Potential of CO_2 emission reductions by carbonizing biomass waste from industrial tree plantations in south Sumatra, Indonesia. Mitigat. Adaptat. Strateg. Global Change 8 (2003): 261-280.

Radhika, T., and Sugunan, S. Structural and catalytic investigation of vanadia supported on ceria promoted with high surface area rice husk silica. Journal of Molecular Catalysis A: Chemical 250 (2006): 169-176.

Sohi, S.P., Krull, E., Lopez-Capel, E., and Bol R. A review of biochar and its use and function in soil. In Sparks D.L. ed., Advances in Agronomy, Vol. 105, 47-82 pp. Burlington: Academic Press, 2010.

Tarley, C.R.T., and Arruda, M.A.Z. Biosorption of heavy metals using rice milling by-products, Characterisation and application for removal of metals from aqueous effluents. Chemosphere 54 (2004): 987-995.

Weast, R.C. CRC Handbook of Chemistry and Physics. CRC Press, INC, Boca Raton, Florida, 1983.

Xu, W., Lo, T.Y., and Memon, S.A. Microstructure and reactivity of rich husk ash. Construction and Building Materials 29 (2012): 541-547.

Nattaporn Prakongkep has a B.Sc and Ph.D. from Kasetsart University, Thailand. She carried out this work when she was a research fellow in the School of Earth and Environment at the University of Western Australia.

Robert (Bob) Gilkes has a B.Sc. and Ph.D. from Southhampton University, UK. He is an Emeritus Professor at the University of Western Australia.

Wanpen Wiriyakitnateekul has a B.Sc. from Prince of Songkla University, and M.Sc. and Ph.D. from Kasetsart University, Thailand. She works at the Land Development Department, Thailand.

Apinya Duangchan has B.Sc. and M.Sc., Chulalongkorn University, Thailand and M.Sc., University of Alberta, Canada and Ph.D., University of British Columbia, Canada. She works in the Department of Chemical Engineering, Faculty of Engineering, Kasetsart University.

Timtong Darunsontaya has a B.Sc and Ph.D. from Kasetsart University, Thailand. She is a lecturer at Department of Soil Science, Faculty of Agriculture, Kasetsart University.

Hydrothermal Synthesis of W-Doped Titania Nanofibers and Its Photocatalytic Activity

[1]Low Jing Xiang, *[2]Teressa Nathan-Walleser

Faculty of Engineering, Multimedia University
Jalan Multimedia, Cyberjaya 63000 Malaysia

[1] jx_low@yahoo.com; [2]*teressanathan@hotmail.com

Abstract

Titania nanofibers were synthesized using hydrothermal technique by dispersing P25 powder (20% Rutile and 80% Anatase of TiO_2) in NaOH solution and annealed at 150 °C. The nanofibers that were in ten-hundred nanometer lengths with the diameter of ~ 10 nm were doped with Tungsten Oxide (WO_3) using a simple and efficient impregnating-calcination method. The doping effect of Tungsten (W) on TiO_2 was investigated by means of XRD, UV-Vis and gas chromatograph, while SEM and Nitrogen adsorption were carried out to investigate the morphology and the Brunauer-Emmett-Teller (BET) surface area respectively. The result showed that W doping has enhanced the visible light photocatalytic activity of TiO_2 nanofibers as it has induced shift in the absorption light range with the narrowing of the bandgap energy. The photocatalytic activity of the W-doped anatase TiO_2 has greatly enhanced the transportation of charge transfer and reduced the electron-hole recombination. It showed more than 60 times higher photocatalytic activity than TiO_2 nanofiber and pristine Degussa P25. The amount of W-doping played a crucial role in affecting the photocatalytic activity of TiO_2 where W-doping of more than 5% can reduce the photocatalytic efficacy under visible light range.

Keywords

Metal Oxides; Nanostructures; Band-structure; Photocatalytic

Introduction

Photocatalyst water splitting hydrogen production has been receiving great attention for its high potential as a source of energy, which can be obtained from solar irradiation and water. With Gibbs energy of 237.7 kJmol^{-1}, photocatalyst water splitting is quite a challenging process as it yields thermodynamically unfavorable reaction (Fujishima, 1972; Kudo, 2033; Khan, 2008). However, semiconductor photocatalyst materials overcame this shortfall by band structure tuning, whereby the efficiency of water splitting is determined by the band structure of the material and the electron transfer process. A photogenerated electron is produced in the conduction band along with photogenerated holes in the valence band when the semiconductor photocatalyst material is subjected to irradiation of light energy source (Kaneko, 2002) and this affects the recombination rate. Therefore, band structure tuning has become imperative for the design of semiconductors with these properties.

Years since the discovery of photo-induced water splitting process on TiO_2 electrode by Fujishima and Honda (1972) , TiO_2 has been proven as the most suitable, cost effective and environmental friendly photocatalyst materials for widespread hydrogen production with chemical inertness, non-toxicity, photostability and high oxidizing power properties (Fujishima, 1972; Fujishima, 2000). However, the application of TiO_2 in photocatalysis field is limited by its wide bandgap energy, 3.2 eV and 3.0 eV for Anatase TiO_2 and Rutile TiO_2 respectively, where UV irradiation is needed to activate its photocatalytic properties (Fujishima, 2008). As a result, only 3-5% of the solar beam that reaches the earth can be utilized, which is inefficient. In the past, research efforts have been focused on decreasing the threshold energy for excitation during TiO_2-assisted photocatalysis to maximize the utilization of a wider fraction of solar irradiation for energy conversion as TiO_2 has a relatively large bandgap.

The photocatalytic activity of photocatalyst materials can be improved by several methods such as coupling TiO_2 with other metal oxides, doping, sensitization and supporting (Hashimoto, 2005; Colon, 2006; Kanade, 2007; Arai, 2008). Doping metal ion on the surface of the material has been reported to suppress the electron-hole recombination rate on the photocatalyst materials surface (Colon, 2006; Kanade, 2007; Arai, 2008). The photocatalytic activity was also found to increase with the surface area, which resulted from the doping (Jung, 1999; Dholam, 2009). Transition metal ion has been proven to provide additional energy levels within the bandgap of semiconductor as the metal ion doping creates a transition band on the photocatalyst materials. This may significantly improve the light absorption range of the photocatalyst materials (Zhou, 2005; Zhou, 2006).

Tungsten (W) is amongst the metal ion that has high potential as a dopant on the photocatalyst materials as it is non-toxic and low in cost (Shen, 2005; Couselo, 2008). Its smaller bandgap energy of 2.8 eV has been reported to improve the electron-hole recombination rate, because it controls the availability of photoexcited sites on the catalyst surface. It was also found to improve the charge separation which resulted from the coupling of the two materials (Putta, 2011). $W^{(6+)}$ in WO_3 acts as a trapping site by accepting photoexcited electrons from TiO_2 valence band and reduces to $W^{(5+)}$. In the present work, W-doping has been used to shift the absorption edge of anatase TiO_2 to the visible region and modify its electronic structure by substituting oxygen in the lattice, with tungsten. W-doped TiO_2 nanofibers were synthesized by a simple single step impregnating-calcination method using Titania nanofiber as precursors. The sample was subjected to physical characterization such as XRD, SEM, nitrogen adsorption and UV-Vis characterization to confirm the structural properties and then evaluated for its photocatalytic hydrogen production in methanol aqueous solution by visible light irradiation.

Experimental

Preparation of TiO_2 Nanofiber

TiO_2 nanofiber was prepared by hydrothermal method using Degussa P25 (composed of 80% Anatase and 20% Rutile) as a starting material. 0.75 g of P25 was added into 70 ml of 10 M NaOH solution and stirred for 20 minutes. Solution was then heated up at 150°C in a 100 ml Teflon-lined autoclave for 48 h to ensure the complete combustion of NaOH and the formation of highly crystalline nanofibers. The resulted precipitation was separated by filtration and washed with 0.1 M HCl solution and distilled water. Sample was then dried at 80°C.

Preparation of W-doped TiO_2 Nanofiber

Impregnation method was used to prepare W-doped TiO_2 nanofiber by mixing 0.2 g of TiO_2 with sodium tungsten dehydrate solution at various loading level such as 1, 2.5, 5 and 10 wt%. Nitrate acid solution was used to adjust the pH value of the solutions to 5 followed by 0.5 h of continuous stirring. Solutions were then left at room temperature for 48 h before being dried it in the oven at 100 °C for 5 h to evaporate the water. Dried samples were then calcined at 550 °C for 1.5 h in a muffle furnace.

Physical Characterization of Titania Nanofiber

X-ray diffraction patterns were obtained using the D/MAX-RB X-Ray diffractometer (Rigaku, Japan) with Cu $K\alpha$ radiation at a scan rate of 2θ of 0.05 $^{o}s^{-1}$. The accelerating voltage and applied current were at 40 kV and 80 mA, respectively. The absorption and reflectance spectra of sample were recorded using a UV-Vis spectrophotometer (UV-2550, Shidmadzu, Japan). The Brunauer-Emmett-teller (BET) surface area of the sample materials was measured using ASAP 2020 nitrogen adsorption apparatus (Micromeritics Instruments, USA). All samples were subjected to a degassing process at 180°C prior to the nitrogen absorption measurements. The adsorption data in the relative pressure (P/P_0) ranging from 0.05-0.3 were obtained to determine the BET surface area by multi-point BET method. Barret-Joyner-Halender (BJH) method was carried out to determine the pore size distribution of sample materials, assuming that they are all cylindrical pores. Pore volume and average pore size were determined by nitrogen adsorption volume at the relative pressure (P/P_0). Microstructural observation was done using the S-4800 field emission scanning electron microscope (FESEM, Hitachi,Japan).

Photocatalytic Activity Measurements

50 mg of the sample was dissolved in 80 ml of 25% methanol and 75% DI water solution. A 100 ml closely sealed Pyrex flask was used as a reactor at atmospheric pressure and room temperature. The mixture was then poured into the flask and bubbled with nitrogen for 40 minutes to remove dissolved oxygen and ensure that the reaction is under anaerobic conditions. The Pyrex flask with the sample solution was then irradiated by a 350 W Xe arc lamp with 400 nm range with cutoff filter for 1 h. Subsequently, 40 ml of gas was intermittently sampled through septum and analyzed with a gas chromatograph (GC-14C, Shidmadzu, Japan) with nitrogen as the carrier gas.

Results and Discussion

SEM Observation

Fig. 1 (a) and Fig. 1 (b) show the SEM image of undoped TiO_2 nanofiber and W-doped TiO_2 nanofiber, respectively, where monodispersed fibers can be observed whose length ranges from tens to hundreds nanometer, and the diameters were about 10nm. The formation of the nanofibers was initialized by breaking down the Ti-O-Ti building blocks of the P25 with the aid of NaOH. It was further exfoliated into smaller flakes in the direction of [0 1 0] plane as it was subjected to high pressure and temperature during the hydrothermal process. Both sides of the P25 flakes brimmed with unsaturated dangling bonds which resulted from the high surface activity of P25 flakes. The saturation of these dangling bonds led to different surface energy, hence, further rolling the sheets into fibers (Kasuga, 1998). The adhesion of the layer was determined by the weak van der Waal's forces which caused the hydrophilic head of P25 to bond strongly to the adjacent water molecules (Kasuga, 1998). Fig. 1 (b) shows that when 5% W is doped into TiO_2 nanofiber, the TiO_2 nanofibers tend to agglomerate some sub-particles which are also in the order of nanometer. This may be attributed to the calcination process which has improved the surface activity of sample.

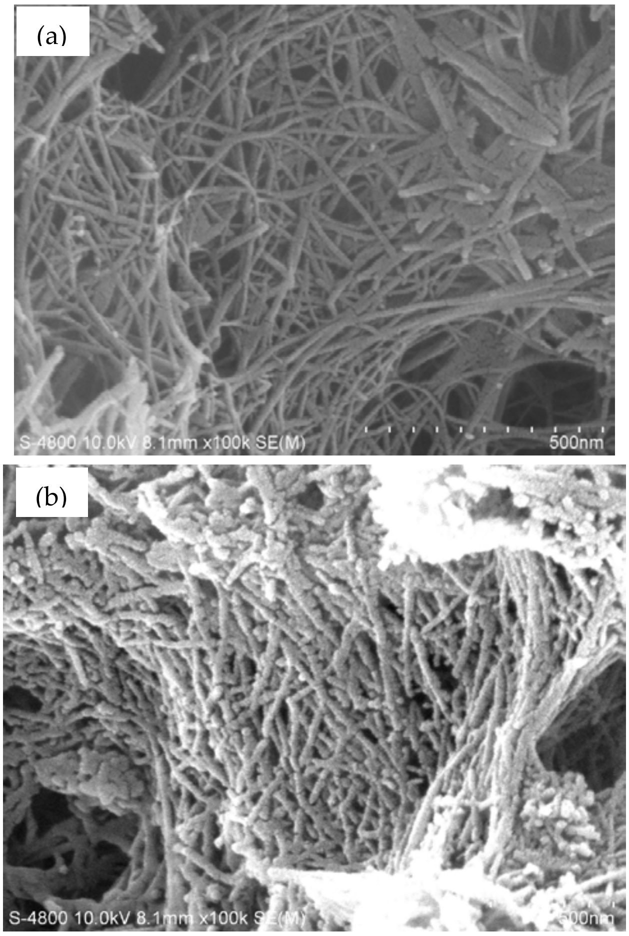

FIG.1. SEM IMAGES OF (a) TIO_2 NANOFIBERS (b) W-DOPED TIO_2 NANOFIBERS

XRD Analysis

Fig. 2a shows the comparison of the XRD pattern of pristine P25, P25 nanofiber and 5 wt% W-doped P25 nanofibers. The result of the diffraction peaks obtained confirms the formation of TiO_2 anatase phase [JCPDS No. 21-1272, space group: I41/amd (1 4 1)]. As shown in Fig. 2a, there are two anatase phase in the pristine P25 with diffraction peak at 25.4° and 48° for (1 0 1) phase and (2 0 0) phase, respectively. The intensity of anatase peaks decreased and the width of XRD diffraction peaks of anatase became wider as it went from pristine to doped TiO_2 nanofiber. The degree of crystallinity decreased as the sample was subjected to further calcination. W peaks were not significant in all the samples. This could be attributed to the low wt% of W and the fact that some of the Ti^{4+} that are on the lattice of TiO_2 nanofiber could be substituted with the $W^{n+}(4<n<6)$, which has similar ion radius (Saepurahman, 2010; Habazaki, 1998). This was clearly elucidated in Fig. 2b where a slight shift towards lower 2θ at the (101) diffraction peak position can be observed as it went from pristine to W doped TiO_2 nanofiber at various concentrations. The peaks have shifted more towards lower 2θ and peak broadening was observed as the concentration increased from 1% wt to 10% wt. As explained earlier, the ionic radius of W^{n+} (4<n<6) (41 pm) smaller than Ti^{4+}(53 pm) (Yang, 2005) is indicative of a decrease in the crystal size.

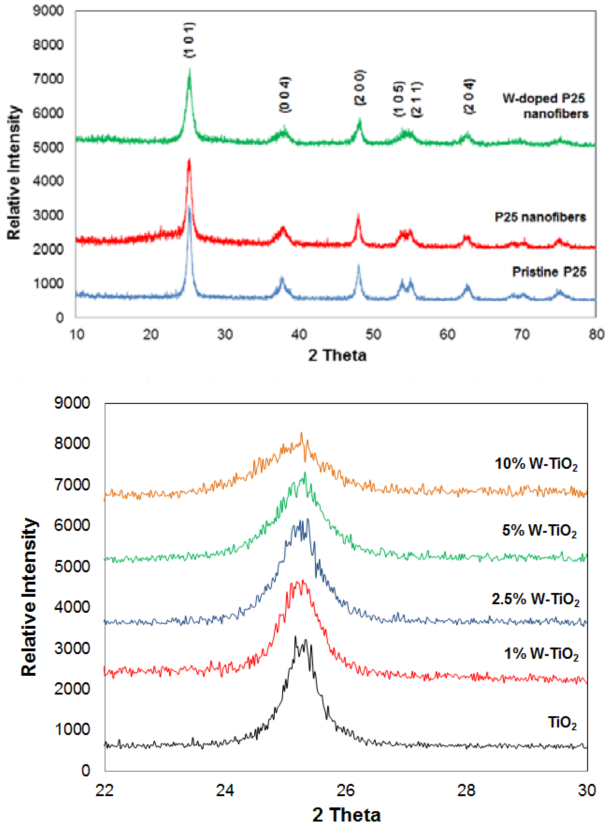

FIG. 2(a) XRD PATTERN OF P25, TIO_2 NANOFIBER AND 5 WT% W-DOPED TIO2 NANOFIBER (b) A ZOOM OF THE (101) DIFFRACTION PEAKS OF TIO_2 NANOFIBER, 1 WT%, 2.5 WT% ,5 WT% AND 10 WT%; W-DOPED TIO_2 NANOFIBER

However, as reported by Yang et.al (2005), a shift in lower 2θ angle generally indicates a lattice volume expansion, which is contrary to the decrease of crystal size. In the present work, no increase of crystal size was observed, thus confirming that the lower angle shift is indicative of mild lattice strain that arises from the possible repulsion between W^{6+} cations, which may occur as interstitial dopants in the bulk of the material. The XRD results here corroborate with the reported work (Yang, 2005).

BET Surface Area and Pore Structure Analysis

Fig. 3 shows the nitrogen adsorption-desorption isotherms and corresponding pore size distribution curves of the W-doped TiO_2 nanofiber. The presence of mesopores (2-50 nm) on the sample was observed with the hysteresis loops of type H3 at relative pressure (P/P_o) of range 0.8-1.0. The presence of macropores (>50 nm) on the samples were also seen with the approaching of hysteresis loops to relative pressure of 1.0.

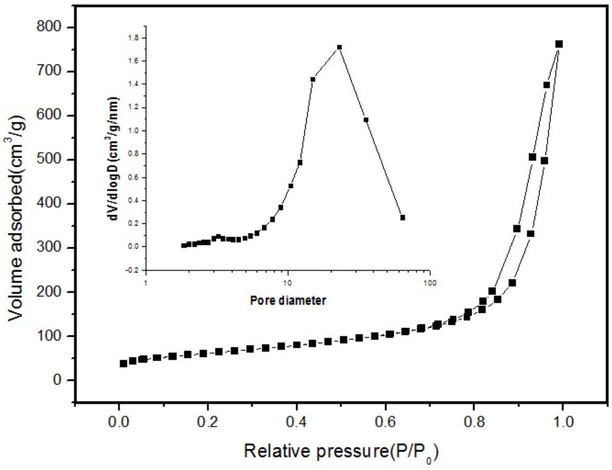

FIG. 3 NITROGEN ABSORPTION TO THE RELATIVE PRESSURE TEST OF W-DOPED TiO_2

TABLE 1 BET SURFACE AREA, PORE VOLUME AND PORE SIZE DISTRIBUTION OF THE W-DOPED TITANIA AT VARIOUS W DOPING CONCENTRATIONS

Samples	Surface area (m^2/g)	pore volume (cm^3/g)	Average Pore Size (nm)
TiO_2	112.4	0.99	35.3
1% W-TiO_2	128.7	1	31.1
2.5%W-TiO_2	157.4	1.14	29
5% W-TiO_2	197.2	1.25	25.4
10% W-TiO_2	220.3	1.18	21.4

Table 1 shows the BET test result of different W doping concentrations obtained from the nitrogen adsorption-desorption isotherm data. BET surface area (S_{BET}) of the W-doped Titania nanofiber increased with the increasing wt% of W. Higher specific surface was attributed to the W-doping which inhibited the growth of TiO_2 nanofiber. The smaller the crystallite sizes of materials were, the higher the specific surface area was. As shown in the Table 1, the pore size distribution of the W-doped Titania nanofiber has also increased as the W doping concentration increased.

Light Absorption Characteristics

Fig. 4 shows the UV-Vis spectra of the photocatalyst samples. The absorption threshold of pristine P25 occurred at ~400 nm and an abrupt increase in absorption before 400 nm can be observed because of the intrinsic band gap energy of TiO_2 (3.2 eV). As the absorption spectra were extended, a red shift can be seen for the W-doped Titania nanofiber as the wt% of W increases; the higher the wt% of W in the composite was, the larger the absorption threshold of the samples was. This was influenced by the doping of W into the Titania nanofiber, which was attributed to the charge transfer transition on Titania nanofiber conduction band (Chen and Mao, 2007). The sample doped with 5% of W and 10% of W showed similar absorption on in the 500-800 nm regions of visible light but the latter showed a higher absorption on the region of ultraviolet region. This is because of the crystal distortion that increases as doping concentration increases. When more W6+partly substitutes Ti^{4+} in the TiO_2 lattice, and the absorption edge of TiO_2 red shifts to a longer wavelength. Although, higher degree of crystal distortion could induce more carriers to be generated under visible light irradiation (Chen and Mao, 2007), which will increase the photocatalytic efficiency but sample doped with 5% of W was found to show higher photocatalytic activity than 10% of W. The drop in photocatalytic efficacy as the doping concentration exceeds 5% is attributed to the increase in the recombination centres produced by W for the photogenerated carriers.

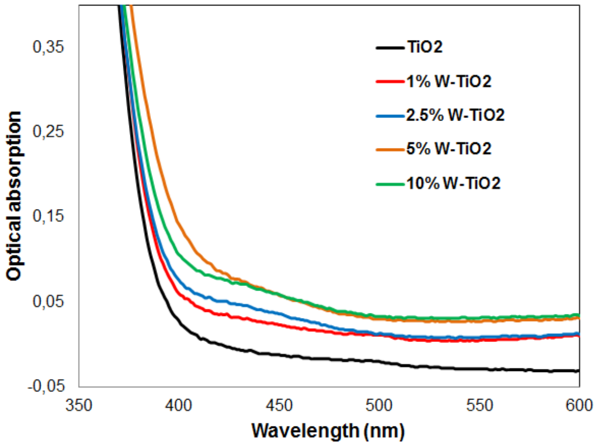

FIG. 4 UV-VIS SPECTRA OF THE W-DOPED TiO_2 NANOFIBER WITH DIFFERENT WT% OF W

Photocatalytic Activity

The hydrogen production rate of W-doped Titania nanofiber in 20% methanol aqueous solution has been reported as an effective hole scavenger to prevent electron hole recombination. In Fig. 5, the hydrogen production rate shows an increasing pattern, as the wt% of W increases from 1% (209.08 μmolH_2h^{-1}) to 5% (790.63 μmolH_2h^{-1}). As the loading of W goes beyond 5%, the hydrogen production of sample materials started decreasing. The excess loading of WO_3 creating recombination site of photocatalysis process has reduced the hydrogen production. The photocatalytic activity of sample was evident from the W-doping as it created means of transfer of photogenerated electrons from TiO_2 to W. The enhancement of absorption intensity in visible light range has induced more photogenerated electrons and holes, giving rise to the photocatalytic activity.

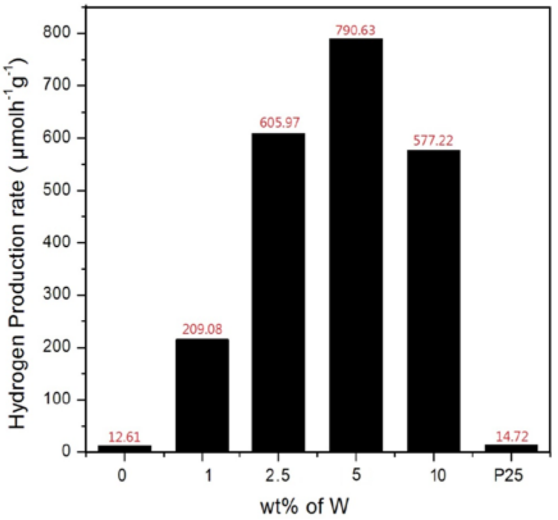

FIG. 5 PHOTOCATALYTIC HYDROGEN PRODUCTION RESULT OF THE W-DOPED TIO_2 NANOFIBER WITH DIFFERENT WT% OF W

Conclusions

A light driven strategy was demonstrated with the preparation of W-doped TiO_2 nanofiber. W-doping into TiO_2 nanofiber has influenced the change of crystallinity, specific surface areas and pore structures. The photocatalytic activities of the samples were greatly enhanced by yielding 60 times higher hydrogen production with the increase of W-doping into TiO_2 nanofiber at an optimal doping level of W, i.e. at 5 wt%. The doping has induced a shift in the absorption light range with the narrowing of the bandgap energy. The increase in the photocatalytic activity of the W-doped TiO_2 has indicated the improvement of the transportation of charge transfer on the Titania nanofiber conduction band and reduced the electron-hole recombination rate. However, the further increase of W-doping into TiO_2 nanofiber has led to reduction of photocatalytic activity.

ACKNOWLEDGMENT

We gratefully acknowledge the support from State key laboratory of advanced technology for Materials synthesis and processing (SKLWUT), Wuhan University of Technology (WHUT) for SEM, XRD, and Gas-chromatograph analysis.

REFERENCES

Arai T., Senda S., Sato Y., Takahashi H., Shinoda K., Jeyadevan B. and Tohji K., Cu-Doped ZnS Hollow Particle with High Activity for Hydrogen Generation from Alkaline Sulfide Solution under Visible Light Chem. Mater., 20 (2008): 1997-2000.

Chen X., and Mao S. S., Titanium dioxide nanomaterials: synthesis, properties, modifications, and applications, Chem. Rev., 107 (2007): 2891–2959.

Colon G., Maicu M., Hidalgo M., Navio J. , Cu-doped TiO systems with improved photocatalytic activity, Appl Catal. B-Environ, 67 (2006): 41-51.

Couselo N., Garcia Einschlag F. , Candal R., Jobbagy M. , Tungsten-Doped TiO_2 vs Pure TiO_2 Photocatalysts: Effects on Photobleaching Kinetics and Mechanism J. Phys. Chem. C, 112 (2008): 1094-1100.

Dholam R., Patel N., Adami M., Miotello A. , Hydrogen production by photocatalytic water-splitting using Cr- or Fe-doped TiO_2 composite thin films photocatalyst, Int. J. of Hydrog. Energy, 34 (2009): 5337-5346.

Fujishima A. and Honda K. , Photocatalyst materials for water splitting, Nature, 238 (1972): 37-38.

Fujishima A., Rao T. N., and Tryk D. A., Titanium dioxide photocatalysis, J Photochem Photobiol C Photochem Rev, 1 (2000)

Fujishima A., Zhang X., Tryk D. A. , TiO_2 photocatalysis and related surface phenomena, Surface Science Reports, 63 (2008): 515-582.

Habazaki H., Takahiro K., Yamaguchi S., Shimizu K., Skeldon P., Thompson G.E., Wood G. C. , Influence of tungsten species on the structure of anodic titania , Philosophical Magazine A, 78 (1998): 171-188.

Hashimoto K.,. Irie H and Fujishima A., TiO_2 Photocatalysis:

A Historical Overview and Future Prospects Jpn. J. Appl. Phys., 44, 12 (2005):8269–8285.

Jung K. Y. and Park S. B. , Enhanced photoactivity of silica-embedded titania particles prepared bysol–gel process for the decomposition of trichloroethylene Appl Catal. B-Environ, 25 (1999): 249-256.

Kanade K.G., Kale B.B., Baeg J. O, Lee S. M., Lee C. W., Moon S. J., Chang H. , Self-assembled aligned Cu doped ZnO nanoparticles for photocatalytic hydrogen production under visible light irradiation, Materials Chemistry and Physics, 102 (2007): 98-104.

Kaneko M. and Okura I. ,Photocatalysis: science and technology: Springer-Verlag (2002).

Kasuga T., Hiramatsu M., Hoson A., Sekino T., and Niihara K., Formation of Titanium Oxide Nanotube Langmuir, 14 (1998): 3160-3163.

Khan M. A., Woo S. I., Yang O.B, Hydrothermally stabilized Fe(III) doped titania active under visible light for water splitting reaction Int. J. of Hydrog. Energy, 33 (2008): 5345-5351.

Kudo A. , Photocatalyst Materials for Water Splitting, Catalysis Surveys from Asia, 7 (2003): 31-38.

Lorret O., Francova D., Waldner G., Stelzer N. , W-doped titania nanoparticles for UV and visible-light photocatalytic reactions, Appl Catal. B-Environ:91 (2009): 39-46.

Marci G., Palmisano L., Sclafani, Venezia A.M. , Campostrini R., Carturan G., Martin C., Rives V. , Solana G., Influence of tungsten oxide on structural and surface properties of sol–gel prepared TiO_2 employed for 4-nitrophenol photodegradation , J Chem Soc Faraday Trans 92 (1996): 819–82.

Putta T., Lu M. C., Anotai J. , Photocatalytic activity of tungsten-doped TiO_2 with hydrothermal treatment under blue light irradiation, J. of Environ Management ,92 (2011): 2272 -2276.

Saepurahman, Abdullah M. A., Chong F. K., Preparation and characterization of tungsten-loaded titanium dioxide photocatalyst for enhanced dye degradation J. Hazard M., 176 (2010): 451-458.

Shen Y., Xiong T., Li T., Yang K. , Tungsten and nitrogen co-doped TiO_2 nano-powders with strong visible light response, Appl Catal. B-Environ, 83 (2005): 177-185.

Wu W., Hu X., Xie T., Li G., Zhang L., Phase Structure of W-Doped Nano-TiO_2 Produced by Sol-Gel Method, China Particuology 3 (2005): 233-236.

Yang H. M., Shi R. R., Zhang K., Hu Y. H., Tang A. D. and Li X.W. , Synthesis of WO_3/TiO_2 nanocomposites via sol–gel method Alloy Compd 398 (2005): 200–202.

Zhou M., Yu J., Cheng B., Yu H. , Preparation and photocatalytic activity of Fe-doped mesoporous titanium dioxide nanocrystalline photocatalysts, Materials Chemistry and Physics, 93 (2005): 159-163.

Zhou M., Yu J., Cheng B. , Effects of Fe-doping on the photocatalytic activity of mesoporous TiO_2 powders prepared by an ultrasonic method, J. Hazard M., 137 (2006): 1838-1847.

The Electron Range and the Backscattering Coefficients in Compound Semiconductors: Comment on Z.Rouabah, A. Bouzid, C. Champion, N. Bouarissa [Sol.Stat.Comm. 151 (2011) 838]

A. Bentabet*[1], N. Fenineche[2], A.Betka[3], A.Azbouche[4], Y. Bouhadda[5]

[1]Laboratoire de Caractérisation et Valorisation des Ressources Naturelles (LCVRN), université de Bordj Bou-Arreridj, 34000, Algeria

[2]IRTES-LERMPS/FR FC LAB, UTBM University, Belfort, France

[3]Départements de physique, faculté des sciences, université de Bejaia, 6000, Algérie

[4]Nuclear Research Center of Algiers, 2 Boulevard Frantz Fanon Alger, Algeria

[5]Unit of Applied Research in Renewable Energy, 47000 Ghardaïa, Algeria

*[1]a.bentabet@gmail.com; [2]nour-eddine.fenineche@utbm.fr; [3]betrahim@yahoo.fr; [4]a_azbouche@yahoo.fr; [5]bouhadda@yahoo.com

Abstract

This work is a comment on the paper of Z.Rouabah et al [Sol.Stat.Comm. 151 (2011) 838]. Indeed, it is shown that the transport cross-section used in their work is inaccurate and really not based on Jablonski model [Phys. Rev. B 58 (1998) 16470] as well. Moreover, it is noted that their calculation method concerning the compound materials is not explained also not justified. Moreover, some recommendations have been indicated on the use of a given model (developed initially for a monatomic solid target) to study the compound material which is not respected in the case of the above mentioned paper. In addition, it is showen that all their results concerning GaN, GaAs and InSb semiconductor materials must be reviewed.

Keywords

Semiconductors; Low-energy Electron; Electron Backscattering; Electron Range; Monte Carlo Simulation

Introduction

Electron material interaction is tied much importance to many domains of analytical techniques such as electron probe microanalysis, Auger electron spectroscopy, scanning electron microscopy (SEM) etc (Bentabet[a] et al. 2013, Bentabet et al. 2010). Two transport quantities play a great role in the majority of such mentioned studies: the backscattering coefficient (BSC) and the range of penetration (R). For example, the BSC is a major factor to validate the model used in the simulation and to inform about the absorbed rate of incident particles (Bentabet 2011). Indeed, by this work, some comments are presented, about a paper of (Rouabah et al. 2011) studying the electron transport in GaN, GaAs and InSb semi conductor targets using analytical models. These materials are base of a number of electronic devices, as the authors of (Rouabah et al. 2011) said “The choice of target materials is based on their importance for many applications in semiconductor technology... As for GaAs, it is the most technologically important material for device applications. Concerning GaN, interest on this material has grown since it has successful applications in blue lasers and light emitting diodes. It has also applications in high-frequency optoelectronics and at high temperatures”. Besides, the indium antimonide (InSb) is a semiconductor consisting of III-V compounds of antimony and indium. It has a narrow gap used particularly as infrared detector, in thermal imaging, in infrared homing guidance systems and infrared astronomy. Detectors, based on indium antimonide, are sensitive to wavelengths between 1 and 5 μm. So, for such reasons, the authors (Rouabah et al. 2011) took these materials as targets for electron beam to carry out their study.

In this paper, our work is divided into two parts: the first one represents generalities on two great axes: the first of which shows the electronic properties of the above mentioned materials near or in the thermodynamic equilibrium, while the second shows the electron beam transport in these materials (i.e. the incidental electron is outside the thermodynamic equilibrium with the target). However, the second part represents our commentary on the work of (Rouabah et al. 2011) which is part of the second axis.

The Electronic Interaction in GaN, GaAs and InSb Semi Conductors

The Electronic Properties of GaN, GaAs and InSb

GaN, GaAs and InSb semi conductors have been studied using the first-principle total-energy calculations based on the density functional theory using the pseudopotential method, and a plane-wave expansion of the wave functions as implemented in the ABINIT code.

The exchange and correlation energy is treated using the local density approximation (LDA) with the Ceperley–Alder form (1980) as parameterized by Perdew and Zunger (1981). The interaction of the valence electrons with the ionic cores is represented by separable, norm-conserving Troullier–Martins pseudo-potentials (1991).

The pseudo-potentials were generated using Hartwigsen -Goedecker-Hutter scheme (www.abinit.org). A basis of plane waves up to a kinetic energy of 80 Hartree was used. Reciprocal space integration was performed by k-points sampling with sets of special points of 8×8×8 obtained using the standard special k point technique of the Monkhorst and Pack (1976).

The zinc-blende GaX (X=N and As) and InSb have a cubic symmetry belonging to the F-43M (space group N°216). The Ga (or In) atom is located at 4a (0, 0, 0) site and the X (or Sb) atom is located at 4c (1/4, 1/4, 1/4) site (Bouhadda et al. 2012) . The calculated equilibrium lattice constant for zinc-blend GaN, GaAs and InSb from LDA, compared to the experimental data are presented in Table 1. Our calculated lattice parameters seem very close to the experimental one (Madelung 1982, Lie et al. 1992, Straumanis et al. 1965).

TABLE 1 THE CALCULATED AND EXPERIMENTAL LATTICE PARAMETERS (IN Å) OF THE ZINC-BLENDE GAN, GAAS AND INSB.

	GaN	GaAs	InSb
This work	4.335	5.531	6.35
Exp.	4.50 [a]	5.650[b]	6.479[c]

[a] Madelung 1982. [b] Lie et al. 1992. [c] Straumanis et al. 1965

Elsewhere, the importance of GaN, GaAs and InSb materials could be validated by their electronic properties.

The figures (1-3) represent the band structure of the above compound materials respectively. Indeed, it is remarked that all these materials have a direct band gap. Consequently, the transition from the valence band to the conduction one could be done by energy absorption phenomena without the phonon contribution. Moreover, the semi conductor group compounds (GaN, GaAs and InSb) shows three typical gaps (large, medium and tight) respectively. Each category of these later plays an important role in the technology application.

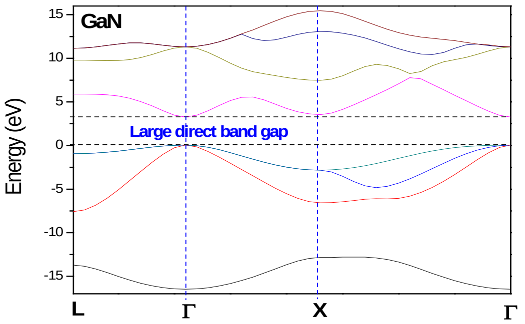

FIG. 1 BAND STRUCTURES OF GaN.

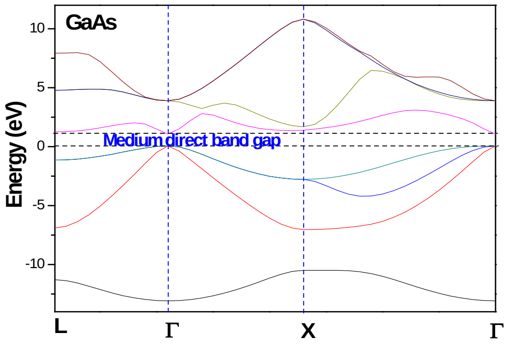

FIG. 2 BAND STRUCTURES OF GaAs.

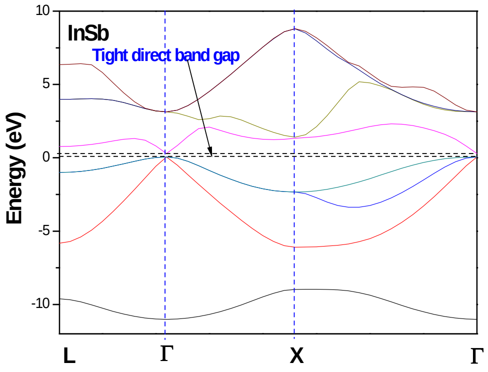

FIG. 3 BAND STRUCTURES OF InSb.

The Electron Beam Transport in GaN, GaAs and InSb Targets

Generally the solid targets are presented in the form of thick or thin films attacked by slow electrons. In other words, it is supposed that the target is taken as a parallelepiped with infinite length and width and thickness (half entire space). The coordinates of the particles are located using a (OXYZ) reference so that axis (OX) and (OY) belong to the exterior surface outside of the target (entry surface) and (OZ) is directed toward the interior of the solid (Bentabet et al. 2009). The angles θ and φ represent the polar and the azimuthal angles which can be varied as follow: 0≤ θ≤π and 0≤φ≤2π (Bentabet 2012) (see figure 4). A number of methods could be used to follow the electron trajectory in the solid target since its entry in the target to its final stage which is defined as either the backscattering or the absorption phenomena. In the figure (2) we present a Monte Carlo scheme used by number of authors.

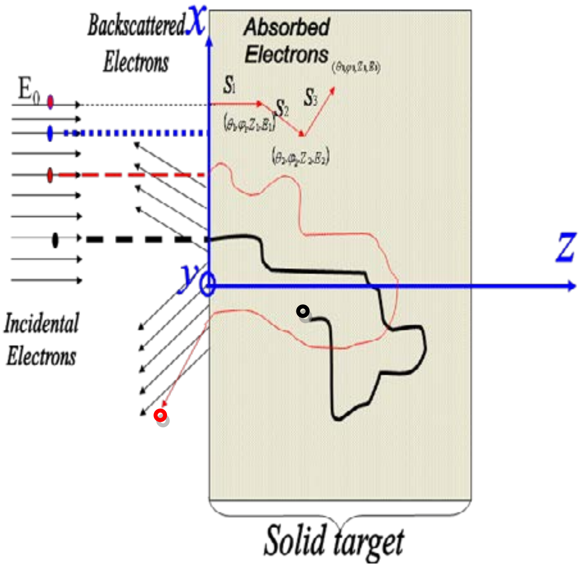

FIG. 4 THE SLOW ELECTRON TRANSPORT SCHEME IN THE INTERIOR OF THE SOLID TARGET. SI: THE DISTANCE BETWEEN TWO SUCCESSIVE COLLISIONS (I INDICATES THE COLLISION NUMBER, i=1, 2,). Zi: THE NORMAL DISTANCE BETWEEN THE ENTRY SURFACE AND THE ELECTRON. θI AND φI ARE THE AZIMUTAL AND SCATTERING ANGLES. EI THE ELECTRON ENERGY AFTER COLLISION. THE RED TRAJECTORY IS OF THE BACKSCATTERED ELECTRON. THE BLACK TRAJECTORY IS OF THE ABSORBED ELECTRON.

Both the two phenomena could be defined as follows:

- An electron is absorbed if its energy is lost during the different inelastic processes with the solid target, from its initial energy until it arrives at the thermal equilibrium with the medium (the bold black trajectory in figure (4)). In the absorption phenomena, number of quantities could describe the absorption of the electron; among them the range of penetration which is defined as the path length travelled by a particle (in an infinite medium) before being absorbed (Salvat et al. 2003). In other words, R is the average track length of absorbed particles (Penelope nomination).
- An electron considered as backscattered if, after interaction with the solid target, this electron leaves the solid by the entry surface (the red trajectory in figure (4)). Under these conditions, the backscattered electrons are those which have energy higher than the thermal energy rather higher than the surface energy and its coordinate (Z) is lower than zero. Several quantities could describe this category of transport phenomena, in particular, the backscattering coefficient (BSC). BSC is the backscattering probability which is the ratio of the backscattered particles to the incidental ones.

Comments on the Paper of Rouabah et al. (2011)

According to Rouabah et al. (2011), they calculated the backscattering coefficient (BSC) using the Vicanek and Urbassek (1991) formula. Hence, they used four models to calculate the range and one model to calculate the transport cross-section (TCS) as well. Moreover, they think that their results concerning some semi-conductors seems to be seen as the first predictions for low-energy electron BSC.

Carefully analyzing (Rouabah et al. 2011) paper, an anomalous problem is noted and consequently the results must be reviewed and corrected.

The Jablonski Transport Cross Section

Rouabah et al (2011) attributed an old TCS to Jablonski (1998) and they said in their abstract (Rouabah et al. 2011) in the next paragraph: "*The cross-sections used to describe the electron transport are determined via the appropriate analytical expression given by Jablonski (1998) whose new improved version has been recently reported by Rouabah et al (2009)*". Unfortunately, this information is inaccurate. Actually, their work "Rouabah et al. 2011" is based on the TCS obtained by integrating a screened cross-section. Knowing that this latter is obtained by applying the first order Born approximation on a screened potential (Jablonski 1998, Bentabet[a] et al. 2013).

So, the TCS obtained by integrating the screened cross section is given by (Bentabet[a] et al. 2013):

$$\sigma_{Tr}^{B} = \frac{32\pi Z^{2/3} C_F^4 a_0^2}{\left(\mu^{\infty}\right)^4} \frac{1}{\varepsilon_0^2} \left[\ln\left(1+\varepsilon_0\right) - \frac{\varepsilon_0}{1+\varepsilon_0} \right] \qquad (1)$$

With,

$C_F=0.8853414$, $\varepsilon_0 = 0.230440\dfrac{E}{\left(\mu^\infty\right)^2 Z^{2/3}}$, $\mu^\infty = 1.22$.

where σ_{Tr}^{B}, Z and E are the transport cross-section, the atomic number of the atom target and the electron energy, respectively.

We note that we have shown step by step in our recent paper (Bentabet[a] et al. 2013) that the age of σ_{Tr}^{B} is more than 60 years old (since the works of *Wentzel (*1927*) and* Nigam (1959)). Moreover, it is worth noting that the first order Born approximation fails at lower energies (Jablonski 1998, Bentabet[a] et al. 2013), and the σ_{Tr}^{B} standard deviation reaches hundreds percent for number of elements compared to that obtained by quantum methods. For example the σ_{Tr}^{B} deviation reaches ~1500% for Au at E = 250 eV (which is the proof that Jablonski cannot propose such model with such unacceptable deviation) whereas the authors of (Rouabah et al. 2009, Rouabah et al 2011) attributed eq. (1) to Jablonski.

Actually, the TCS proposed by Jablonski lies in his paper (Jablonski 1998): "To *obtain a more accurate analytical expression for* σ_{Tr} *, we need an additional analytical function* $G(\varepsilon_0)$ *correcting* σ_{Tr}^{B}

$$\sigma_{Tr} = \sigma_{Tr}^{B} G(\varepsilon_0) \tag{2}$$

With

$$G(\varepsilon_0) = \varepsilon_0 \exp\left\{\sum_{i=1}^{4} A_i \left[\ln(10\varepsilon_0)^{i/2}\right]\right\} \tag{3}$$

where A_0, A_1, A_2, A_3, and A_4 are fitted constants for each element." Therefore the Jablonski transport cross section is that given by (2-3) which correspond to Eqs. (21) and (22) of (Jablonski 1998).

Consequently, the next two paragraphs of (Rouabah et al 2011) must be reviewed:

- In their abstract: "*The cross-sections used to describe the electron transport are determined via the appropriate analytical expression given by Jablonski [A. Jablonski, Phys. Rev. B 58(1998) 16470] whose new improved version has been recently reported by Rouabah et al. [Z. Rouabah,N. Bouarissa, C. Champion, N. Bouaouadja, Appl. Surf. Sci. 255 (2009) 6217].*"
- In their section 3.:"*The electron transport cross-sections have been calculated by using the new improved expression suggested by Rouabah et al. of the approximate analytical one previously derived by Jablonski.*"

Comment on the Accuracy of the Used Transport Cross Section in Rouabah et al. 2011

Rouabah et al (2011) used the TCS proposed by (Rouabah et al. 2009). However, before quoting our overview points, we recall that Rouabah et al (2009) used the same transport cross section expressed by equation (1) where the only difference is that μ^∞ has been taken as a free parameter. Thus, to determine μ^∞, σ_{Tr}^{B} has been ajusted to Mayol et al TCS (1997). After a fitting process, they suggested the next interpolation form of μ^∞ given by:

$$\mu^\infty = 2.17\times10^{-7}Z^3-1.54\times10^{-4}Z^2+0.03Z+0.89 \tag{4}$$

It is noted that we have shown step by step in our recent paper (Bentabet[a] et al. 2013) that Rouabah et al (2009) TCS fit is not accurate (the deviations were as examples: for Au: 96% and 30.3 % at E=250 and 500 eV respectively, for Al: 21% and 12 % at E=250 and 500 eV… respectively, for Cu: 41%, 20% and 10.2 % at E=250, 500 and 1000 eV respectively, ….).

Calculation Method of Rouabah et al. (2011)

There's a great ambiguity regarding the calculation method of (Rouabah et al. 2011). For example, no one can take again their calculation without knowing in detail the TCS and the ranges used in their work. For example, no explanation has been given about how they calculated the range of Kanaya and Okayama (1972) and the BSC of GaN, GaAs and InSb. This ambiguity is another **inaccuracy** of Rouabah et al (2011) work.

For more details;

The range of Kanaya and Okayama is given by:

$$R_{K-O} = \frac{2.76\times10^{-11} A E_b^{5/3}}{Z^{8/9}\rho}\frac{\left(1+0.978\times10^{-6}E_b\right)^{5/3}}{\left(1+1.957\times10^{-6}E_b\right)^{4/3}} \tag{6}$$

Where $R_{K\text{-}O}$, A, E_b, ρ are Knaya and Okayama range, the atomic weight, the electron incidence energy and the density of the target. In terms of question: how did they calculate the atomic weight and the atomic number of GaN, GaAs and InSb?

The Vicanek and Urbassek BSC model: We recall that Rouabah et al. (2011) used Vicanek and Urbassek (1991) model which showed that BSC (denoted η in the following) has been calculated analytically at normal angles of incidence by:

$$\eta = \left(1 + a_1\frac{1}{\nu^{\frac{1}{2}}} + a_2\frac{1}{\nu} + a_3\frac{1}{\nu^{\frac{3}{2}}} + a_4\frac{1}{\nu^2}\right)^{-1/2} \tag{7}$$

with: $a_1 = \dfrac{6}{\sqrt{\pi}}$, $a_2 = \dfrac{27}{\pi}$, $a_3 = \dfrac{27}{\sqrt{\pi}}\left(\dfrac{4}{\pi}-1\right)$, $a_4 = \left(\dfrac{3}{2}-\sqrt{2}\right)^{-2}$.

In expression (7), ν is the mean number of wide angle collisions defined as,

$$\nu = NR\sigma_{tr} \tag{8}$$

With R and σ_{tr} are the range and the transport cross-section and N is the number of atoms per unit of volume in the solid target given by:

$$N = \frac{N_{Av}\rho}{A} \tag{9}$$

with N_{Av} is Avogadro number.

Indeed, to calculate η they have needed to know "v". By consequence they have needed to calculate σ_{tr} and A of GaN, GaAs and InSb. Unfortunately, Rouabah et al (2011) have not given any information about the calculation of these quantities!

Is Rouabah et al (2011) Exptession *"The results May be Seen as the First Predictions …"* True?

When said it is reported in the ABSTRACT of Rouabah et al (2011) the next paragraph that "The results may be seen as the first predictions …" they should be very careful because when someone reading this later will believe, certainly, that the authors of such paragraph will show a new method or a new idea somewhere. However, the authors of (Rouabah et al. 2011) have not explained any method concerning the passage from monatomic materials to compound ones (see above). In addition, Rouabah et al. (2011) did not present any comparison with the experience or with the Monte Carlo simulation concerning the compound materials. Before giving our viewpoint concerning this latter, we recall that number of Monte Carlo codes have been developed to study simple and complex systems (medicals, nuclear, materials, etc.). Among "the simplest systems" is that studied by (Rouabah et al. 2011) (the simplest geometry of the incidental particles source and the simplest geometry of the target).

For example, Penelope (Salvat et al. 2003) is an accurate Monte Carlo code developed since about twenty years.

In Penelope manual (version 2008) we found in page 3 the next expression:

---- MATERIAL DATA FILE ----

PENELOPE reads the required information about each material .. … To simulate geometrical structures with several materials, .. PENELOPE labels the M-th material in this file with the index MAT=M... The maximum number of different materials that PENELOPE can handle simultaneously is fixed by the parameter MAXMAT, which in the present version is set **equal to 10**."

Thus, the use of Penelope code straightforwardly allows the calculation of the backscattering coefficient and the range of GaN, GaAs and InSb with reasonable results.

We think that this claim "the results may be seen as the first time"is quite similar to the following example:

One would like to calculate for example $(1.0201030406)^{1/3}$. May be, no person has calculated this equation previously. So, anyone could claim "the result $(1.0201030406)^{1/3}$= 1.00665660482660198750765839 may be seen as the first time". But, is this claim a scientific fact? Of course no, because, really, anyone who masters the use of the calculator, could calculate this latter " $(1.0201030406)^{1/3}$ "without any difficulties.

Following the same argument. So, when anyone who masters the use of Penelope code, could calculate the BSC and the range of GaN, GaAs, InSb and any binary compound material in short time and without any difficulties. In addition, the important question is: are the BSCs of (Rouabah et al. 2011) true (see below)?

Thus, on the basis that (Rouabah et al. 2011) have not explained their calculation method despite the fact of the possibility to use accurate Monte Carlo codes, the use of such paragraph of Rouabah et al (2011) "*The results may be seen as the first predictions ….*" is inaccurate.

The Large Deviation of Rouabah et al (2011) Results

It is noted that Rouabah et al. (2011) have repeated an important part (i.e. using the same procedures) of the work of Kurniawan and Ong (2007). In other words, Kurniawan and Ong used three models to calculate the range: Gruen et al (1957) (R_G), Everhart and Hoff (1971) (R_{E-H}) and Kanaya and Okayama (1972) (R_{K-O}). Moreover, Kurniawan and Ong tried to carry out a correction on these ranges by proposing an improvement range (R_{Ku-O}). However, Rouabah et al. (2011) repeated the same above models to calculate the BSC but without showing any improvement somewhere.

For more details; it is recalled that Kurniawan and Ong used R_{K-O} given by (6) and R_G and R_{E-H} which are given by:

$$R_G = \frac{45.7}{\rho} E_b^{1.75} \tag{10}$$

$$R_{E-H} = \frac{40.}{\rho} E_b^{1.75} \tag{11}$$

It is noted that R_{K-O} can be written as follows:

$$R_{K-O} \approx \frac{2.76\times10^{-11} A}{Z^{8/9}\rho} E_b^{5/3} \qquad (12)$$

Because $\left(1+0.978\times10^{-6}E_b\right)^{5/3}\times\left(1+1.957\times10^{-6}E_b\right)^{-4/3}$ is a relativistic correction.

Based on the fact that some of the above ranges are semi-empirical models (developed, with a limit validity, on the basis of experimental results) then Kurniawan and Ong proposed an improvement expression given by $R_{Ku-O}=\alpha E_b^{\beta}$, where α and β are free parameters determined by using the best fit of the ranges obtained by using Monte Carlo code. Hence, they found:

$$R_{Ku-O}=23.17E_b^{1.73} \quad \text{for Si} \qquad (13)$$

$$R_{Ku-O}=10.46E_b^{1.68} \quad \text{for GaN} \qquad (14)$$

Consequently, Kurniawan and Ong have suggested an improvement range expression for Si and GaN by by means of Monte Carlo method.

Elsewhere, Rouabah et al (2011) said the next paragraph: "*the proposed range-energy expressions based on the extrapolated range for Si and GaN provided by Kurniawan and Ong at low beam energies.*" Unfortunately, this information is inaccurate. The results presented by Rouabah et al (2011) do not correspond to R_{KuO} expressions (given by (13-14)). As results, such information needs to be corrected.

To validate the results of Rouabah et al (2011) concerning the compound materials that have been reviewed, it is thought that a similar reasoning of (Kurniawan et al. 2007) can be followed. In other words, their work can be evaluated by carrying out a comparison between the results of Rouabah et al (2011) and those of Penelope code which is an accurate Monte Carlo code (the additively rule and the mean excitation energy have been validated experimentally for compound materials (Barô et al. 1993). Figures (5), (6) and (7) represent the BSCs of Rouabah et al (2011) compared to that of Penelope code. It can be observed is that the deviation between the BSC of GaN (Rouabah et al. 2011) and that of Penelope code is very larger than that in the case of GaAs and InSb (as example the deviation of their BSC by using R_{K-O} is about 55%, 19% and 21% for GaN, GaAs and InSb respectively). This latter allows us to claim that the authors of (Rouabah et al. 2011) have not used the same procedure in the calculation of BSC. Moreover, it is remarked that there is a large deviation between their results and those of Penelope code in all compound materials cases which is the proof of the invalidity of their work, otherwise Penelope is, (as example, too, the deviation of their BSC by using R_{E-H} is about 75%, 50% and 44% for GaN, GaAs and InSb respectively).

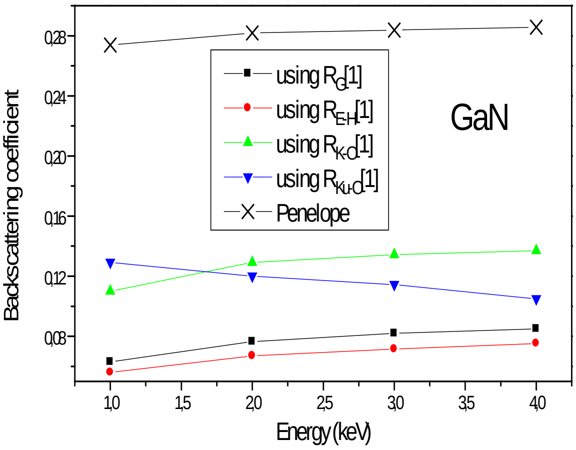

FIG. 5 ELECTRON BACKSCATTERING COEFFICIENT VERSUS ELECTRON PRIMARY ENERGY IN GAN. [1] ROUABAH ET AL.(2011).

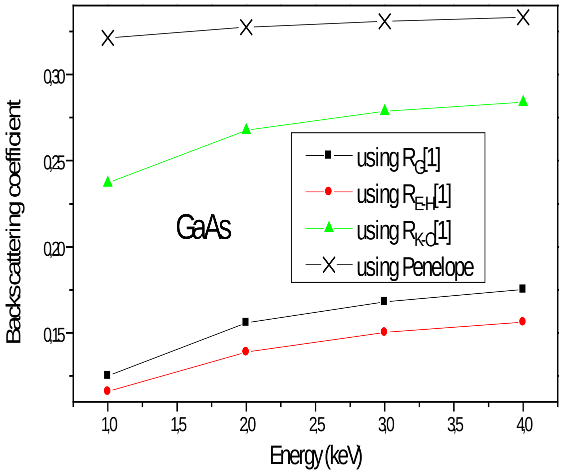

FIG. 6 ELECTRON BACKSCATTERING COEFFICIENT VERSUS ELECTRON PRIMARY ENERGY IN GAAS. [1]: ROUABAH ET AL.(2011).

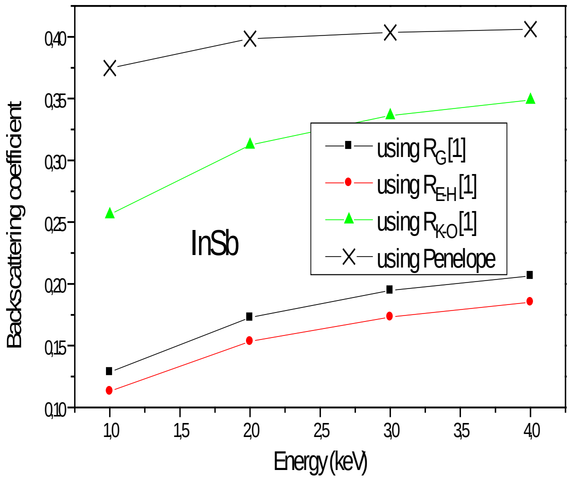

FIG. 7 ELECTRON BACKSCATTERING COEFFICIENT VERSUS ELECTRON PRIMARY ENERGY IN INSB. [1]: ROUABAH ET AL.(2011).

Remark: it is noted that we have tried after a nimber of tests (due, unfortunately, to the ambiguity in their calculation) to discover the procedures applied by (Rouabah et al. 2011) to calculate the range and the BSC of compound materials; where it is thought that:

- ✓ Concerning the Kanay and Okayama range: via the reading of Kurniawan and Ong paper (Kurniawan et al. 2007)., it is indicated that the authors of (Rouabah et al. 2011) used the next procedure to calculate $R_{K\text{-}O}$:

  $$A_{AB} = (A_A + A_B)/2 \qquad (15)$$

  $$Z_{AB} = (Z_A + Z_B)/2 \qquad (16)$$

  Where A_{AB} and Z_{AB} are the atomic weight and the atomic number of a material up from two elements A and B. For example the atomic number of Z_{GaN}=(31+7)/2=19. Indeed, we have a reservation about this procedure. It is noted that eqs.(15-16) have been proposed, first, by (Kurniawan et al. 2007). However, the authors (Rouabah et al. 2011) have not cited this latter. This one (i.e. the no citation of the used method especially if they used equations (15-16) proposed first by (Kurniawan et al. 2007)) is another inaccuracy of the work (Rouabah et al. 2011). Secondly, (Kurniawan et al. 2007) adopted equations (15-16) as an intermediate steps (before improvement). Actually, it is totally not a justifiable processing to pass from monatomic materials to compound ones by using the equations (15-16). Moreover, when $R_{K\text{-}O}$ given by using equations (6, 15-16) is approximately good for GaN (which has been remarked by (Kurniawan et al. 2007)), it is not recommended to generalize this rule on all $R_{K\text{-}O}$ ranges of compound materials because eqs.(15-16) it is a false procedure (except after an agreed $R_{K\text{-}O}$ study for number of compound materials).
- ✓ Concerning their BSC results, too, it is reported that the authors (Rouabah et al. 2011) have used the next procedures:

  For GaN: $\sigma_{tr(GaN)} = \left(\sigma_{tr(Ga)} + \sigma_{tr(N)}\right)/2$,

  $$A_{GaN} = A_{Ga} + A_N = 83.73g \qquad (17)$$

  For GaAs: $\sigma_{tr(GaAs)} = \left(\sigma_{tr(Ga)} + \sigma_{tr(As)}\right)/2$,

  $$A_{GaAs} = \left(A_{Ga} + A_{As}\right)/2 = 72.32g \qquad (18)$$

  For InSb: $\sigma_{tr(InSb)} = \left(\sigma_{tr(In)} + \sigma_{tr(Sb)}\right)/2$,

  $$A_{InSb} = \left(A_{In} + A_{Sb}\right)/2 = 118.285g \qquad (19)$$

  Equations (17-19) showed that the atomic weight of GaN have been not calculated by using the same procedure such as on GaAs and InSb.

So, whether the authors of (Rouabah et al. 2011) used these procedures or not, we note that the use of these procedures given approximately the same results presented by (Rouabah et al. 2011).

Conclusion

In summary, it has been shown that Rouabah et al (2011) have applied the Vicanek and Urbassek formula to calculate the backscattering coefficient (BSC) of electrons impinging in GaN, GaAs and InS but without any explanation concerning their method calculation. In addition, it has been also noted that they have used inaccurate transport cross-section model and their BSC results of compound materials have a large deviation with those of Penelope code, as well. Consequently, on the basis that Penelope is an accurate Monte Carlo code, this latter (large deviation results) is the proof that their work is invalid and should be reviewed.

REFERENCES

Bentabet, A., Betka, A., Azbouche, A., Fenineche, N., Bouhadda, Y. “Study on Electron/Positron Scattering in Solid Targets Using Accurate Transport Cross-sections: Comment on Z. Rouabah et al Papers.”, American Journal of Condensed Matter Physics, 3(3)(2013):31-40.

Bentabet, A., Azbouche, A., Betka, A., Bouhadda, Y. , Fenineche, N. ““Improved Expression for Calculating Electron Transport Crosses Sections”: Comment on Z. Rouabah Et Al[Phys. Lett. A 373 (2009) 282].”, American Journal of Condensed Matter Physics, 3(4)(2013):104-110.

Bentabet, A. “The range of penetration and the backscattering coefficient by using both the analytic and the stochastic theoretical ways of electron slowing down in solid targets: Comparative study.” Nucl. Instrum. Meth. Phys. Res. B 269 (2011): 774-777.

Bentabet, A., Fenineche, N., Loucif, K.,” A comparative study between slow electrons and positrons transport in solid thin films.” Applied Surface Science 255 (2009):7580–7585.

Bentabet, A. “Spherical geometric model for absorption electrons/positrons phenomenon: Application to the mean penetration depth calculation Vacuum 86 (2012): 1855-1859.

Bouhadda, Y., Bentabet, A., Fenineche, N. E., Boudouma, Y. "The ab initio calculation of the dynamical and the thermodynamic properties of the zinc-blende GaX (X=N, P, As and Sb)", International Journal of Computational Materials Science and Engineering 1250026 (2012): 1-16.

Baró, J., Sempau, J., Fernández-Varea, J.M., Salvat F., "PENELOPE: An algorithm for Monte Carlo simulation of the penetration and energy loss of electrons and positrons in matter", Nucl. Instr. Method. B, 73 (1993): 447-473.

Ceperley, D. M. and Alder, B. J. "Ground state of the electron Gas by a stochastic method." Phys. Rev. Lett. 45(1980): 566–569.

Everhart, T.E. and Hoff, P.H. "Determination of Kilovolt Electron Energy Dissipation vs Penetration Distance in Solid Materials", J. Appl. Phys. 42 (1971): 5837-5836.

Gruen, A.E., Z. Nat. Forsch. A 12 (1957) 89.

Jablonski, A. "Transport cross section for electrons at energies of surface-sensitive spectroscopies." Phys. Rev. B 58 (1998) 16470.

Kurniawan, O., Ong V.K.S. "Investigation of Range-energy Relationships for Low-energy Electron Beams in Silicon and Gallium Nitride", Scanning 29 (2007) 280-286.

Kanaya, K., Okayama, S., "Penetration and energy-loss theory of electrons in solid targets", J. Phys. D 5 (1972): 43-58.

Lei, T., Moustakas, T. D., Graham, R. J., He, Y. and Berkowitz, S. J. "Epitaxial growth and characterization of zinc-blend gallium nitride on (001) silicon," J. Appl.Phys. 71(1992): 4933–4943.

Madelung, O. (Ed.) "Semiconductors: Physics of Group IV Elements and III–V Compounds," Landolt-B¨ornstein, New Series, Group III, Vol. 17, Part. A (1982), Springer-Verlag, Berlin.

Mayol, R., Salvat, F., 1997, At.Data Nucl. Data Tables, Total and transport cross sections for elastic scattering of electrons by atoms, 65, 55-154.

Monkhorst, H. J. and Pack, J. D. "Special points for Brillouin-zone integrations,"Phys. Rev. B 13(1976): 5188–5192.

Nigam, B. P., Sundaresan, M. K., Wu, T.-Y. "Theory of Multiple Scattering: Second Born Approximation and Corrections to Molière's Work", Phys. Rev. 115 (1959): 491-502..

Perdew, J. P. and Zunger Alex, "Self-interaction correction to density-functional approximations for many-electron systems." Phys. Rev. B 23(1981) 5048–5079.

Rouabah, Z. , Bouarissa, N. , Champion, C., Bouaouadja, N. "Study on electron scattering in solid targets using accurate transport cross-sections.", Appl. Surf. Sci. 255 (2009): 6217-6220.

Rouabah, Z., Bouzid, A., Champion, C., Bouarissa, N. "Electron range-energy relationships for calculating backscattering coefficients in elemental and compound semiconductors" Solid State Communications 151 (2011):838-841.

Straumanis, M. E. and Kim, C. D., "Lattice Parameters, Thermal Expansion Coefficients, Phase Width, and Perfection of the Structure of GaSb and InSb." J. Appl. Phys. 36(1965):3822-3825.

Salvat, F., Fernandez-Varea, J.M., Acosta, E., Simpau, J., PENELOPE–A Code system for Monte Carlo Simulation of Electron and Photon Transport, Nuclear Energy Agency OECD/NEA, Issy-les-Moulineaux, France, 2003. <http://www.nea.fr>.

Troullier, N. and Martins, J. L. "Efficient pseudopotentials for plane-wave calculations. II. Operators for fast iterative diagonalization," Phys. Rev. B 43(1991): 8861–8869.

Vicanek, M., Urbassek, H.M. "Reflexion coefficient of light ions", Phys. Rev. B 44 (1991): 7234-7242.

www.abinit.org

Wentzel, G., 1927, Z. Phys., 40, 590.

Assessment of Thermal Performance of Green Building Materials Produced with Plant Oils

Figen Balo[1], H. Lütfi Yucel[2]

[1]Department of Industrial Engineering, Firat University, 23279 Elazığ, Turkey

[2]Department of Mechanical Engineering, Firat University, 23279 Elazığ, Turkey

[1] figenbalo@gmail.com, [2] hlyucel@gmail.com

Abstract

The purpose of this study was to investigate the potential utilisation of vegetable oils in fly ash and clay, as binding, to develop construction materials that could be used for walls.

In present work, fly ash, natural clay and four different kinds of epoxidized vegetable oils (epoxidized soybean oil, epoxidized sunflower oil, epoxidized olive oil and epoxidized palm oil) were used to produce 180 kinds of composite materials and by analyzing the thermal conductivity coefficients of these novel materials, their use as a construction material was investigated.

The lowest value of thermal conductivity, 0.25 W/mK, was measured for the sample with a 70% fly ash /30% clay ratio and 50% epoxidized sunflower oil processed at 200^{0}C; while the highest value of thermal conductivity, 0.496 W/mK, was measured for the sample with a 30% fly ash /70% clay ratio and 40% epoxidized soybean oil processed at 160^{0}C. The lowest values of thermal conductivity for the samples with epoxidized olive oil and epoxidized palm oil processed at 200^{o}C were obtained 0.255 and 0.258 W/mK, respectively. The lowest value of thermal conductivity was obtained from the highest process temperature at use of the epoxidized vegetable oils. Density and thermal conductivity decreased with the increase of epoxidized vegetable oils and FA at all levels of replacements. Moreover, with increasing of process, temperatures decreased density and thermal conductivity. The results showed that thermal conductivity of the building material increased when the high clay ratio was used in the preparation of the material composition. Results have also indicated an interesting potential for the fly ash recycling and epoxidized vegetable oils renewable to produce useful materials.

Keywords

Construction Material; Epoxidized Vegetable Oils; Mechanical Properties; Fly Ash; Thermal Conductivity

Introduction

Recently, the use of renewable sources in the preparation of various industrial materials has been revitalized because of the environmental concerns. Many researchers have invested the modification of traditional materials to make them more user-friendly, and into designing novel biocomposites out of naturally occurring materials. The belief is that biocomposite materials will reduce the need for petrol-based production (thus reducing pollution) at a low cost, thereby producing a positive effect both environmentally and economically. Natural oils are considered to be the most important class of renewable sources. They can be obtained from naturally occurring plants, such as sunflower, cotton, linseed (Güner et al.). Natural oils are tri-glyceride esters of fatty acids, the general structure of which is shown in Fig.1 (Khot et al.).

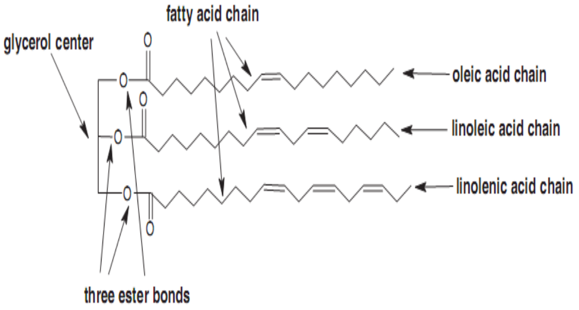

FIG. 1 THE TRIGLYCERIDE CHAIN CONTAINING THREE FATTY ACID BY A GLYCEROL CENTER

TABLE 1 FATTY ACID COMPOSITION OF ZO, PO, SFO AND SO

Fatty Acid	Formula	Structure	[C:DB]*	ZO (%)	PO (%)	SFO (%)	SO (%)
Palmitic	$C_{16}H_{32}O_2$	$CH_3(CH_2)_{14}COOH$	16:0	13.7	39	6	11.0
Stearic	$C_{18}H_{36}O_2$	$CH_3(CH_2)CH_{16}COOH$	18:0	2.5	2	4	4.0
Oleic	$C_{18}H_{34}O_2$	$CH_3(CH_2)CH_7$-$CH=CH(CH_2)_7$-$COOH$	18:1	71.1	56	4	23.4
Linoleic	$C_{18}H_{32}O_2$	$CH_3(CH_2)_4CH=CH$-CH_2-$CH=CH(CH_2)_7$-$COOH$	18:2	10	9	47	53.2
Linolenic	$C_{18}H_{30}O_2$	$CH_3.CH_2.CH=CH$-CH_2-$CH=CH$-CH_2-$CH=CH(CH_2)_7$-$COOH$	18:3	0.6	2	1	7.8

* (C, the number of carbon atoms; DB, the number of double bonds)

Triglycerides comprise three fatty acids joined by a glycerol center. Most of the common oil contains fatty acids that vary from 14 to 22 carbons in length, with 1–3 double bonds. The fatty acid distribution of vegetable oils is shown in Table 1 (Güner et al. and Sharma et al.). In addition, there are some oils containing fatty acids with other types of functionalities (e.g.epoxies, hydroxyls, cyclic groups and furanoid groups) (Gunstone).

It is apparent that on a molecular level, these oils are composed of many different types of triglyceride, with numerous levels of unsaturation. In addition to their application in the food industry, triglyceride oils have been used for the production of coatings (Bussell), inks (Cunningham et al), plasticizers (Hodakowski et al.), lubricants (Salunkhe et al.) and agro-chemicals (Trecker et al and Force et al). In general, drying oils (these can polymerize in air to form a tough elastic film) are the most widely used oils in these industries, although the semi-drying oils (these partially harden when exposed to air) also find use in some applications. The polymers obtained from natural oils are biopolymers in the sense that they are generated from renewable natural sources; and often biodegradable as well as non-toxic. Plant oils containing epoxy groups are important oleochemicals. The major application for these oils is their use as a PVC-plasticizers and stabilisers, because of their ability to catch free HCl and thus slowing degradation. In addition epoxidized vegetable oils (EVO) can be used as reactive diluents for paints and as intermediates for polyurethane-polyol production (Eierdanz).

Recently, bio-based thermosetting polymers from vegetable oils such as epoxidized soybean oil (ESO), epoxidized palm oil (EPO), epoxidized castor oil, epoxidized linseed oil, and epoxidizeed canola oil have been synthesized in several studies (Park et al and Crivello et al). EVOs possess functional epoxide groups, which can react with suitable curing agents to form an elastomeric network. However, vegetable-oil-based polymeric materials show low mechanical strengths. Several researchers have studied the preparation and mechanical properties of bio-based composite materials derived from soybean oils and glass fibers (Miyagawa et al- Miyagawa et al). Park et al. and Miyagawa and coworkers investigated the thermophysical and mechanical properties of epoxidized-vegetable-oil-modified epoxy materials. Hong and Uyama and coworkers reported the fabrication and characterization of biobased nanocomposites from functionalized vegetable oils and organically modified layered clays (Lu et al. and Hiroshi et al.).

Clay can be chemically modified to make the clay complexes (Polyamide (PA)/clay and, polystyrene (PS)/clay, polymethylmethacrylate (PMMA)/clay, polypropylene (PP)/clay, and polyurethane (PU)/clay nanocompsites) compatible with organic monomers and polymers (Lu et al. and Hiroshi et al.). Clay, an inexpensive natural mineral that has been used as filler for rubber and plastic for many years, is easy availability, low cost and more importantly environmentally friendly.

The use of many waste products as engineering materials is of major concern to engineers due to their applications for different objectives. For this reason, research on the use of waste products will help to solve many environmental problems, and create new useful findings in the field of engineering. Many researchers have worked to evaluate the waste materials to lower the pollutant effects to the natural environment. The quantity of FA produced from thermal power plants in Turkey is approximately 15 million tons each year, and its percentage utilization is less than 5% (Akkaya). FA, a by-product of coal combustion, is frequently used in concrete production as an inexpensive substitute for Portland cement. Its pozzolanic properties improve the strength of the concrete, and its small particles make the mixture easier to knead (Pei-wei et al.). Indeed, there is an extensive bibliography on the use of FA as a component of concrete (Jiménez et al. and Chindaprasirt et al) and the changes that its addition induces in both mechanical (Topçu et al) and thermal (Demirboğa et al.) terms. Balo and coworkers produced composite materials with different EVO-FA–C and analyzed the physical–mechanical and thermal properties of these materials. When the FA and EVO ratio is increased, low compressive-tensile strength, low thermal conductivity, and high abrasion loss are obtained; while when the C ratio is increased, high compressive-tensile strength, high thermal conductivity, and low abrasion loss are obtained. The minimum thermal conductivity of 0.273 W/mK is observed with the samples containing ESO–FA–C. It is increased with the decrease of ESO and FA. The compressive and tensile strengths are varying from 13.53 to 6.31 MPa and 1.287 to 0.879 MPa, respectively. The minimum thermal conductivity of 0.255 W/mK is observed with the samples containing EPO–FA–C. The compressive and tensile strengths are varying from 4.26 to 1.5 MPa and 0.722 to 0.428 MPa, respectively. The best sample properties with the samples containing EZO–FA–C are determinated as follows: thermal conductivity of 0.258 W/mK, compressive strength of 4.37 MPa, tensile strength of 0.731 MPa, abrasion loss of 1.04% and mass of 198.72g. The lowest value of the thermal conductivity, compressive-tensile strength and mass in produces are obtained for sample produced with 50% EVO/70% FA/30%C. The lowest value of the abrasive loss is determinate for sample produced with 40% EVO/30% FA/70% C. The effect of FA, C, perlite and epoxidized linseed oil on the thermal and mechanical properties of construction materials have been investigated by Balo et. al. The compressive and tensile strengths varied from 10.01 to 1.107 MPa and 8.38 to 1.013 MPa, respectively. The minimum thermal conductivity of 0.313 W/mK observed for the sample made with a 60% FA/30% C/10% P ratio and 50% ELO is processed at 200°C. It is increased with the decrease of ELO and FA. Results indicate an interesting potential for the FA recycling and epoxidized linseed oil renewable to produce useful materials (Balo et al).

In present work, FA, C and four different EVO (ESFO, EPO, EZO and ESO) are used to produce of composite materials. The densities and thermal properties of obtained novel construction materials are investigated.

Experimental

Experimental Scope

Fly ash is one of the most plentiful and versatile of the industrial by-products. About 55 million tons of coal and lignite is combusted in Turkey annually, resulting in more than 15 million tons of fly ash.

In recent years, natural oils have attracted much attention as raw materials for the preparation of resins and polymeric materials, to replace or augment the traditional petro-chemical based polymers and resins. Soybean oil, olive oil, sunflower oil and palm oil are some of the cheapest commercially available vegetable oils.

This study is aimed at assessing the feasibility, in technological terms, of FA disposal and EVO in C bodies used in insulation material making.

Materials and Methods

EVOs (EZO, EPO, ESFO, ESO), FA and C were used as the raw materials to produce the construction material samples. ASTM C618 (Class C), FA, from Kahramanmaraş (Afşin-Elbistan Thermal Power Plant) in Turkey was used in this study. The material has a density of 1.5 g/cm³ and a thermal conductivity coefficient of 0.93 W/mK. EVOs and C (whose density is 2.24 g/cm³ and the thermal conductivity coefficient is 0.511W/mK.) were obtained from Konsan Inc. in Adana and Aslan Corporation in Elazığ in Turkey, respectively. The EVOs are cured with different anhydrides in the presence of various catalysts such as tertiary amines or imidazoles. The physical and chemical characteristics of the EVOs used in this study are summarized in Table 2. Figure 2 shows the chemical structures of ZO, EZO, PO, EPO, SFO, ESFO, SO and ESO. The chemical compositions for the FA and C are shown in Table 3.

TABLE 2 PHYSICAL AND CHEMICAL CHARACTERISTICS OF EZO, EPO, ESFO AND ESO

PROPERTIES	EPOXİDİZED VEGETABLE OİLS			
	EZO	EPO	ESFO	ESO
Appearance at normal temperature	*Thick to green liquid*	*Thick to orange liquid*	*Thick to yellow liquid*	*Clear to yellow liquid*
Brilliance	< (Pt-Co) : 412	< (Pt-Co) : 391	< (Pt-Co) : 385	< (Pt-Co): 400
Acid value	(KOH/g) : 1.21mg	(KOH/g) :1.14 mg	(KOH/g) :max 1.5 mg	(KOH/g):max.2 mg
Iodine value	< %0.85	< %0.44	< %1.5 - %1,7	< max. %3
Oxirane value	%4.14	%3.15	%4.5 - %5,2	%6.4
Thermal conductivity coefficient	0,14 W/mK	0,144 W/mK	0,135 W/mK	0,156 W/mK
Density (25 °C)	0.9 – 0.926 g/cm³	0.897 – 0.941 g/cm³	0.925 – 0.973 g/cm³	0.985 - 0.995 g/cm³
Sabonification number	188 - 196 (KOH/g)	173 – 77	162 – 169	183 – 185
Flow point	12°C	4°C	1°C	-1°C
Boiling point	167°C	145°C	138°C	150°C
Ignition point	359°C	304°C	297°C	310°C
Viscosity	276 MPa.s (at 25°C)	239 MPa.s (at 40°)	143 MPa.s (25°C)	325 MPa.s (25°C)
Refractive index (at 25°C)	%1.865	1.398	1.356	1.472
Melting point in water (at25°C)	< %0.035	< %0.011	< %0.01	< %0.01
Loss on heating	< %0.65	< %0.51	< %0.46	< %0.5

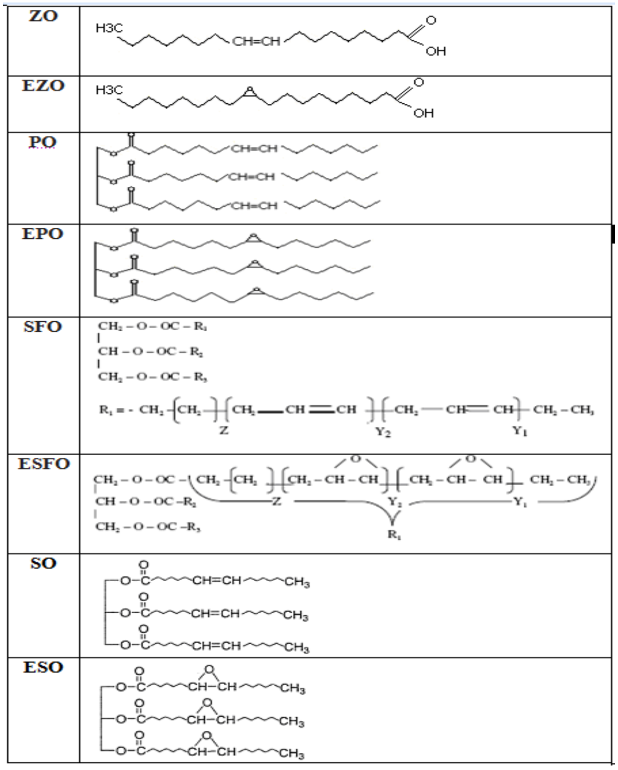

FIG. 2 CHEMICAL STRUCTURES OF EVOs

TABLE 3 RANGE OF CHEMICAL COMPOSITION (WT %) OF FA AND C

	SiO_2	Al_2O_3	Fe_2O_3	CaO	MgO	Ignition loss
Fly Ash	21.33	4.025	2.606	36.480	1.032	29.798
Clay	43.645	20.259	12.954	10.150	1.534	9.650

FA and C were used as the main materials to produce the samples. The EVO was used as binder in samples. The standard temperatures and sample compositions were determined from the pretrial. The percentage ratio of the weights of FA and C were 30, 40, 50, 60 and 70. The different compositions of 100 wt% FA-C volume were maintained throughout the series of sample mixes. 100 wt%: compositions of FA and C were prepared using EVO and mixed in predetermined proportions to adjust the appropriate moulding consistency to desired levels. The levels of EVO were selected to give appropriate moulding consistency values ranging from 40 to 50 to sample mixes when treated with a fixed volume of sample. This volume which imparts proper moulding consistency to a sample mix was predetermined from blank trials. The experimental studies were designed to determine the heating conditions most favourable for the EVO/FA/C samples in relation to the properties of the finished products, and to explore the possibilities of reducing the temperatures below those normally used in the brick industry. When process temperature was lower than 160^{o}C, the sample wasn't completely dry. When process temperature was above 200^{o}C, deformation of sample began; and its structure started to crack, at the same time partial fracture in sample happened. Three main groups of samples of EVO, FA and C were produced (160, 180 and 200^{o}C) and specified as 70%C+ 30%FA, 60%C+ 40%FA, 50%C+ 50%FA, 40%C+ 60%FA and 30%C+ 70%FA. For each group, separately, EZO-FA-C, EPO-FA-C, ESFO-FA-C and ESO-FA-C mixtures were prepared adding 40%, 45%, and 50% EVO in weight to FA+ C. Hence, 180 different mixes were obtained and cast. The full details and numbers of these samples are given in Table 4. The samples were prepared in laboratory with a small type Lancaster PC-Lab counter-current mixer (size: 16"w. x 30"d. x 40"h) for a total of 5 min. Hand compaction was used. Precautions were taken to ensure homogeneity and full compaction (The full homogenity mixture was supplied with counter-current mixture. The compaction of the samples was obtained by means of vibration. Test samples of 150mm x 60mm x 20mm were cast using an internal and external vibrator). The samples are casted into 150 x 60 x 20 mm prism steel moulds at normal consistency (Unfired sample shouldn't be ooze from mould.) for tests. After casting, all the test samples were finished with a steel towel. Firstly, the samples are fired at temperature 100^{o}C for 12 h (Predrying was obtained at this temperature) and then fired at temperatures 160, 180 and 200^{o}C for 10 h in electric furnace, respectively. The fortyfive different results were obtained for the fifteen samples at three different process temperatures (160, 180 and 200^{o}C) from each EVO. The number of total sample was 180. The samples containing EVO, FA and C, after firing are shown in Fig.3.

TABLE 4 THE MİX DESİGN AND NUMBERS FOR SAMPLES.

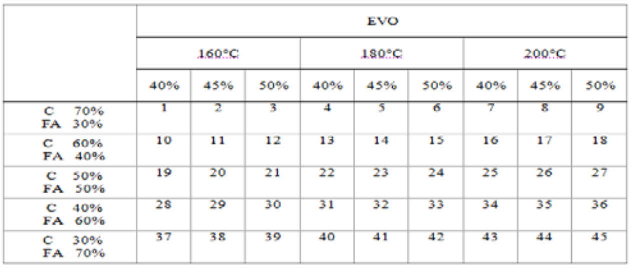

	EVO								
	160°C			180°C			200°C		
	40%	45%	50%	40%	45%	50%	40%	45%	50%
C 70% FA 30%	1	2	3	4	5	6	7	8	9
C 60% FA 40%	10	11	12	13	14	15	16	17	18
C 50% FA 50%	19	20	21	22	23	24	25	26	27
C 40% FA 60%	28	29	30	31	32	33	34	35	36
C 30% FA 70%	37	38	39	40	41	42	43	44	45

FIG. 3 SAMPLES CONTAİNİNG EVO [EZO (50%), EPO (50%), ESFO (50%), ESO (50%)], FA (50%) AND C (50%), AFTER FİRİNG

The tests were performed in the Fırat University Engineering, Construction Department Laboratories. The density was evaluated for each sample and raw materials using test procedures described in the TS 699 (1987) standard. The results were appraised using equations from TS 699.

FIG. 4 PİCTURE OF THE SHOTHERM-QTM TEMPERATURE MEASUREMENT GAUGE

A Shotherm Quick Thermal Conductivity Meter (QTM) based on DIN 51046 Hot Wire Method was used (ASTM C 1113-90). Shotherm-QTM device is the production of Kyoto Electronics Manufacturing, Japan (Fig. 4) with measurement range 0.02–10 W/mK; measurement precision is 5% of reading value per reference plate, and measuring time to be the standard 100–120 s; in which, the hot wire (Cr-Ni) and the thermoelement (Ni Cr-Ni) soldered in the middle, is placed between the two samples. One of the samples is known thermal conductivity coefficient while the other is the sample to be investigated. Here, the thermal conductivity coefficient is determined by Eq.(1) (Denko et al.):

$$k = K\frac{l^2 \ln(t_2/t_1)}{V_2 - V_1} - H \qquad (1)$$

Where K and H are the constants of Shoterm QTM Aparatus and they are taken as 252.10^{-4} and 33.10^{-3}, respectively. Every measurement is repeated three times on three different localities for each sample. The thermal conductivity coefficient (k) is computed by using the average of these nine k values.

This method has wide applications (Willshee et al. and Daire et al) in determining thermal conductivity of refractory materials where, instead of measuring heat flow, the temperature variation with time at certain locations is measured. Being transient in nature, this method takes only a few minutes in contrast to the earlier methods involving steady-state conditions.

Results and Discussions

The results obtained in the tests are shown in Figs. 5–9. They are evaluated and discussed below.

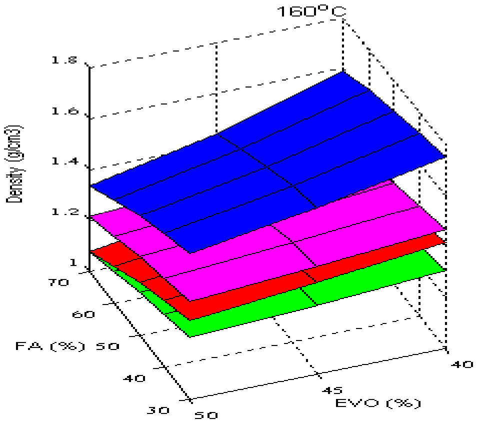

(a) 160 ^{0}C

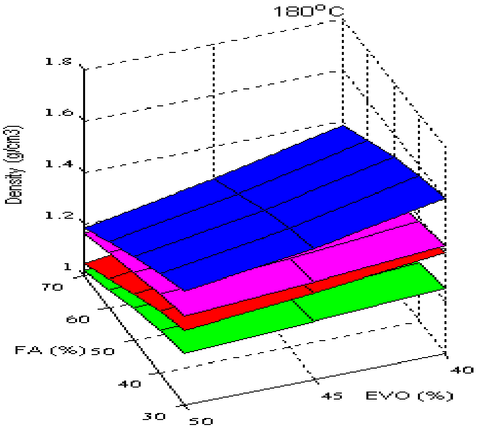

(b) 180 ^{0}C

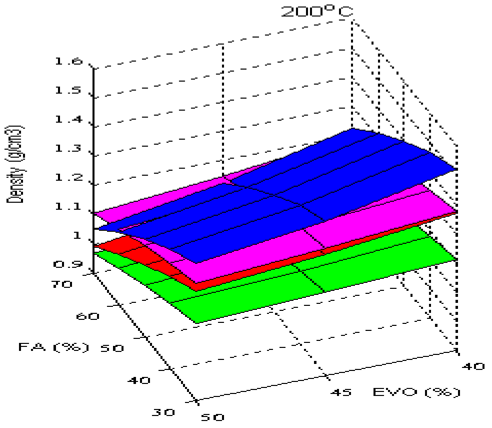

(c) 200 ^{0}C

FIG. 5 THE DENSITY, FA AND EVO PER CENT RELATION IN THE SAMPLES

Density

The density is an important parameter for construction material. The low-density products are desirable in terms of transportation, storage and handling. In order to understand the relationships among the sample density, the constituent materials and the firing temperature, we first need to consider the density of the component materials. The densities of ESO (0.985–0.995 g/cm^{3}), EZO (0.9 g/cm^{3}- 0.926 g/cm^{3}), EPO (0.897–0.941 g/cm3) and ESFO (0.925 – 0.973 g/cm^{3}) are less than those for either clay (2.24 g/cm3) or FA (1.5g/cm3). It can be certainly seen that density decreases with an increase in EVO content and, because the density of FA is less than that of C, the density decreases with an increase in the FA content. The sample density decreases as the firing temperature increases. This may be due to the loss of water and/or the loss of volatile constituents from the EVO. It is possible that there is a link between sample density and thermal conductivity, especially if that reduction in density is caused by an increase in sample porosity. The density, FA and EVO per cent relation in the samples are shown in Fig. 5. It is observed that densities of the sample are decreased with increasing FA in the mixtures due to the lower density of FA. EVOs are used as binder for sample lowered the densities too. The lowest density, 0.969 g/cm^{3}, is measured for the sample with a 70% FA/30% C ratio and 50% ESFO processed at 200^{0}C. The highest density, 1.754 g/cm^{3}, is obtained for the sample with 30% FA/70% C ratio and 40% ESO treated at 160^{0}C. Thus, the densities varied between 0.969 and 1.754 g/cm^{3}. The density is decreased with the increase in process temperature. The lowest densities for samples with ESFO are 1.078, 1.019 and 0.969 after subjected to 160, 180 and 200^{0}C, respectively. When process temperature is raised from 160 to 200^{0}C, the densities for samples with EZO, EPO, ESFO, ESO are decreased

24.69%, 30.18%, 25.91% and 40.07%, respectively.

Thermal Conductivity

The knowledge of thermal conductivity of construction materials involved in the process of heat transfer is essential in predicting the temperature profile and heat flow through the material. The thermal conductivity of construction material, one of the most commonly used construction materials, is very important. The major factors influencing material's thermal conductivity include chemical composition, pore structure and process temperature.

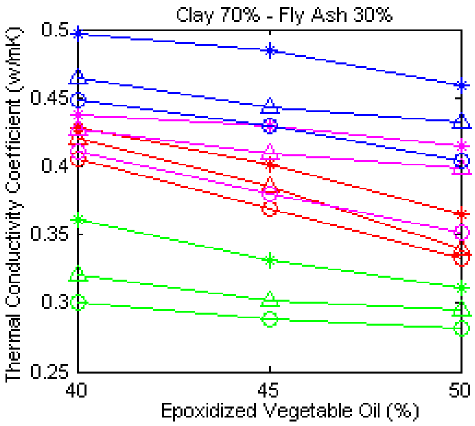

(A) C 70%-FA 30%

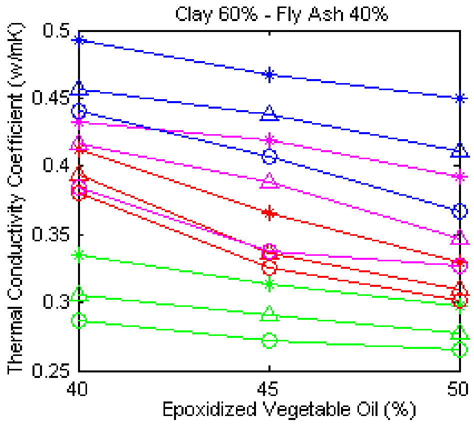

(B) C 60%-FA 40%

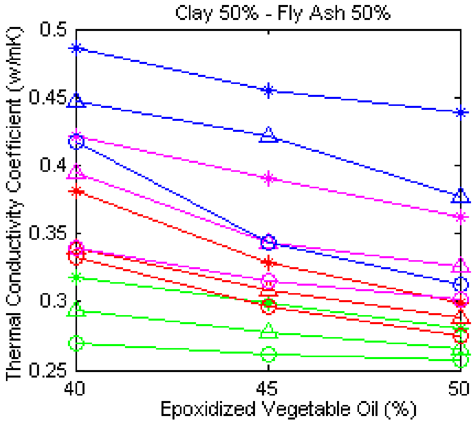

(C) C 50%- FA 50%

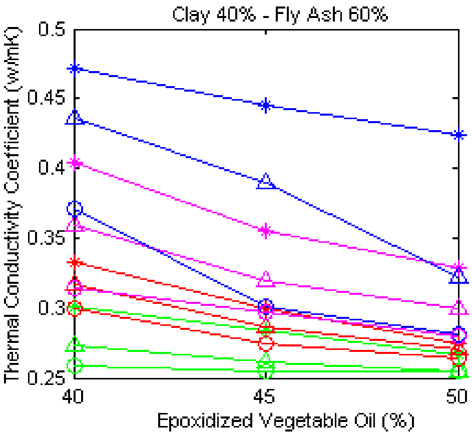

(D) C 40%-FA 60%

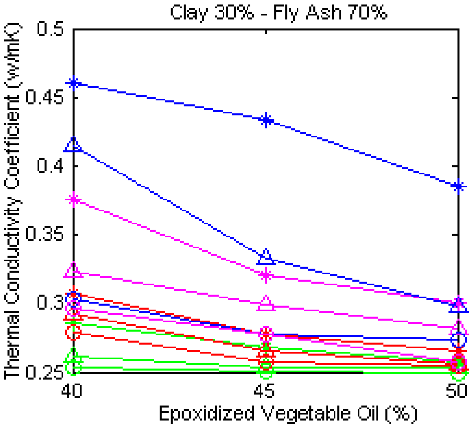

(E) C 30%-FA 70%

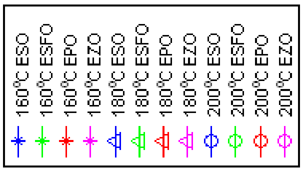

FIG. 6 RELATIONSHIP BETWEEN THERMAL CONDUCTIVITY COEFFICIENT AND EVO PER CENT

In this study, Figs. 6–8 show the effects of EVO (40%, 45% and 50%), FA (30%, 40%, 50%, 60% and 70%) and process temperature (160^{0}C, 180^{0}C and 200^{0}C) on thermal conductivity of the EPO, EZO, ESFO and ESO groups of sample, respectively. The following results have been observed.

The process temperature is an important factor affecting thermal conductivity of end product in the samples. 200^{0}C series has lower thermal conductivity than 160^{0}C series. The thermal conductivity slightly is decreased with increasing temperature as the process temperature gradually is increased from 160 to 200^{0}C, and the decrease has become more pronounced as the temperature is further increased. The decrease in thermal conductivity against sample 45 with ESFO is lower than that of sample 45 with EPO and 3.10% lower than that of sample 45 with EZO and 8.42% lower than that of sample 45 with ESO. The maximum thermal conductivities of samples with ESO processed at 160, 180 and 200°C are 0.496 (sample code: 1), 0.464 (sample code: 4) and 0.448 (sample code:7) W/mK, respectively. The highest value of thermal conductivity, 0.496 W/mK, is obtained for the sample with 30% FA/70% C ratio and 40% ESO treated at 160°C. At 180 and 200°C, the thermal conductivity values of the samples with ESO are decreased 6.45-22.59% and 9.67- 29.09%, respectively, compared to those of the samples with ESO processed at 160°C. Sample 1 with ESO processed at 160°C is given the highest thermal conductivity which was 11.96% higher than that of sample 1 with EZO and 13.70% higher than that of sample 1 with EPO and 27.21% higher than that of sample 1 with ESFO. In other words, the maximum reduction in thermal conductivity is obtained at the maximum process temperature (200°C). This is probably related to the increase of porosity due to the high process temperature. There is positive correlation between thermal conductivity coefficient and EVO-FA

The FA ranges from 30% to 70%, while the EVO ranges from 40% to 50%. The samples obtain the lowest thermal conductivity values with FA content of 70%. Increasing the FA ratio is found to impact the thermal conductivity values of samples significantly. Thus, for example, samples code: 37–38–39, 40–41–42 and 43–44–45, the lowest thermal conductivity values are obtained with the highest FA ratio and when the C ratio is low. The maximum thermal conductivity for every group EVO of samples is found for sample 1 (sample code) with FA content of 30%. For 40%, 50%, 60% and 70% FA, the reductions are 5.69-8.54-9.60-11.03%, 6.83-13.96-20.22-26.49%, 9.15-22.77-30.44-32.42% and 9.03-17.16-20.48-23.19%, respectively, compared to the corresponding sample with 30% FA and ESFO, EZO, ESO and 50% EPO processed at 200°C. The thermal conductivity of samples is decreased by 27.21-42.54% with FA content of 70% and EVO content of 40% treated at 160°C. For 30% FA, the increases are 7.25%, 14.15%, 21.05% and 28.27%, respectively, compared to the corresponding sample with 70% FA and ESO, EZO, ESFO and 40%EPO processed at 160°C. The best thermal conductivity values are obtained for samples with ESFO processed at 200°C. The thermal conductivity of these samples is 3.06 -6.25% lower than that of samples with FA content of 30 -70% processed at 180°C and 11.22 -16.89% lower than that of samples with FA content of 30-70% processed at 160°C, respectively, compared to the samples with 30-70% FA at 200°C. This is because the thermal conductivity decreased with increasing FA content. The eduction in thermal conductivity of sample by means of FA is probably related to the increase of porosity due to the addition of FA in EVO–C, the lower specific gravity of FA, and partly to the amorphous structure of FA, since the thermal conductivity of crystalline silica is about 15 times that of amorphous, it is natural for the samples with amorphous silica to have lower conductivity (Onaran).

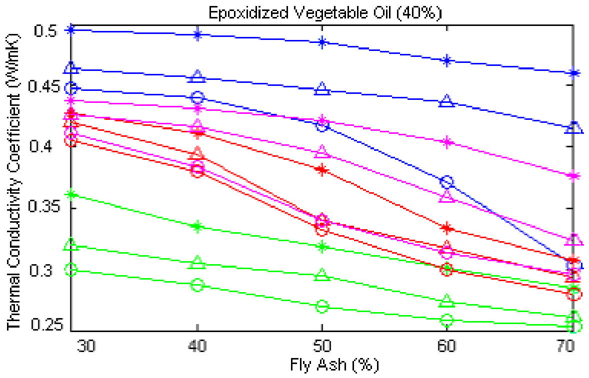

(a) EVO 40%

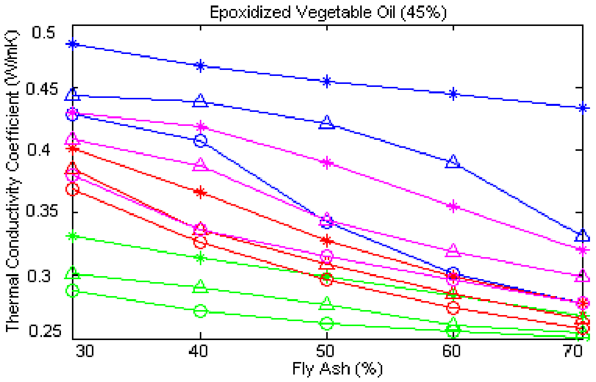

(b) EVO 45%

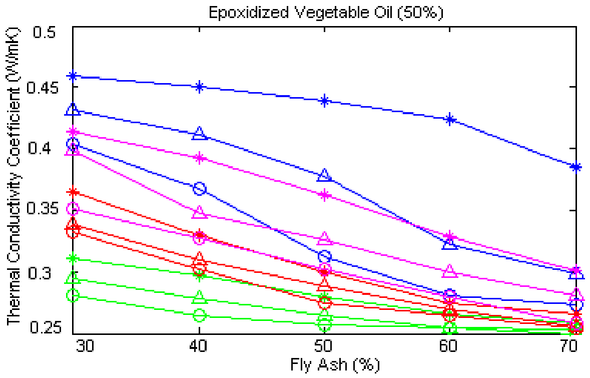

(c) EVO 50%

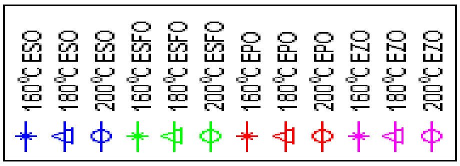

FIG. 7 RELATIONSHIP BETWEEN THERMALCONDUCTIVITY COEFFICIENT AND FA PER CENT

The best thermal conductivity values of all groups are obtained for the group ESFO, EPO, EZO and ESO, respectively. The reductions in thermal conductivity induced by 30%, 40%, 50%, 60% and 70% FA (70%, 60%, 50%, 40% and 30% C) for group ESFO (50%) are 30.44%, 27.79%, 17.62%, 9.60% and 8.4% compared to the group with 50% ESO treated at 200°C, respectively (Fig.9).

The samples reveal the highest thermal conductivity values with EVO content of 40% for all temperatures. As shown in Fig. 7, the thermal conductivity of samples is decreased by 4.00-0.79% with ESFO content of 45% and 6.30-1.18% with ESFO content of 50% at 200°C. The reductions due to FA ratio for group with 40% ESO treated at 200°C are 9.82%, 16.59%, 25.35%, 24.25% and 9.90% compared to the group with 50% ESO treated at 200°C, respectively (Fig.9). This is because the thermal conductivity decreased with increasing EVO and FA content. The low thermal conductivity of sample by means of FA is probably related to the higher air content, and partly to the amorphous structure of FA, as indicated in Refs. (Onaran and Postacıoğlu). The effect of FA and EVO (ESFO) on group ESFO is greater than that of C for all samples. The thermal conductivity of samples is decreased due to the decreasing of density.

Additionally, Gul et al., Akman and Tasdemir and Blancoetal also reported that the thermal conductivity decreased due to the density decrease of concrete. Lu-shu et al. experimentally formulated a correlation between the density and thermal conductivity, and reported that the thermal conductivity increased with increasing density.

For group EPO, FA and EVO (EPO) treated at 200°C compared to the group EPO at 160 and 180°C reducethe thermal conductivity by 14.59% and 43.37%, respectively. The reductions due to FA (30%, 40%, 50%, 60% and 70%) for group EPO (50%) are 17.82%, 17.71 %, 11.85%, 6.04% and 6.59%, compared to the group with 50% ESO treated at 200°C, respectively (Fig.9). The effect of FA at the 60% and 70% replacements on group EPO is greater than that at the other replacements. Hence, at the 30% replacement of C, both EPO and FA induce approximately equal reduction (Fig. 6-9).

Fig. 8 shows that in group EZO, FA and EVO (EZO) treated at 200°C decreasethe thermal conductivity. These reductions compared to the group EZO at 160 and 180°C are 26.49% and 37.22%, respectively. Likewise, the samples reveale the lowest thermal conductivity values with EZO content of 50%. The thermal conductivity of samples are increased about 12.83 -14.59% with EZO content of 40% and 7.19–7.63% with EZO content of 45% at 200°C. Thus, it may be concluded that decrease of thermal conductivity coefficient provided by decrease in number of EZO-FA-C grains in unit volume results in more void volume between grains and also increase in number of pores in the EZO-FA-C grains. As expected, thermal conductivity tends to increase when density increases.

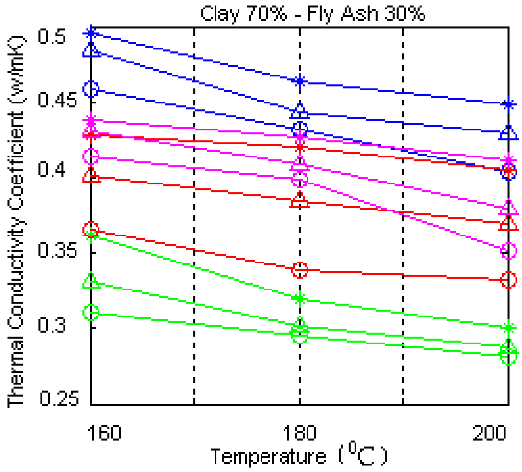

(a) C 70%-FA 30%

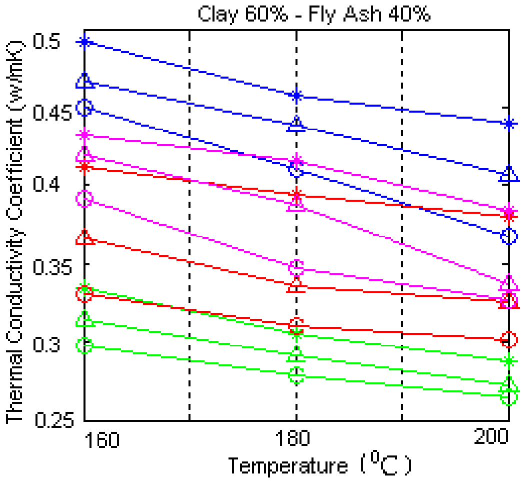

(b) C 60%-FA 40%

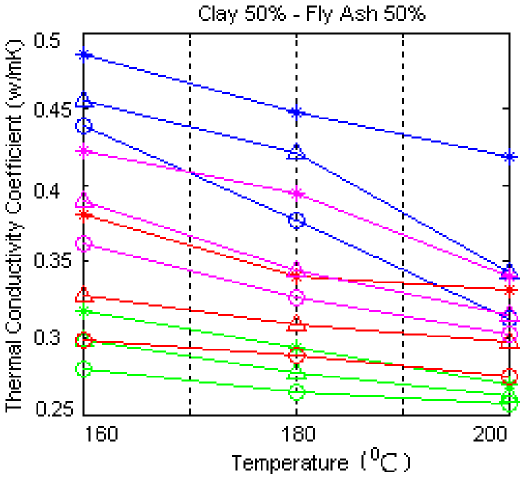

(c) C 50%- FA 50%

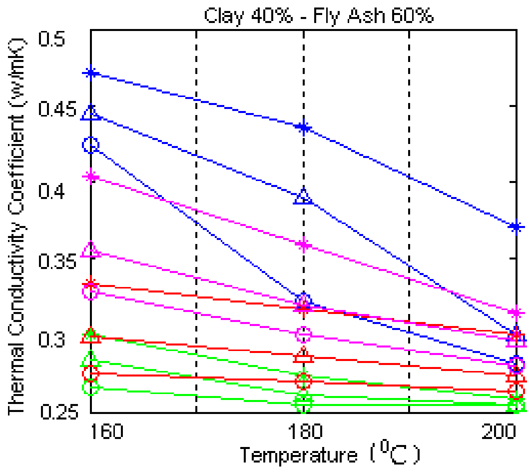

(d) C 40%-FA 60%

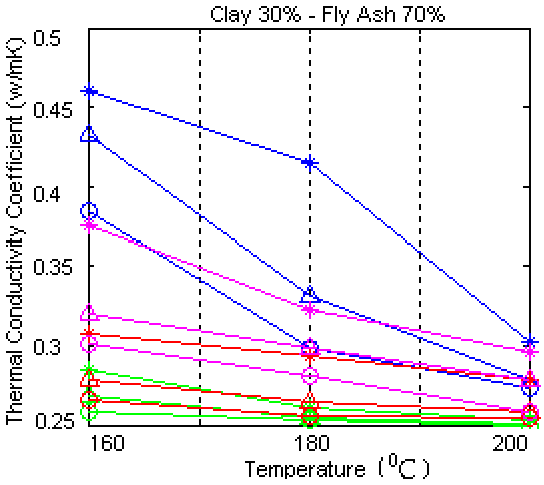

(e) C 30%-FA 70%

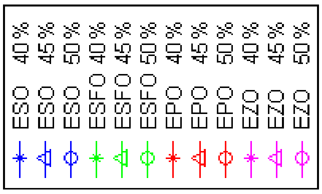

FIG. 8 RELATİONSHİP BETWEEN THERMAL CONDUCTİVİTY COEFFİCİENT AND PROCESS TEMPERATURE

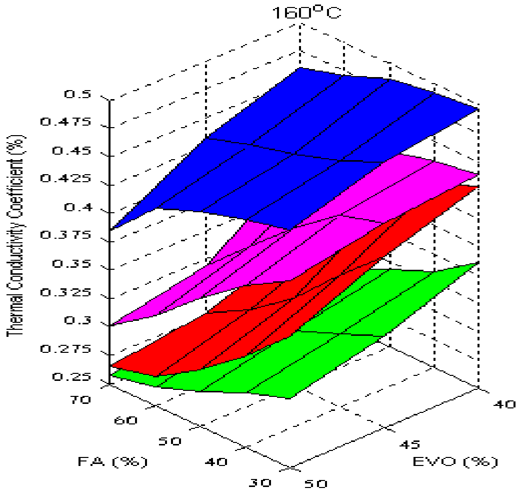

(a) 160 ⁰C

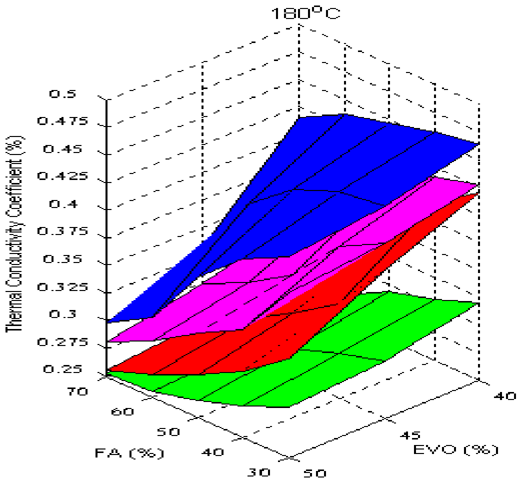

(b) 180 ⁰C

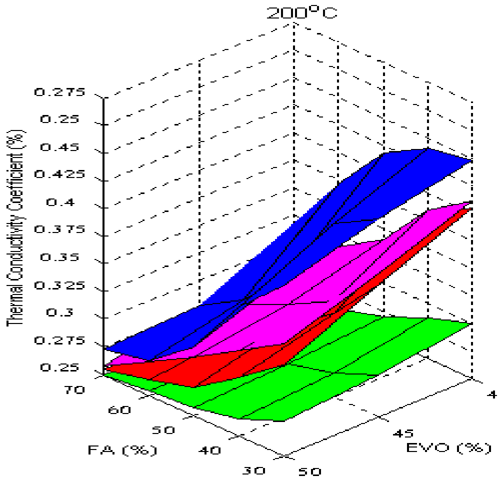

(c) 200 ⁰C

FIG. 9 RELATIONSHIP BETWEEN THERMAL CONDUCTIVITY COEFFICIENT AND EVO TYPE.

In this study, it is determined that the higher reduction in thermal conductivity in all groups is obtained for the sample with a 70% FA/30% C ratio and 50% EVO processed at 200⁰C. When the groups are compared with each other, the effects of EVO, FA and process temperature at on group ESFO are greater than those on the other groups. This is due to the fact that the effect of the EVO, FA and process temperature on sample determines the lowest thermal conductivity values for group ESFO. While the effect of the ESFO and FA at 200⁰C is 16.66%, the effect of the ESFO and FA at 160⁰C on thermal conductivity is 28.53%. The effect of the FA of 50% ESFO at 200⁰C on thermal conductivity is 5.69%, 3.01%, 1.16% and 4.00%, respectively.

Thermal conductivities of some types of plaster materials used at present (Blanco et al. and Lu-shu et al) and the most useful of the samples with EVO-FA-C are given at Table 5. It can be seen from this table that the thermal conductivity coefficients of insulation plasters made by EVO, FA and C are less than most of values stated at T.S.E. standards. The thermal conductivities of samples of groups EZO and ESO are about twice lower than those of the traditional mud bricks, whereas, those of samples of group ESFO and EPO are about three lower time traditional mud bricks (Balo ety al).

TABLE 5 THE THERMAL CONDUCTIVITY VALUES MEASURED BY SHOTHERM QTM APPARATUS IN DIFFERENT MATERIALS

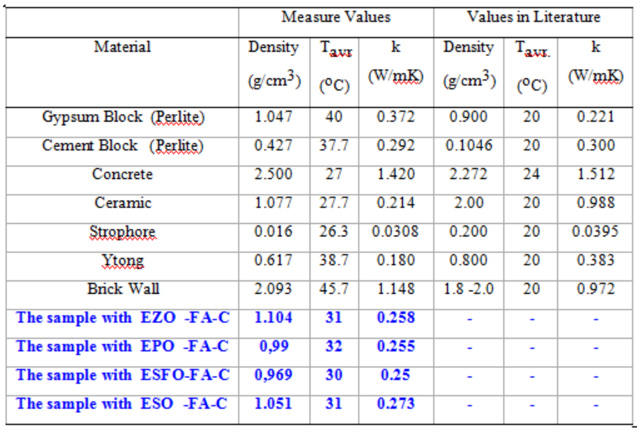

Material	Measure Values			Values in Literature		
	Density (g/cm^3)	T_{avr} (°C)	k (W/mK)	Density (g/cm^3)	$T_{avr.}$ (°C)	k (W/mK)
Gypsum Block (Perlite)	1.047	40	0.372	0.900	20	0.221
Cement Block (Perlite)	0.427	37.7	0.292	0.1046	20	0.300
Concrete	2.500	27	1.420	2.272	24	1.512
Ceramic	1.077	27.7	0.214	2.00	20	0.988
Strophore	0.016	26.3	0.0308	0.200	20	0.0395
Ytong	0.617	38.7	0.180	0.800	20	0.383
Brick Wall	2.093	45.7	1.148	1.8 -2.0	20	0.972
The sample with EZO -FA-C	**1.104**	**31**	**0.258**	-	-	-
The sample with EPO -FA-C	**0,99**	**32**	**0.255**	-	-	-
The sample with ESFO-FA-C	**0,969**	**30**	**0.25**	-	-	-
The sample with ESO -FA-C	**1.051**	**31**	**0.273**	-	-	-

In conclusion, for all groups, the thermal conductivity decreased with increasing EVO-FA content and process temperature. The variation in the reductions may be due to the testing condition and moisture contents. Both EVO (ESFO, EPO, EZO, and ESO) and FA have caused significant reductions in the thermal conductivities. The reduction due to the EVO is greater than that of the FA. The reduction in thermal conductivity is primarily due to the low density of sample with increasing EVO and FA content, and may be partly due to the amorphous silica content of FA. EVO and FA also reduce the thermal conductivity of samples up to 49.59%.

Conclusion

This study explores the possibility of use of FA by-product, natural C and renewable EVO in the sample to produce construction materials. The work presented herein has focused on the thermal conductivity properties of the construction material containing FA, C and EVO. FA (30%, 40%, 50%, 60% and 70%), C (30%, 40%, 50%, 60% and 70%) and EVO (40%, 45% and 50%) are effective for decreasing the thermal conductivity of sample up to 49.59%, which is mainly due to the relatively low conductivity of these admixtures and the consequent low density of the sample. The thermal conductivity and density of sample decreased with increasing FA and EVO content.

Densities decreased from 1.754 to 0.969 g/cm^3 with the increasing FA and EVO content of admixtures. Both EVO (50%) and FA (70%) show the maximum reduction of thermal conductivity with 30% C in all groups, and maximum reduction is observed at group ESO.

EVO is more effective than FA in decreasing the thermal conductivity. The maximum reduction is due to the FA (at 30% by weight of C) and it is 44.95%. The EVO reduces the thermal conductivity, and density of samples. The maximum reduction due to 50% EVO is 40.65%.

The results thus indicate that the samples with EVO-FA-C offer a good alternative for making environmental friendly fired construction material.

Nomenclature

K	Constant of Shoterm QTM Aparatus
H	Constant of Shoterm QTM Aparatus
t_1	Temperature of startup (K)
t_2	Temperature of finish (K)
V_1	The startup voltages of thermoelement (mV)
V_2	The finish voltages of thermoelement (mV)
k	Thermal conductivity coefficient (W/mK)
T_{avr}	Average temperature (K)
I	Current density in heater wire (A)

ACKNOWLEDGEMENTS

The authors gratefully acknowledge the financial support from the Scientific Research Projects Administration Unit of Firat University (Elazığ, Turkey) for this study (project number: 1245).

REFERENCES

Akkaya D (2002) Uçucu Kül Katkısının Dolgu Zeminlerin Stabilitesine Etkisi.

Akman MS, Taşdemir MA. Perlite concrete as a structural material, (Tasiyici malzeme olarak perlit betonu). Ankara, Turkey: 1st National Perlite Congress; 1977.

ASTM C 1113-90, Test method for thermal conductivity of refractories by hot wire, (Platinum Resistance Thermometer Technique).

Balo F, Ucar A, Yücel HL, (2010) Development of the insulation materials from coal fly ash, perlite, clay and linseed oil, Ceramics Silikaty, 54(2): 182- 191.

Balo F, Biçer Y, Yücel HL, (2010) The Engıneerıng Propertıes of Olıve Oıl-Based Materıals, Journal of the Ceramic Society of Japan, November Issue, 118 (8), 1-8.

Balo F, Yucel HL, 16-17 October (2008) Availability at engineering materials of unsaturated oils, Çukurova Üniversitesi, Adana, 563-567, (in Turkey).

Balo F, Yucel HL, December (2008) Evaluation in obtaining building materials of vegetable oils, UTES. İstanbul,. (Turkey); 213-220.

Balo F, Yucel HL, Ucar A, March (2010) Determınatıon of the thermal and mechanıcal properties for materials contaınıng palm oil, clay and fly ash, International journal of Sustainable Engineering, Vol.3, Issue 1, pp. 47 - 57.

Balo F, Yucel HL, Ucar A. March (2010). Physical and mechanical properties of materials prepared using class C fy ash and soybean oil, Journal of Porous Materials (2009) (DOI 10.1007/s 10934 -009 -9324-1) (In Press).

Balo F. (2008) Usıng Vegetable Oıls In Obtaınıng Of Composıte Materıals, PhD. Thesis. FÜ Fen Bilimleri Enstitüsü. Elazığ, (Turkey).

Blanco F, Garcia P, Mateos P, Ayala J, (2000) Characteristics and properties of lightweight concrete manufactured with cenospheres, Cement and Concrete Research 2000;30: 1715–1722.

Bussell GW (1974) Maleinized fatty acid esters of 9-oxatetracyclo-4.4.1.^{2,5}O^{1,6}O^{8,10} undecan-4-ol., US Patent, 3: 855, 163.

Chindaprasirt P, Jaturapitakkul C, Sinsiri T. (2007) Effect of fly ash fineness on microstructure of blended cement paste, Constr Build Mater., 21: 1534–1541.

Crivello JV, Narayan R. (1992) Epoxidized Triglycerides as Renewable Monomers in Photoinitiated Cationic Polymerization, Chemical Materials, 4: 692.

Cunningham A, Yapp A (1974) Liquid polyol compositions, US Patent, 3: 827, 993

Daire W.R., Downs A (1980) The hot wire test—a critical review and comparison with B 1902 panel test, Trans. Br. Ceram. Soc. 79: 44.

Demirboğa R. (2007) Thermal conductivity and compressive strength of concrete incorporation with mineral admixtures, Build Environ, 42: 2467–2471.

Denko S, Shotherm Operation Manual No: 125-2.K.K. Instrument Products Department, 13-9 Shiba Daimon. Tokyo, 105, Japan.

Eierdanz, H (1993) Industrielle fettchemie rohstoffe, verfahren, produkte, (In: Eggersdorfer, M., Warwel, S.,

Force CG, Star FS (1988) Vegetable oil adducts as emollients in skin and hair care products, US Patent, 4: 740, 367.

Gül R, Uysal H, Demirboğa R. (1997) Kocapınar Pomzası ile Üretilen Hafif Betonların ısı İletkenliklerinin Araştırılması, (Investigation of the Thermal Conductivity of Lightweight Concrete Made with Kocapınar's Pumice Aggregate), Advanced in Civil Eng.: III. Technical Congress, vol. 2, METU, Ankara, Turkey, 553–562 (In Turkish).

Güner FS, Yağcı Y, Erciyes AT (2006) Polymers from Triglyceride Oils, Prog. Polym. Sci., 31: 633-670.

Gunstone F (1996) Fatty acid & lipid chemistry, New York: Blackie Academic & Professional.

Hiroshi U, Moi K, Takoshi, T, Mitsuru N, Arimitsu U, Shiro K, (2003) Green Nanocomposites form Renewable Resources-Plant Oil-Clay Hybrid Materials, Chem. Mate., 15: 2492-2944.

Hodakowski LE, Osborn CL, Haris EB (1975) Polymerizable epoxide-modified compositions, US Patent, 4: 119, 640

Jiménez F, Palomo A, Criado AM (2006) Alkali activated fly ash binders. A comparative study between sodium and potassium activators, Mater Construct, 56: 51–65.

Khot NS, Lascala JJ, Can E, Morye SS, Williams IG, Palmese RG, Kusefoğlu SH, Wool PR (2001) Development and Application of Triglyceride Based Polymers and Composites, Joumal of Applied Polymer Science 82: 703–723.

Lu J, Hong CK, Wool RP. (2004) Biobased Nanocomposites from Functionalized Plant Oils and Layered Silicate, Journal of Polymer Science, 42: 1441-1450.

Lu-shu K, Man-qing S, Xing-Sheng S, Yun-xiu L, (1980) Research on several physico-mechanical properties of lightweight aggregate concrete, The International Journal of Lightweight Concrete 2(4):185–91.

Miyagawa H, Misra M, Drzal LT (2005) Fracture Toughness and Impact Strength of Anhydride Biobased Epoxy, Polymer Engineering and Science, 29: 487-493.

Miyagawa H, Misra M, Drzal LT, Mohanty AM (2005) Novel Biobased Nanocomposites from Function Analized Vegatable Oil and Organically-Modified Layered Silicate

Clay, Polymer, 46: 445-453.

Miyagawa H, Misra M, Drzal LT, Mohanty, AM (2005) Novel Biobased Nanocomposites from Function Analized Vegatable Oil and Organically-Modified Layered Silicate Clay, Polymer, 46: 445-453.

Miyagawa H, Mohanty AK, Burgoneo R, Drzal LT, Misra M. (2007) Novel Biobased Resins from the Blends of Functionalized Soybean Oil and Unsaturated Polyester Resin, Journal of Polymer Science Part B: Polymer Physics, Natural Oils-A Review, Prog. Polym. Sci 31: 983–1008.

Onaran K (1993) Malzeme Bilimi (Materials Science), Science Technical Press, Istanbul, Turkey, 174 (In Turkish).

Park SJ, Jin FL, Lee JR (2004) Synthesis and Characterization of Novel Conjugated Polymer with 4H-Cyclopentadef phenanthrene and the Sulfanyl Group, Macromol. Rapid. Commun. 25: 724.

Park SJ, Jin FL, Lee JR (2004);Synthesis and Thermal Properties of Epoxidized Vegetable Oil, Korea Research Institute of Chemical Technology, 41: 724-727.

Pei-wei G, Xiao-lin L, Hui L, Xiaoyan L, Jie H (2007) Effects of the fly ash on the properties of environmentally friendly dam concrete, Fuel, 86: 1208–1211.

Postacıoğlu B (1986) Bağlayıcı Maddeler, (Cementing Materials), vol. 1, Matbaa Teknisyenleri Basımevi, Istanbul, Turkey, 63– 66 (In Turkish).

Salunkhe DK, Chavan JK, Adsule RN, Kadam SS (1992) World oilseeds: chemistry, technology and utilization, New York: Van Nostrand Reinhold.

Sharma V, Kundu PP (2006) Addition Polymers from Natural Oils-A Review, Prog. Polym. Sci 31: 983–1008.

Topçu IB, Canbaz M. (2007) Effect of different fibers on the mechanical properties of concrete containing fly ash, Constr Build Mater, 21: 1486–1491.

Trecker DJ, Borden GW, Smith OW (1976) Method for curing acrylated epoxidized soybean oil amine compositions, US Patent, 3: 979, 270.

Trecker DJ, Borden GW, Smith OW (1976) Acrylated epoxidized soybean oil amine compositions and method, US Patent, 3: 931, 075.

Willshee JC (1980) Comparison of thermal conductivity methods, Proc. Br.Ceram. Soc., 29: 153.

Wulff, G., (Eds.), Nachwachsende RohstoffePerspektiven für die Chemie.) VCH, Weinheim, 23–32.

Zhu J, Chandrashekhara K, Flanigan V, Kapila S, Zhu J. Manufacturing and Mechanical Properties of Soy Based Composites Using Pultrusion, Composites Part A: Applied Science and Manufacturing , January 2004; 35(1): 95-101.

Nanocantilever Property Based on Carbon Nanotubes

Khalil El-Hami

Univ Hassan 1, Faculty of Khouribga, Laboratory of Nanosciences and Modeling
BP.145, Khouribga, Morocco

elhami_k@yahoo.com

Abstract

The mechanical and geometrical properties of carbon nanotubes (CNT), nanocantilevers beam from single walled carbon nanotube (SWCNT) material were investigated in this study. Therefore, a bundle of SWCNT in cylindrical geometry with 20 nm in diameter and 1 μm in length was fabricated in two nanocantilever devices: clamped-clamped and clamped-free positions and the foucus of this paper was on the latter design. In this case, the results showed that the first resonance frequency ω_0 of the nanocantilever beam from the measured SWCNTs' dimension and spring constant is about 100 MHz. Due to the exceptional mechanical and geometrical characteristic of SWCNT, the first resonance frequency found is high compared to that one made from mica (ω_0 = 20 Hz) or silicon (ω_0 = 14 KHz). The result obtained is expected to have potential applications in nanoelectromechanical system (NEMS) working with high resonance frequencies.

Keywords

Single Walled Carbon Nanotubes; Nanocantilever Vibration; Clamped-Clamped; Clamped-Free

Introduction

Carbon nanotubes with special electronic and mechanical characteristics have attracted much attention from many researchers in various fields. In fact carbon nanotubes are tiny tubes made of carbon atoms arranged in hexagonal patterns whose nanometer diameter and length are larger and about micrometers. The single walled carbon nanotubes (SWCNT) can be regarded as a rolled up piece of a graphene sheet, two-dimensional graphite plane, in a cylinder formed by wrapping up a regular hexagonal lattice. Such nanomaterials are promising materials in the area of nanoscience towards nanotechnology. Specially, the carbon nanotubes have found many applications in atomic force microscopy cantilever tip and actuators. This study is concerning the use of SWCNT as a nanocantilever beam with remarkable properties. The advantages result in high flexibility and stiffness of SWCNT beside its nanometer-scale geometry. In mechanic, resonnace leads system to oscillate with greater amplitude at some specific frequencies. High resonance frequency is needed and even small periodic driving forces can produce large amplitude oscillations. Moreover, at high resonance frequency, the system can store mechanical energy.

Experimental Set-up

SWCNTs, generated by the electric arc discharge method, were dispersed in ethanol solvent with an ultrasonic bath and sonicated further to promote uniform dispersion. A drop of SWCNTs solution was deposited on the electrodes patterned by photolithography as shown in Fig.1 that is an image obtained from the scanning electron microscopy SEM. After few minutes, the ethanol was evaporated and the SWCNTs were extended and stuck on the electrodes used as support. The SWCNT nanocantilever was designed in two devices: clamped-clamped and clamped-free positions.

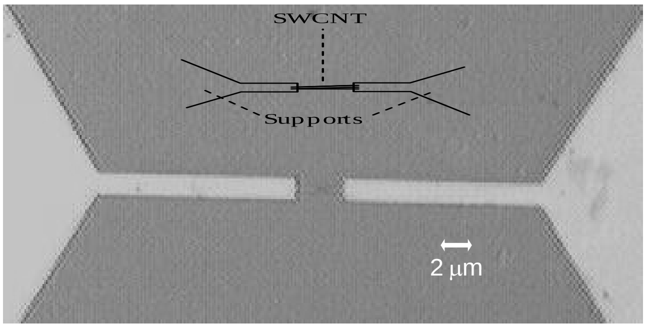

FIG.1 SCANNING ELECTRON MICROSCOPY OF SWCNT BUNDLE BETWEEN TWO ELECTRODES PATTERN AS NANOCANTILEVER CLAMPED-CLAMPED DESIGN

In the same figure, the concept is schematically illustrated and drawn.

The clamped-free design, the focus of this paper, is mean clamped at one end and free to move in the other end; in addition, the transverse motion of cantilevers is studied as well.

Fig.2 shows a high resolution electron microscopy (HREM) image of SWCNT bundle as nanocantilever clamped-free design

FIG.2 HIGH RESOLUTION ELECTRON MICROSCOPY IMAGE OF SWCNT BUNDLE AS NANOCANTILEVER CLAMPED-FREE DESIGN

Analytical Calculation of Flexural Vibration of Clamped-free Cylindrical Nanocantilever

The theory of vibration modes of flexural cantilever is well known. The equation of motion of the cantilever is a differential equation of fourth order and can be briefly summarized as equation 1:

$$EI\,(\partial^4 Z/\partial x^4) + \rho S\,(\partial^2 Z/\partial t^2) = 0 \qquad (1)$$

where E is the modulus elasticity, I is the area moment of inertia, ρ is the mass density and S is the cross section; x is the coordinate in the longitudinal direction of the cantilever and $Z(x)$ is the deflection from the rest position of the length element at x.

The mode shapes for a continuous cantilever beam are given as:

$$Z_n(x) = z_0[(\cos k_n x - \cosh k_n x)-(\cos k_n L+\cosh k_n L)\,(\sin k_n x\, \sinh k_n x)/(\sin k_n L+\sinh k_n L)]$$

where z0 is the vibrational amplitude and n is the mode number.

The resonance frequency for n, the mode number is given as: wn = k2n {(EI/ρS}1/2, for $k_0 = 1.875$, $S = \pi(d/2)^2$ where d is the SWCNT diameter about 1.2 nm, and the first resonance frequency of the nanocantilever beam calculated from the measured SWCNTs'dimension and spring constant is about 100 MHz.

In previous study, a cantilever beam from mica muscovite with a modulus elasticity of $1.7\ 10^{11}$ Pa, a mass density of 2.7 and the geometrical properties of 25 mm in length, 6 mm in width and 20 μm in thickness, the first resonance frequency ω_0 20 Hz have been investigated. Moreover, in the study of U. Rabe et al. used the silicon material and they found a resonance frequency ω_0 of about 14 kHz. By comparison, the resonance frequency of SWCNT is so high and the ration in case of mica muscovite or silicon is respectively about $5\ 10^6$ and 7142 times. The comparative resonance frequencies dependent of physical properties of materials have been summarized in the following table.

Type of material	First resonance frequency
SWCNT	100 MHz
Si	14 kHz
Mica (muscovite)	20 Hz

The high value of the first resonance frequency of SWCNTs could be explained by their exceptional mechanical and geometrical characteristic. It is noted that high resonnace frequency leads system to oscillate with greater amplitude at some specific frequencies and the system can stores the mechanical energy.

Conclusion

The technique to fabricate nanocantilever using SWCNT has been described in the experimental part. The analytical method for calculation of the resonance frequencies is determined. The result have suggested that, due to the high resonance frequencies, the SWCNTs nanocantilever can possibly be used in nanoelectromechanical system (NEMS) working with high resonance frequencies.

The perspective of the nanocantilever for further investigation is to calculate the vertical shear force, which counteracts the object's weight and its influence on resonance frequency change.

REFERENCES

Jorio A, Saito R, Hafner J.H, Lieber C.M, Hunter M, McClure T, Dresselhaus G andDresselhaus M. S. "Fullerenes and Carbon Nanotubes" Phys. Rev. Lett. 86 (2001): 1118-1125.

Xiaotong Gao, Wei-Heng Shih and Wan Y. Shih "Vibration Energy Harvesting Using Piezoelectric Unimorph Cantilevers with Unequal Piezoelectric and Nonpiezoelectric Lengths". Applied Physics Letters, 97, (2010): 233-240.

Beeby S.P. "A micro electromagnetic generator for vibration energy harvesting" Journal of Micromechanics and Microengineering, 17-7 (2007): 1257-1265.

Takeshi Fukuma, Yasutaka Okazaki, Noriyuki Kodera, Takayuki Uchihashi and Toshio Ando "High resonance frequency force microscope scanner using inertia balance support"Applied Physics Letters, 92, (2008): 243-249.

Marc Dequesnes, S V Rotkin and N R Aluru. "Calculation of pull-in voltages for carbon-nanotube-based nanoelectromechanical switches". 2002 Nanotechnology, 13, (2002) : 120-128.

Baughman Ray H, Zakhidov Anvar A and Heer Walt "Carbon nanotubes--the route toward applications"

Science, 297, (2002): 787-792.

Baughman, Ray H, Cui, Changxing, Zakhidov, Anvar A, Iqbal, Zafar, Barisci, Joseph N, Spinks, Geoff M, Wallace, Gordon G, Mazzoldi, Alberto, De Rossi, danilo, Rinzler, Andrew G, Jaschinski, Oliver; Roth, Siegmar, Kertesz, Miklos "Carbon nanotube actuators" Science, 284, (1999): 1340-1344.

Wang, Zong-lin lin "Nanobelts as nanocantilevers Applied Physics Letters, 82, (2003): 2886–2888.

El-Hami K, Gauthier-Manuel B. "Selective excitation of the vibration modes of a cantilever spring" Sensors and Actuators, A 64, (1998): 151-155.

Rabe U, Janser K and Arnold W "Mapping mechanical properties of organic thin films by force-modulation microscopy in aqueous media" Rev.Sci. Instrum. 67, (1996): 9-14.

Sader J. E, Larson I, Mulvaney P and White L. R. "Method for the calibration of the atomic force microscopy cantilevers " Rev Sci. Instrum. 66 (1995): 3789-3797.

M. Sasaki, K. Hane, S. Okuma and Y. Bessho "Rheology of Passive and Adhesion-Activated Neutrophils Probed by Atomic Force Microscopy" Rev Sci. Instrum. 65 (1994) 1930-1939.

Neumeister J. M and Ducker W. A "Calibration of rectangular atomic force microscope cantilevers " Rev Sci. Instrum. 65 (1994) 2527-2533.

Humar, Prentice-Hall J. L, Dynamics of Structures, (1990) ISBN 0-13-222068-7.

Atkins P. W, Physical Chemistry. 5th ed. New York: W. H. Freeman and Company, (1994).

Gere J. M, Timoshenko S. P, Mechanics of Materials. 4th ed. Boston: PWS Publishing Company, (1997).

Voltera E, Zachmanoglou E. C, Dynamics of Vibrations. Columbus, Charles E. Merrill Books, Inc., (1965).

El-Hami K and Matsushige K "Alignment of Different Lengths of Carbon Nanotubes Using Low Electric Field" IEICE Transactions on Electronics, 87, (2004) : 2116-2122.

El-Hami K and Matsushige K "Electrostriction in single walled carbon nanotubes" Journal of Ultramicroscopy, Vol. 105, Fasc No.242, (2005) : 2344-2349

El-Hami K and Matsushige K "Imaging Wet Individual Single Walled Carbon Nanotube at Atomic Level" Construction and Building Technology Journal, (2008): 134-136.

Khalil El-Hami was born in Khouribga (Morocco) in 1965 and earned his Ph.D in 1996 in material sciences and engineering from Université des Sciences et Techniques de Franche-comté in Besançon (France). After being a Senior Research Scientist for CNRS (Centre National de la Recherche Scieitifique) in Besançon, France, during 1996-1998, he joined Max-Plank Institute in Stuttgart, Germany for synthesis and production of carbon nanotubes. From 1998 to 2005, he moved to Kyoto University in Japan as associate Professor and was promoted to full Professor position in in the Department of Electronic Science and Engineering. His major fields of study is related to nanomaterials, nanocomposites for nanosciences towards nanotechnology.

Since 2006, he has been Professor and Director of Laboratory of Nanosciences and Modeling at the University of Hassan 1, Faculty of Khouribga, Morocco.

Prof. Dr. El-Hami is member of several boards and committees, including Associate Editor of international scientific journals. He earned the first price of idea contest of Kyoto University in 1999 (Japan). He has 2 Japaneses patents protected in TLO (Technology Licensing Organisation, Japanese Patent organization), over 80 refereed international publications and communications with over 1400 citations.